



An Investigation of the Young Stellar Population in the Cep A Region

by
Magnus Gålfalk



Master thesis in Astronomy

Department of Astronomy, Stockholm University
1998 / 1999

Table of contents

1. Introduction and concepts	1
1.1 YSOs and their classification	1
1.2 Luminosity-Mass functions	3
1.3 The Initial Mass Function (IMF).....	4
1.4 The Cepheus A molecular cloud	5
1.5 The Cepheus A region.....	6
1.6 About this master thesis	6
2. An introduction to ISOCAM.....	8
2.1 The ISO-satellite	8
2.2 An overview of ISOCAM	9
2.3 Available filters and arrays	11
2.4 Readout sensibility	13
2.5 Effects of charged particles	14
2.6 Transient and memory effects	14
2.7 Flatfielding.....	15
3. Processing of the ISOCAM data	17
3.1 The data calibration procedure	18
3.2 The ISOCAM data formats	19
3.3 Dark correction.....	19
3.4 Glitch correction.....	20
3.5 Second order dark correction	21
3.6 Transient correction	22
3.7 Masking.....	23
3.8 Flatfielding	24
3.9 Point source detection	24
3.10 Photometry of point sources.....	26
3.11 Correlation between LW2 and LW3 point sources	27
4. Results of the ISOCAM observations	28
4.1 Mosaics of the Cepheus A region.....	28
4.2 Calibration of source positions.....	28
4.3 Detected sources.....	29
4.4 Colour diagrams	31
5. My observations at visual and near-IR wavelengths.....	34
5.1 Planning the observations.....	34
5.2 Filter testing	36
5.3 Preparations.....	37
5.4 The CCD camera.....	38
5.5 Telescope testing	38
5.6 Observations.....	39
5.7 Data reduction	42
5.8 The mosaics of Cepheus A in Visual and Near-IR observations.....	42
5.9 Identification of ISOCAM sources.....	43
5.10 Photometry	44
5.10.1 The photometry program.....	44
5.10.2 Calculating the integrated PSF.....	47
5.10.3 Uncertainty estimations.....	48
5.11 Results.....	49

Continued overleaf..

6. Additional Near-IR observations	53
6.1 The 2MASS survey.....	53
6.1.1 Identification of ISOCAM sources	53
6.1.2 Results	55
6.2 The central Cep A region.....	59
7 Summary of results.....	61
References.....	65
Appendix A – ISOCAM data reduction (one raster).....	66
Appendix B – Aperature photometry program.....	68
Appendix C – Vocabulary	71
Appendix D – The optical mosaic (V filter).....	73
Appendix E – ISOCAM mid-IR mosaics	74

1. Introduction and concepts

Since regions of star formation and consequently newborn stars are located deep inside gas and dust clouds, infrared astronomy is a powerful tool in the search for embedded young stars, lying at great optical depths for visual light.

In this master thesis, a region centred on the compact molecular cloud Cepheus A, will be examined at visual, near-IR and mid-IR wavelengths. The purpose of the observations is to detect and classify Young Stellar Objects (YSOs) present in this active star formation region. The focus of this project is the recently collected mid-IR data taken by ISOCAM onboard the ISO-satellite, using additional observations in visual and near-IR to aid in the classification of the ISO-sources found.

I have made observations in both the visual and near-IR spectral regions using the 1m-reflector telescope at Stockholm Observatory. Also, part of the region has been observed in the J, H and K_s near-IR passbands as part of the ongoing 2 Micron All Sky Survey (2MASS).

This chapter introduces important concepts such as YSOs, Luminosity-Mass functions, Initial Mass Function (IMF), InterStellar Medium (ISM) and also gives details on the region observed.

1.1 YSOs and their classification

In order to detect and classify YSOs there are a number of methods available, one of the most efficient and the one relevant to the ISO-observations is detecting sources with IR-excess and this method will be used in this master thesis. This continuum IR-excess is thought to arise in a circumstellar disk that surrounds a young star.

The two used mid-IR filters in the present ISOCAM observations are called LW2 (6.7 μm) and LW3 (14.3 μm).

For the ISO-observations two related indices are used to classify detected sources, the spectral (SED) index $\alpha_{6.7-14.3}$ (from now on shortened as α , always referring to the spectral index between 6.7 μm and 14.3 μm) and the colour index $[14.3/6.7] = \log(F_{14.3}/F_{6.7})$. Except for sources with small IR excess, where the interstellar reddening may make up a large part of the excess, it is often possible to classify a source as having intrinsic excess using one of these indices.

The spectral index is defined as

$$\alpha = \frac{d\log(\lambda \cdot F_\lambda)}{d\log(\lambda)} = -\frac{d\log(\nu \cdot F_\nu)}{d\log(\nu)}$$

where the notations have their usual meaning.

For the ISO-observations, this can be written as:

$$\alpha = -\frac{\log\left(\frac{c}{\lambda_{14.3}} F_{14.3}\right) - \log\left(\frac{c}{\lambda_{6.7}} F_{6.7}\right)}{\log\left(\frac{c}{\lambda_{14.3}}\right) - \log\left(\frac{c}{\lambda_{6.7}}\right)} = -\frac{\log\left(\frac{\lambda_{6.7}}{\lambda_{14.3}}\right) + \log\left(\frac{F_{14.3}}{F_{6.7}}\right)}{\log\left(\frac{\lambda_{6.7}}{\lambda_{14.3}}\right)} = \frac{\log\left(\frac{F_{14.3}}{F_{6.7}}\right)}{\log\left(\frac{14.3}{6.7}\right)} - 1$$

That is, the ISOCAM single colour index [14.3/6.7] and the spectral index α are related as:

$$[14.3/6.7] = \log\left(\frac{F_{14.3}}{F_{6.7}}\right) = (\alpha + 1) \cdot \log\left(\frac{14.3}{6.7}\right)$$

All ISO-sources are classified as either 'blue' or 'red', referring to the amount of mid-IR excess (at 14.3 μm). Sources classified as 'blue' lacks sufficient mid-IR excess according to the single colour index condition $[14.3/6.7] \lesssim -0.20$ and are often background or foreground stars of the observed star-formation cloud. Sources with $[14.3/6.7] \gtrsim -0.20$ are listed as having mid-IR excess and are therefore YSO-candidates.

Newborn stars (YSOs) can be observationally classified into four evolutionary classes (0, I, II and III) with a gradual loss of circumstellar matter, according to current theories of low mass star formation (Adams et al. 1987, Lada. 1987, Shu et al. 1987, André et al. 1993). The following table contains information about the spectral and single colour indices in relation to the evolutionary classes of young stars.

Table 1-1. *Observational classification limits used to classify YSO candidates found with ISOCAM.*

Source type	Spectral index	Single colour index	Designation
Class 0	---	---	Not detected in mid-IR
Class I	$\alpha \geq 0$	$[14.3/6.7] \gtrsim 0.33$	'Super-red' source
Class II	$-1.6 < \alpha < 0$	$-0.20 \lesssim [14.3/6.7] \lesssim 0.33$	'Red' source
Class II/III limit	$\alpha = -1.6$	$[14.3/6.7] \approx -0.20$	'Red/Blue' limit
Normal photosphere	$\alpha \approx -3.0$	$[14.3/6.7] \approx -0.66$	

Class 0 objects are YSOs in their main accretion phase, having cold blackbody SEDs that peak in the far-IR and are therefore generally not observable in the mid-IR (ISOCAM), however due to the short time scale of this phase ($< 10^4$ years), they are expected to be few. They are deeply embedded in a substantial amount of circumstellar matter.

Class I objects have evolved to a later accretion phase (that lasts $\sim 10^5$ years) and can successfully be modelled as consisting of three parts: Stellar core, circumstellar disk and a spherical envelope/halo. They are easily detected by ISOCAM due to their large mid-IR excess ('super-red'), having broad SEDs with a rising SED-index towards longer wavelengths ($\alpha \geq 0$) in the mid-IR.

Class II consists of objects that have expelled their infalling envelopes with the help of their strong winds and most of the circumstellar matter has evolved into an optically thick disk (these objects are known as Classical T Tauri Stars, CTTS). They are recognized by their

broad SEDs with $-1.6 < \alpha < 0$. ISOCAM can also detect these objects easily, classifying them as 'red' due to their mid-IR excess. This phase lasts $\sim 10^6$ years, after that the disk becomes optically thin and the YSOs evolve into the next phase (class III).

Class III is the final phase of the YSOs evolution (lasting $\sim 10^7$ years) and is often associated with Weak emission T Tauri Stars (WTTS) that have either lost their disks or do not interact with one. YSOs in this class are often not distinguishable from evolved ('normal') stars (using ISOCAM) since their mid-IR imprints of a disk eventually disappear, resulting in a naked young star. However, some objects of this class have previously been found with enough mid-IR excess to be classified as class III objects using ISOCAM observations.

These classes are just an approximation of a continuous evolution, therefore their durations are just rough estimates.

Searching for Mid-IR excess is thus a very efficient method of finding YSOs. However, if near-IR observations are available (for instance in the J, H and K_s passbands) the situation gets clearer when these are combined with the mid-IR observations. Then it is possible to separate intrinsic and interstellar mid-IR reddening, dividing the observed population into background stars (interstellar reddening) and YSO candidates (intrinsic reddening).

Near-IR excess is also a possible method of finding YSO-candidates, but near-IR excess is by far not as reliable as mid-IR excess in detecting YSO-candidates, because some YSOs lack detectable near-IR excess due to a 'hole' or an optically thin region created near the young star.

1.2 Luminosity-Mass functions

Current theoretical studies of star formation and pre main sequence tracks yields a relation between the luminosity of an observed young star and its mass, this is a 'one-to-one' relation with only one possible mass for each luminosity (monotonous relation).

There are however several functions, depending on the age of the YSOs.

The Luminosity-Mass functions for 0.5, 1.0 and 2.0 Myr old stars are plotted in figure 1-1. These are adopted from the latest model calculations by D'Antona & Mazzitelli (1997). A single age of 1.0 Myr will be used for all YSOs in the Cepheus A region.

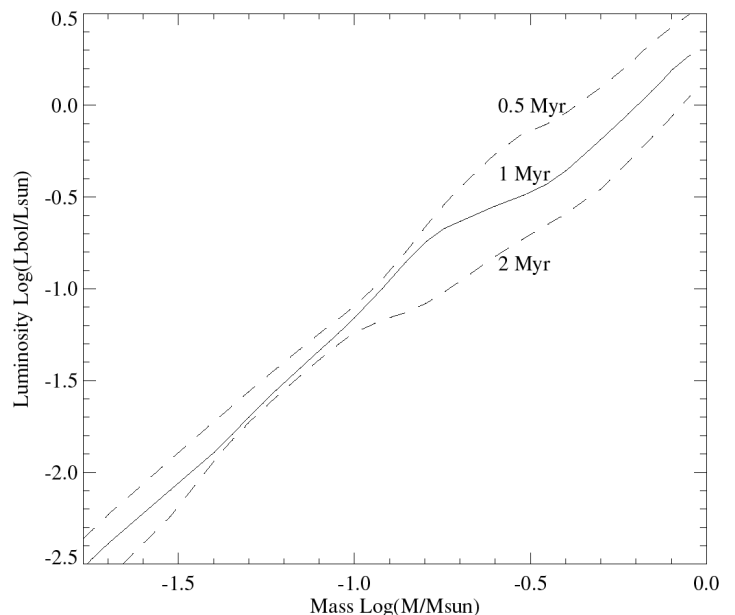


Figure 1-1. Luminosity-Mass functions for young stars.

The ages of $0.5\text{-}2.0 \cdot 10^6$ years were chosen in figure 1-1 since most YSOs found with ISOCAM are of Class II (beginning at an age of a few 10^5 years and entering Class III after a few 10^6 years).

There is a problem in finding a single age to use for all the young stars in a given star formation region. Although there is no support for assuming co-eval star formation for a whole molecular cloud, it can be statistically justified to assume a single age when no spectral information is available.

1.3 The Initial Mass Function (IMF)

The collections of young stars with ages of 10^7 years or less found in association with molecular clouds are referred to as the initial stellar population. On these short time-scales the stars cannot have moved far from their birthplaces, therefore studying the mass distribution of these young stars results in the Initial Mass Function (IMF) of the observed molecular cloud.

Regions of low to intermediate mass star formation offers a good link between cloud morphology and the final mass spectrum since these regions are less destructive to their local environment than clusters of high mass stars. The cloud clump MF and the stellar IMF seem to be different, this mystery may eventually be solved by observations of these types of star formation regions.

There are many unanswered questions about the IMF that needs to be investigated, for instance it is not yet known if the IMF varies between different types of molecular clouds or in regions where star formation appears to be spontaneous rather than externally triggered. Another interesting issue is if there is a mass-cutoff on the low-mass end of the IMF or if there are many brown dwarfs forming in clouds.

In figure 1-2, the IMF as modelled by Scalo (1998) has been calculated for masses in the range $0.1\text{-}10 M_{\text{Sun}}$ using two power law functions, defined by the local logarithmic derivate Γ as:

$$\Gamma \equiv d \log F(\log m) / d \log m$$

where F denotes the IMF. The dashed curves in the plot represents the uncertainties in the IMF. The following logarithmic derivatives were used:

$$\Gamma = \begin{array}{ll} -0.2 \pm 0.3 & \text{for } 0.1 \text{ to } 1 M_{\text{Sun}} \\ -1.7 \pm 0.5 & 1 \text{ to } 10 M_{\text{Sun}} \end{array}$$

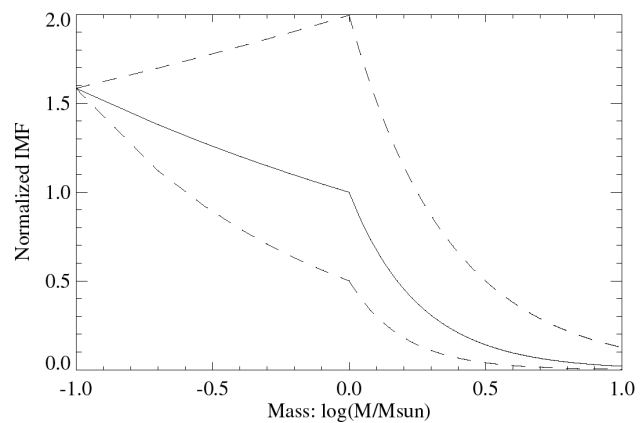


Figure 1-2. The IMF as modelled by Scalo (1998) Dashed curves represents the uncertainties (min and max IMFs) of the two power laws used in the model.

In reality, Γ is often not constant and observational data may suggest double or multiple power laws or even ledges, dips and peaks! However, for simplicity it is usually simplified as being constant within each selected mass region. This model by Scalo is the 'best' but certainly not definitive IMF as of yet.

In the last decade, there has been an increasing interest in finding observational evidence of brown dwarfs ($<0.08 M_{\text{Sun}}$) or even free floating giant planets! It seems reasonable for such objects to exist since the minimum mass (Jeans mass) required to collapse a cloud is less than $\sim 0.01 M_{\text{Sun}}$. There is still much unknown about the IMF and even though the IMF inevitably must decrease for masses approaching zero, several new observations shows no signs of a decrease. This suggests that giant planets and low-mass star formation may be more frequent than previously thought.

1.4 The Cepheus A molecular cloud

Gas and dust that exists between stars is known as the interstellar medium (ISM), it generally consists $\sim 70\%$ of hydrogen (H I, H II and H₂) while helium makes up most of the remaining mass. Heavier atoms, such as carbon and silicon usually account for only a few percent of the ISM. There are many more chemical species that contribute to the ISM, however in less abundances. In the following, the species relevant to the Cepheus A region and especially to the ISOCAM observations will be discussed.

In the Cep A GMC core, several species has been found, for instance: CO, CS, CN, C₂H, HCO⁺, N₂H⁺, CH₃C₂H, HC₃N, SO, CH₃OH, HCN, HNC and C₃H₂ (Bergin et al. 1997). The two filters used with ISOCAM, LW2 (5-8.5 μm) and LW3 (12-18 μm) were especially designed to avoid the silicate absorption bands (at 9.7 and 18 μm) and are centered on two minima of the interstellar extinction curve, however, they include the unidentified IR emission bands (UIBs) that are probably caused by so called PAHs.

PAHs (Polycyclic Aromatic Hydrocarbons) are planar molecules with organic benzene ringlike structures. Vibrations in the C-C and C-H bonds of these molecules results in the emission UIBs located in the wavelength range 3.3-12 μm which shows up in the LW2 (6.7 μm) images as bright nebulosity. Actually, the benzene rings are clustered in groups of about 20-100, too large to be giant molecules but yet too small to be dust grains, they are simply called PAHs.

Apart from emission-bands, there are of course also interstellar absorption-bands and these cause extinction that is more efficient when scattering light at shorter wavelengths. At optical and near-IR wavelengths the extinction smoothly decreases with increasing wavelength and this gives rise to the effect called 'Interstellar reddening' that makes background sources appear redder than they actually are. This may be a problem when comparing a source's magnitude at different wavelengths. It is however possible to separate intrinsic (real) reddening of a source from interstellar reddening in for instance a 'colour/colour' diagram as will be done in this master thesis¹.

¹ See chapters 5.11 (my observations) and 6.1.2 (2MASS observations) for colour/colour diagrams.

1.5 The Cepheus A region

Sargent (1977) discovered several CO hot spots while surveying the giant (20x60 pc) Cepheus OB3 molecular cloud, one of these was designated Cep A. She interpreted Cep A as the currently active spot in a region of sequential star formation. Cep A seems to be the birthplace of a new subgroup of the Cepheus OB3-association.

The distance to Cep A (adjacent to the Cep OB3 association) has been determined to 730 pc (Blaauw, Hiltner and Johnson. 1959).

The Cep A region shows several signs of star formation:

- A bipolar outflow* (Rodriguez et al. 1980, Brown et al. 1981, Ho et al. 1982)
- Compact HII regions* (Beichman et al. 1979, Simon & Joyce 1983, Hughes & Wouterloot 1984, Torrelles et al. 1985)
- H₂O and OH masers* (Wouterloot et al. 1980, Rodriguez et al. 1980b, Lada. 1981)
- One Herbig-Haro object* (Gyulbudaghian, Glushkov and Denisyuk 1978).

In figure 6-5, a K' image (2.17 μm) of the central Cep A region is shown. The bipolar outflow ('red' and 'blue' lobes), the Herbig-Haro object GGD 37 (shock excited) and some of the infrared sources Cep A IRS1-IRS8 (Lenzen, Hodapp and Solf. 1984) can easily be seen.

All these observations support a model of the Cep A cloud core as consisting of one or several recently formed stars embedded in a disk or torus-like molecular cloud that makes them invisible at optical and near-IR wavelengths. This central star (or group of stars) drives the bipolar mass outflow (mainly CO and HCO⁺) and scattered light off the innermost parts of the cavity created by this outflow is then observed as a near-IR reflection nebula, Cep A IRS 6.

At the centre of the bipolar outflow a cluster of ultracompact H II regions has been found, one of them (HW2) is believed to be the driving source of the outflow.

There is a vast amount of diffuse interstellar dust present in the vicinity of Cep A, producing emission in the IR mainly due to PAHs. This emission is clearly visible in ISOCAM images as bright 'nebulous' features, including several bright arcs (appendix E).

The Cep A region observed with ISOCAM is ~0.09 square degrees centred on the Cep A molecular cloud core.

1.6 About this master thesis

This master thesis is very much an observational one, treating star-formation and star classification from an observational point of view. It is based on the ISOCAM observations

recently carried out with the ISO-satellite, as part of its survey of nearby star-formation regions.

Chapter 1 deals with concepts used in the discussion of the ISO-sources and also contains some introductory information on the region observed.

Chapter 2 introduces the ISO-satellite and its camera, called ISOCAM.

Chapter 3 deals with the reduction of the ISOCAM observations as well as point source detection and photometry.

Chapter 4 presents the results from the ISO-data, including a list of all detected stars, the classification of these and a discussion of the thereby found YSO-candidates.

Chapter 5 is devoted to my visual/near-IR observations, in this chapter the data is reduced into two mosaics which are then used for identification and photometry of the ISO-sources, using an aperture photometry program that I have written for the purpose. This data is used to help in the classification of the ISO-sources and to find additional mid-IR excess sources (not seen in the ISO LW3 filter and therefore previously not classified).

Chapter 6 contains additional near-IR observations (J, H and K_S passbands) used to further aid in the classification of the ISO-sources and detection of mid-IR excesses not seen in the ISO-data.

Chapter 7 contains a summary of the results obtained in this master thesis, including a list of all ISO-sources classified as having intrinsic mid-IR excess (YSO-candidates) and an estimation of their mass spectrum.

In **Appendix A**, a 'program' is supplied of a typical ISO-data reduction (one raster). **Appendix B** contains an aperture photometry program that I wrote for my optical and near-IR observations. **Appendix C** is a vocabulary of important acronyms and scientific words used in this report. The mosaics of my optical and near-IR observations are presented in **Appendix D**, and finally, the ISOCAM mid-IR mosaics are found in **Appendix E**.

2. An introduction to ISOCAM

In this chapter, the characteristics of ISOCAM and all its detectors, filters etc. are treated (for completeness) even though only one detector array (LW), two filters (LW2, LW3) and two PFOV's (3" and 6") were used for the Cep A ISOCAM data.

2.1 The ISO-satellite

The IRAS (InfraRed Astronomical Satellite) project (the predecessor of ISO) was a collaborative effort by NASA (USA), NIVR (Netherlands) and SERC (UK). It conducted an all-sky survey using a liquid helium cooled 60 cm Richey-Chrétien telescope at wavelengths ranging from 8 to 120 microns in four broadband photometric channels, centred at 12, 25, 60 and 100 microns. Following a 10 month mission IRAS exhausted its cryogen and ceased operations on November 21, 1983. IRAS angular resolution varied between $\sim 0.5'$ at 12 microns and $\sim 2'$ at 100 microns. The IRAS mission was then followed by the ISO mission which provided a much higher angular resolution.

The ISO (Infrared Space Observatory) satellite, a project of the European Space Agency (ESA), was launched on the 17th of November 1995 by an Ariane 4 rocket into a highly elliptical orbit with a perigee at 1380 km and an apogee at about 70000 km.

ISO's orbit had a period of 24 hours which made it possible to have continuous contact with ISO from a ground station on Earth, this is necessary since there were no on-board storage of scientific data.

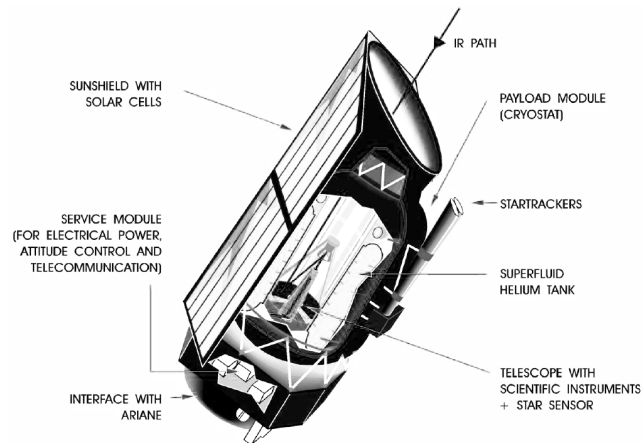


Figure 2-1. The ISO satellite.

About eight hours a day, when the satellite is low in its orbit, it lies within Earth's Van Allen belts of radiation where the majority of ISO's detectors are scientifically unusable due to effects caused by radiation impacts. During the 16 hours a day outside these belts all detectors could be operated.

Several fields of astronomy can benefit from ISO since it provides astronomers with a unique facility of unprecedented sensitivity for a detailed exploration of the universe ranging from objects in the solar system to the most distant extragalactic sources. The spatial extent of ISO's mission includes only selected parts of the sky (as supposed to IRAS), these regions were chosen with the aid of the IRAS all sky survey. There were four instruments available onboard ISO: Short Wavelength Spectrometer, Long Wavelength Spectrometer, imaging photo-polarimeter and ISOCAM which is the instrument that was used for the ISO observations in this master thesis.

The ISO telescope is a 60 cm diameter Richey-Chrétien system with an overall focal ratio of $f/15$, the optical quality of the primary and secondary mirrors provides diffraction-limited performance at wavelengths beyond 5 microns (however, the pointing performance limits diffraction-limited use to wavelengths longer than about 10 microns). A part of the 20' unvignetted field of view of the ISO-telescope is distributed into the entrance pupil of each instrument by a pyramidal mirror located on the telescope axis, this provides each of the four instruments (e.g. ISOCAM) with a 3' unvignetted field of view.

Pointing and tracking is performed on guide stars (apparent visual magnitudes between 2 and 8) using the two star-trackers mounted outside the cryostat. These guide stars are distributed over the entire sky and it is expected that at least one of these stars will be present in the $3^\circ \times 4^\circ$ field of view available to the CCD detector of the operational star tracker. Possible misalignments between the telescope and the star trackers are periodically measured and corrected for, using a star sensor located on the optical axis of the telescope.

The lifespan of ISO ended at 14.00 CET on May 16, 1998, when it was switched off and 'de-orbited' to lower the perigee from 1380km to 715km, probably causing the satellite to re-enter Earth's atmosphere in about 20 years time. This was done since ISO had run out of its liquid helium supply on April 8, 1998.

Between April 8 and May 16 1998 however, some gaps in the previous observations were filled using the shortest wavelength detectors of the SWS instrument. During this time period there were also some detailed tests of unused software and hardware, not used during the operational phase due to the superb performance of the ISO-satellite. These tests were conducted so that more knowledge about the software and hardware could be gained for future ESA missions, using partly the same equipment (e.g. XMM and Integral, which uses similar star trackers).

2.2 An overview of ISOCAM

ISOCAM is the instrument onboard ISO designed to map selected areas of the sky in the IR spectral region from 2.5 to 17 μm at various spatial and spectral resolutions. Observations made with ISOCAM are just impossible to replicate with ground-based observations due to the spectral region used, ISOCAM is also able to do polarization mapping. The spatial resolution is limited by diffraction at longer wavelengths and by the pointing of the ISO-satellite at shorter wavelengths.

ISOCAM is able to image fields of views of up to 3' in diameter, it consists of two optical channels (SW and LW), one used at a time, each of which contains a 32 x 32 pixel IR-detector array. The short wavelength channel (SW) operates between 2.5 and 5.2 μm while the long wavelength channel (LW) operates between 4 and 17 μm . The SW and LW channels also includes different magnification lenses and filters.

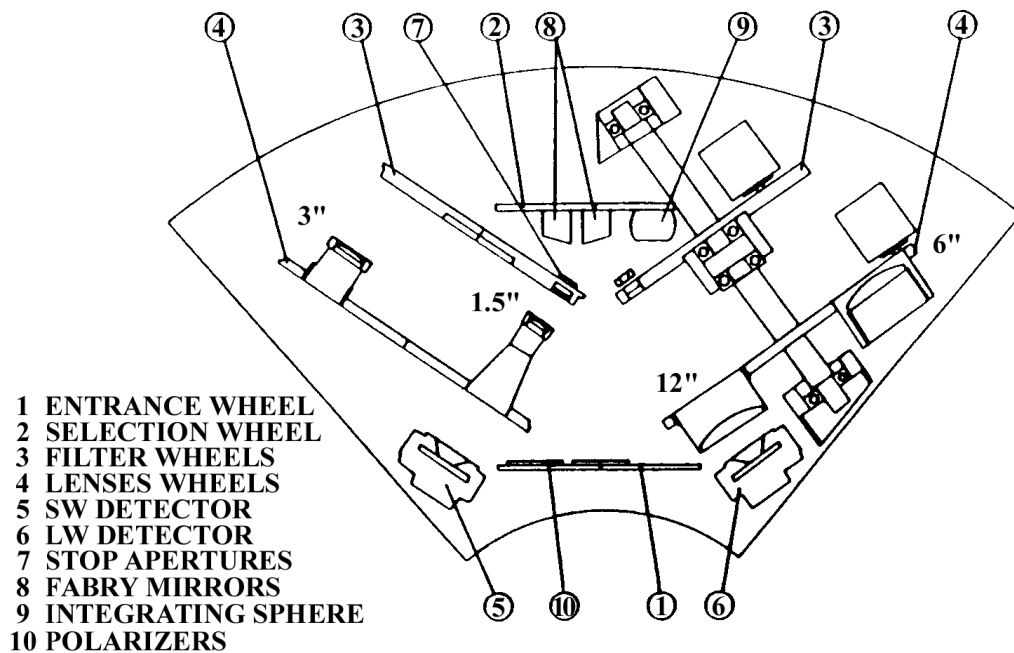


Figure 2-2. Layout of the ISO-satellite's IR-camera: ISOCAM.

ISOCAM's optical design is shown in figure 2-2, radiation enters the camera through the entrance wheel (1) which contains a clear aperture and three polarizing grids (10) with position angles 120° apart.

The selection between the SW / LW channels is achieved by two off-axis field mirrors (8) mounted on the selection wheel (2), these mirrors are placed at the focal plane and depending on which of them is in position, the beam is directed into either the SW or LW channel. Each channel has a filter-wheel (3) and a lens-wheel (4) that reimages the focal plane of the telescope on the selected detector-array (5,6).

The lens-wheels contains four lenses, providing pixel field of views (PFOVs) of 1.5, 3, 6 or 12 arcsec. The field mirror (Fabry mirror) acts as a field stop for the light coming from the telescope, for each channel there are actually two field mirrors providing two different fields (3.3 x 3.3 arcmin and 87 x 87 arcsec).

Since it was not possible to have a broad band antireflection coating on the detectors, the detector back reflected light is a source of stray light. The filters are tilted with respect to the optical axis to avoid strong ghost effects, but the secondary reflection on the wheels and on the filter mounts cause residual ghost images at a level of less than 1% (this changes from one filter to another). The worst case is for the 3'' PFOV where light coming from the whole 3' field of view falls on gold connecting strips on the edges of the photosensitive part of the detectors. To decrease this effect, a smaller field mirror has been designed which define a field sizeable with the array field of view. In the flight configuration only 29 x 29 pixels are illuminated with this small field mirror and the 3'' lens.

The telescope itself provides a 3 arcmin diameter field of view that is unvignetted. With the 1.5 and 3 arcsec PFOVs only the central part of the telescope's field of view is used by ISOCAM, the field of view of the camera is then limited by the size of the array. For the 6 arcsec PFOV, there's some vignetting (up to 40%) in the corners of the 3 x 3 arcmin square field of the array since the system has been designed to match the 3 arcmin diameter unvignetted field of view of the telescope. With the 12 arcsec PFOV, the field stop is always the field mirror, and the outer part of the detector-array is not illuminated. By combining the available field mirrors with the available PFOV's it's possible to obtain camera square fields from 45'' x 45'' (small field mirror, 1.5'' PFOV) up to 3.3' x 3.3' (large field mirror, 12'' PFOV) as shown in table 2-1.

Table 2-1. *ISOCAM - Possible combinations of field mirrors and magnification lenses.*

PFOV	Field Mirror	Field	Vignetting
1.5	small	45'' x 45''	No
3	small	87'' x 87''	No
3	large	1.5' x 1.5'	No
6	large	3' x 3'	Up to 40%
12	large	3.3' x 3.3'	Outer part of detector not illuminated

Due to the off-axis field mirrors, there is a small field distortion. As an example, for the 6'' PFOV, an object which would give an image of 32 pixels on the top of the array would give an image of only 31 pixels in the bottom of the array.

The Point Spread Function (PSF) is a convolution of the diffraction figure of the 60cm telescope with the sky sampling of the PFOV. The PSF is undersampled with the 12'' and 6'' PFOV, although it covers about 2 pixels for the 3'' PFOV and it is well sampled with the 1.5'' PFOV. The PSF is uniform in the circular 3' field of view, but it is somewhat degraded in the corners of the square 3' field of view.

2.3 Available filters and arrays

As mentioned previously the ISOCAM has two different arrays: the SW array which operates between 2.5 and 5.2 μm , and the LW array which operates between 4 and 17 μm . There are 11 different SW-filters (SW1-SW11) and 10 different LW-filters (LW1-LW10) available for band pass imaging, there are also three Circular Variable Filters (CVF), one for the SW-array and two for the LW-array.

All of my work with the ISO-data involves only the LW array (almost all imaging ever done with ISOCAM used only the LW array, mainly because of its more exotic wavelength range compared to the SW array). The SW array will only be mentioned below while the LW array is concerned for the remainder of this master thesis.

The SW array is an InSb 32 x 32 pixel Charge Injection Device (CID) manufactured by the Société Anonyme des Télécommunications. It complies with the demands of the ISO-mission of low operating temperature and a large radiation tolerance. A control and readout hybrid

electronic was designed to work at 4K, close to the chip. The array and its cold electronics are housed behind a titanium cover which provides a shield for radiation and stray light. Including the 89% filling factor of the 100x100 μm pixels and the charge injection efficiency the effective quantum efficiency is 0.3 at 4 μm , with a flat curve towards shorter wavelengths and a cutoff at 5.2 μm .

At first when ESA called for "proposals for ISO instruments" there were no LW array with the needed requirements available in Europe! A specific development was undertaken at the Laboratoire d'imagerie Infrarouge du CEA-LETI in Grenoble, they came up with a 32 x 32 pixel Gallium doped Silicon photoconductor array hybridized by Indium bumps to a direct voltage readout circuit.

The pixel pitch is 100 μm and the detectors are 500 μm thick. A 25 V bias voltage is applied to the photoconductor which provides the optimum trade off between responsivity and stabilization overhead. With this bias voltage, the responsivity at 15 μm is 10^{14} V/W which corresponds to a photogain-quantum efficiency product of ~ 1 . In first approximation, at shorter wavelengths the responsivity decreases as λ and there is a long-wavelength cutoff at 18 μm . To obtain a 100% filling factor, the front surface is doped to ensure a good electrical surface conductivity and the bias voltage is applied to an Aluminium frame on the side of the optical sensitive area. An external guard (3 pixels wide) has been added around the 32 x 32 sensitive frame to prevent field line distortion in the detectors at the edges. The optical crosstalk is very low, it remains below 1.5% even for the 12" PFOV which has the fastest lens ($\approx f/1$) of ISOCAM.

All the ISO data that I have used for Cepheus A was observed with the LW detector array, using the two filters LW2 and LW3. In figure 2-3, the transmission of ISOCAM is plotted for these filters.

The LW2-filter transmits IR light between ≈ 5.00 -8.50 μm (half maximum transmission points) with a centre at 6.7 μm (dashed line), its spectral resolution $R = \lambda/\delta\lambda \approx 2$.

The LW3-filter transmits IR light between ≈ 12.0 -18 μm with a centre at 14.3 μm (dashed line), its spectral resolution $R \approx 3$.

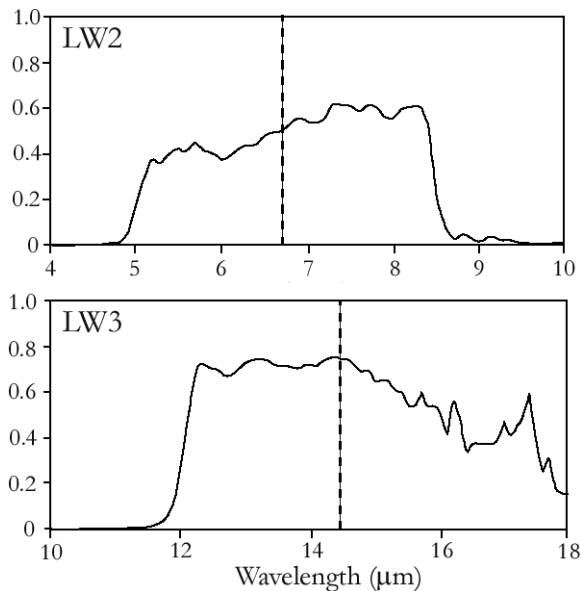


Figure 2-3. The quantum efficiency (times the photoconductive gain) for the LW2 and LW3 filters. Normalized to 1.0 at 9 μm .

2.4 Readout sensibility

For every pixel in the 32 x 32 array, the readout circuit has an integration capacitance of 0.12 pF and a MOSFET follower stage with a gain of 0.8. A double sampling readout scheme is used, first resetting the output capacitance and measuring this reset level, then integrating and measuring the resulting level after this integration. The reset-level and end of integration level are then stored and transmitted to Earth in two separate frames (32 x 32 pixel frames).

Available integration times in flight are limited by the onboard acquisition system (lower limit) and the glitch rate induced by cosmic rays (upper limit). Available integration times are: 0.28, 2, 5, 10 and 20 seconds.

The noise of the ISOCAM-array in the LW-channel consists of three components: A high frequency part that is well approximated by a constant readout noise of ~ 180 e⁻/pixel rms added to the photon shot noise, a low frequency part which becomes important after several tens of readouts. At high level ($>10^6$ e⁻/pixel) an amplifier noise becomes dominant and limits the S/N ratio to ≤ 500 in a single exposure. The best performance is obtained with a signal between $2 \cdot 10^4$ and 10^5 e⁻/pixel.

For all integration times the output signal is linear with the incoming flux up to $6 \cdot 10^5$ e⁻/pixel and saturates above $1.5 \cdot 10^6$ e⁻/pixel. For an integration time longer than 1 sec the output signal is proportional to the integration time, for a shorter integration time there is a small variation of the responsivity, this is taken into account in the data processing.

For each column of the 32 x 32 LW array there is an independent channel in the readout electronic. An analog multiplexer is used to read each line and to encode the signal on 4096 ADU-levels. A programmable offset (bias) is automatically applied before the AD-converter, where a x1, x2 or x4 gain (x1 in all Cep A obs.) can be chosen by the observer to take full advantage of the dynamical range and to obtain good sampling of the noise in low flux conditions. A gain of 2 is normally used, this provides 120 e⁻/ADU and an acceptable sampling of the 1.5 ADU rms of the readout noise over the whole linear range of the array. This gain limits the AD-converter to $\approx 5 \cdot 10^5$ e⁻/pixel (a x1 gain is usually selected for stronger signals).

There is also a "dead column" in the LW array (column 24), the pixels in this column does not have any sensitivity at all but since almost every observed sky position has been observed more than once (overlapping images) any source that lies on the dead column in one image is often visible at a good column in another image.

In all images taken with the LW array there is a signal variation between odd and even lines, this so called "dark pattern" can be suppressed and correct for in the data processing².

² See dark pattern removal, chapter 3.3.

2.5 Effects of charged particles

There are two cases in which the LW array is affected by charged particles, producing either response variations or glitches (streaks across images due to impacts with particles). The response variation can occur when ISO resides in the van Allen belts and is subject to a very high radiation dose coming from trapped electrons and protons within these belts.

Since ISOCAM is not used within the van Allen belts there are no direct problems, however the ionizing radiation obtained when passing through the belts induces a responsivity increase which relaxes in a few hours. This effect is minimized if the photoconductor is polarized and exposed to a high IR flux, therefore during the perigee passage a specific power supply keeps a bias voltage on the photoconductors and ISOCAM is left open to light. This procedure keeps the responsivity variation below 5% in the usable part of ISO's orbit.

The main perturbation during the usable part of ISO's orbit comes from glitches. These are caused by external sources: galactic protons and α particles (depending on solar activity), or internal sources: Thorium in the antireflection coating of the lens which generates a flux of low energy α particles. Less frequent, but more damaging are the heavy ions, each ion affects ~50 pixels and will generate a glitch followed by a decrease of responsivity. Heavy ion and proton glitches can easily be removed from observations by using a filtering technique in the data processing (provided that enough exposures has been taken for each observation).

2.6 Transient and memory effects

When pixels in the LW array experience large flux changes (resulting in charge changes on the detector pixels) there is a time lagged response with characteristics that depends on the initial and final accumulated charges. Because of the small size of the array (32 x 32 pixels) it is necessary to make rasters, combining several individual images at different spatial positions. The lagged response often shows up as several "ghost sources" in successive spatial images of a previously exposed bright source that in reality only exists in the image where it first turned up. These ghost sources (often bright areas) looks like fading echoes of the real source. The intensity of the first ghost source (echo) depends on the flux step by the source, for each readout (one 32 x 32 pixel frame) the ghost source gets dimmer.

An analysis of 50 cases during the calibration of ISOCAM (ISOCAM Observer's manual. 1994) before the ISO-satellite was put into orbit yielded the following stabilization relation of the LW-array:

$$N_{\text{Stab}} = N_0 \cdot \frac{|\text{TO} - \text{FROM}|^\alpha}{(\max[\text{TO}, \text{FROM}])^\beta}$$

where $N_0 \approx 275$; $\alpha \approx 0$ and $\beta \approx 0.60$. This relation gives stabilization times typical of those in figure 2-4. where N_{Stab} is plotted as a function of the destination level (TO) in a flux step from the initial levels 3, 10, 30, 100 and 300 ADUs.

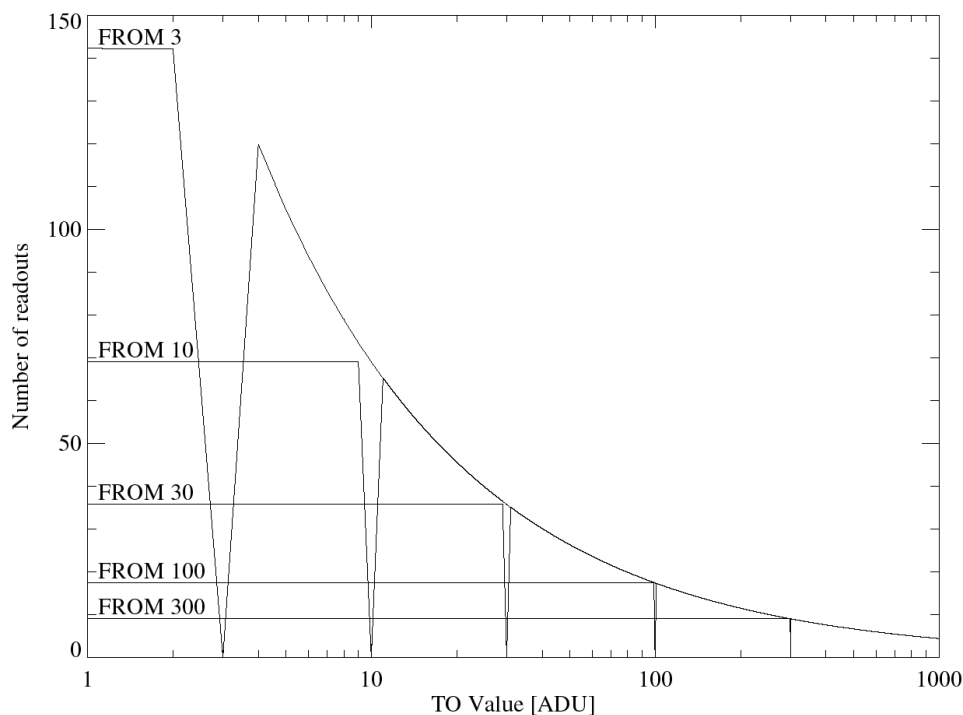


Figure 2-4. *LW transients: Number of readouts for stabilization at 90% after a flux step from 3, 10, 30, 100 or 300 ADUs.*

This "ghost effect" means that different pixels have different responses to a given flux step, which results in a degraded flatness of the images following this step. For every readout the signal gets more stabilized and at least 20 readouts are often needed for the signal to stabilize, but of course, larger flux steps requires longer stabilization times.

Signal stabilization after changes of flux or integration time is the main problem encountered with the LW-array, the worst situations occur in the following two cases: illuminating the array previously at dark or after a saturating flux. The first problem can be overcome by always keeping light on the array and sorting the sequences of observations by decreasing flux. In the second problem, the array can have memory-effects of the saturating scene for a period as long as half an hour. To keep this memory image from polluting the following observations, one can saturate the whole array with an ICD flash for a couple of readouts, this causes the array to loose its memory of the previous scene, however the overall responsivity of the array is degraded for up to 10 minutes.

There exists a pretty complicated software routine that corrects transient effects, this correction procedure requires a lot of time, however it gets rid of all but the strongest transients.

2.7 Flatfielding

Due to different sensitivities in the 32 x 32 pixels of the LW-array every image has to be corrected for this by a procedure called flatfielding, where a normalized image without any sources, called a flat-field, is calculated. All observed images are then divided by this

flatfield, giving an image in which all pixels are almost equally flux-sensitive. If the signal is stabilized this method gives a very good flatfield accuracy, however this is almost never the case since the signal takes too long to stabilize and the observer has to make use of the images obtained in still unstable configurations resulting in transient effects.

Although the transient effects can not be removed by flatfielding, it effectively reduces vignetting and other response inhomogenities intrinsic to the LW array. Vignetting occurs when a high PFOV is selected, and response inhomogenities exists especially at the edges of the array and in a line of pixels in the lower left hand side quadrant of the array, where the responsivity is slightly lower than average.

3. Processing of the ISOCAM data

The ISO observations that I have used concerns five different regions close to the molecular cloud core Cepheus A. For every region, observations have been carried out with the LW array, using both the LW2 and LW3 filters (yielding ten rasters).

Four regions (CepA W, CepA E, CepA CN and CepA CS) used a PFOV of 6'' while the central region (CepA CC) was examined in greater detail using a PFOV of 3''. All observations used a 1x gain and no beam switching. The central region is so bright that an integration time of 0.28 seconds had to be used (four exposures for each frame), while all other regions used an integration time of 2.1 seconds.

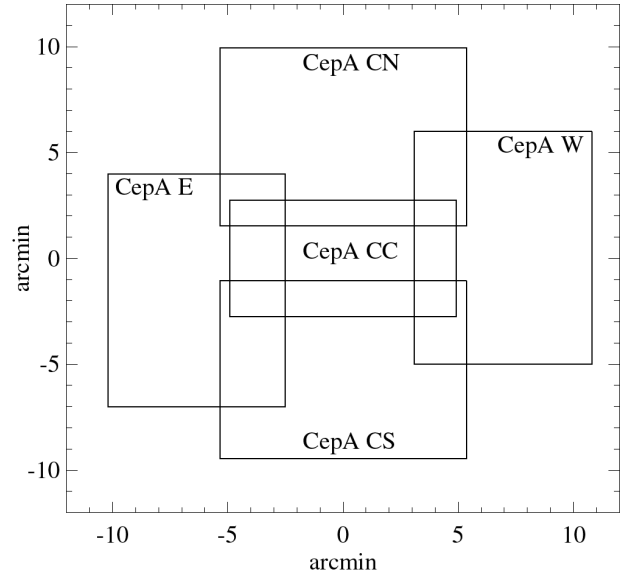


Figure 3-1. The five regions of the Cepheus A ISOCAM observations, each consisting of an array of images.

In table 3-1 below, all observed rasters around Cep A are shown with grid size (M x N), grid step (ΔM , ΔN), PFOV, used filters, exposure times and coordinates (using epoch 2000). The observation dates are also shown.

Table 3-1. ISOCAM observations of the Cepheus A region

Region	M x N	ΔM	ΔN	PFOV	Filter	Exp.Time	RA (2000)	DEC (2000)	Date
CepA W	4 x 4	90''	156''	6''	LW2	2.1 s	22h 55m 23.0s	62° 01' 01.5''	970827
CepA W	4 x 4	90''	156''	6''	LW3	2.1 s	22h 55m 23.0s	62° 01' 01.5''	970827
CepA E	4 x 4	90''	156''	6''	LW2	2.1 s	22h 57m 16.5s	62° 03' 03.8''	970827
CepA E	4 x 4	90''	156''	6''	LW3	2.1 s	22h 57m 16.5s	62° 03' 03.8''	970827
CepA CN	6 x 3	90''	156''	6''	LW2	2.1 s	22h 56m 17.0s	62° 08' 17.6''	970827
CepA CN	6 x 3	90''	156''	6''	LW3	2.1 s	22h 56m 17.0s	62° 08' 17.6''	970827
CepA CS	6 x 3	90''	156''	6''	LW2	2.1 s	22h 56m 17.3s	61° 57' 17.6''	970827
CepA CS	6 x 3	90''	156''	6''	LW3	2.1 s	22h 56m 17.3s	61° 57' 17.6''	970827
CepA CC	12 x 4	45''	78''	3''	LW2	4x0.28 s	22h 56m 17.1s	62° 02' 32.6''	970809
CepA CC	12 x 4	45''	78''	3''	LW3	4x0.28 s	22h 56m 17.1s	62° 02' 32.6''	970809

For every observed raster, an array of 32x32 pixel images were used, either 4x4 (W, E) ; 6x3 (CN, CS) or 12x4 (CC) images. For every used image there are at least 13 exposures (frames), providing records in time for how each pixel changes, making it possible to remove glitches later in the processing stage.

Since the camera (ISOCAM) never stops observing during sessions, not even while ISO is slewing to a new target, some observations (those with only a few exposures) and wait-exposures (waiting for ISOCAM to change filters, lenses etc.) have to be removed from the

data-set prior to the data processing. Each field is observed in a "zig-zag" manner, see table 3-2 below for an example of the observing procedure. M and N are the coordinates in the raster grid, $1 \leq M \leq 6$ and $1 \leq N \leq 3$ in this session because a 6x3 grid was used.

Table 3-2. *ISOCAM observing session of the Cep A, CN, LW3 raster*

M	N	Exposures	ISOCAM status
1	1	2	<i>Waiting... (changing filter etc.)</i>
1	1	2	<i>Waiting...</i>
1	1	2	<i>Observing (later removed with x_slicer)</i>
1	1	1	<i>Observing (later removed with x_slicer)</i>
1	1	2	<i>Observing (later removed with x_slicer)</i>
1	1	85	Observing with LW3 (Stabilization)
2	1	16	Observing with LW3
3	1	16	Observing with LW3
4	1	16	Observing with LW3
5	1	16	Observing with LW3
6	1	16	Observing with LW3
6	2	17	Observing with LW3
5	2	16	Observing with LW3
4	2	15	Observing with LW3
3	2	17	Observing with LW3
2	2	16	Observing with LW3
1	2	16	Observing with LW3
1	3	17	Observing with LW3
2	3	15	Observing with LW3
3	3	17	Observing with LW3
4	3	16	Observing with LW3
5	3	16	Observing with LW3
6	3	14	Observing with LW3
6	3	1	<i>Waiting...</i>

3.1 The data calibration procedure

Most of the data processing was carried out with a software package called CIA³, written in the high-level language IDL (developed by Research systems, Inc.).

The data processing steps that I used on the Cep A data are reproduced in Appendix A (a 'program' written in the IDL-language), these steps are described in greater detail in the rest of this chapter. Throughout the 'program' the name "data" is often used, this is the name of the data that is being calibrated and it is a good idea to include the region and filter names. In my case I have used names like "e_lw2" (CepA East, filter LW2) , "e_lw3", "w_lw2", "cn_lw3" etc.

³ CIA (version 3.0) is the ISOCAM Interactive Analysis system, jointly developed by the ESA Astrophysics Division and the ISOCAM Consortium as the tool adapted to ISOCAM's particular scientific and engineering data processing requirements.

3.2 The ISOCAM data formats

There are some important data formats that are essential in the understanding of the original data format on which all ISOCAM data is built upon. First of all, every exposure (32 x 32 pixel elements) is called a 'frame'. There are often a lot of frames at any observed spatial position in order to avoid saturation and to obtain information on how the pixels intensities changes with time. This is important since it helps separating glitches from real point sources in the data processing. The frames are situated in a three dimensional array, a 'cube', that has the size 32 x 32 x number of frames.

For every observed spatial position there is only one 'image', it is defined as the mean of all frames at that spatial position. The images are stored in a three dimensional array that has the size 32 x 32 x number of images (image cube). Corrections are sometimes made to the frames and sometimes directly to the images. If a correction is applied to the cube (i.e. the frames) it often has to be reduced to images before the effects can be seen correctly.

At larger scales the used format is called a 'raster', this is a two dimensional array consisting of all the images in a specific region/filter combination (e.g. West, LW2) using the correct spatial positions and rotations. One can say that a raster is an image of the whole region using one of the filters.

At even larger scales, rasters are put together in a 'mosaic'. I will obtain four mosaics, one for each filter using two areas. The rasters that are used in a mosaic are often overlapping, the overlapping pixels are calculated as a mean value of all overlaps. Images in a specific raster are also overlapping each other, the pixels are calculated in the same manner as for overlapping rasters.

There is also a special type of data structure used in the CIA package, much like the filesystem on a computer, where variables are stored under categories and sub-categories separated by a dot. For example, the images in a raster are often temporary situated in an array called 'tmp.image' while the equatorial coordiantes for these images are stored in two arrays called 'tmp.info.ra' and 'tmp.info.dec'. The command "hs" is used in CIA to view a structure or a sub-structure, for example "hs, tmp" or "hs, tmp.info" is used to list all variables under the structure 'tmp' and the sub-structure 'tmp.info'. The mostly used structure, tmp, is a temporary structure to which all alterations are done, this structure is later saved under another name when a successful alteration has been done.

3.3 Dark correction

As mentioned previously there is a signal variation between odd and even lines in the LW array, this so called 'dark pattern' can be suppressed and correct for by a method called 'dark pattern removal'. At this stage, it is only necessary to do a first-order dark correction in which a linear relationship is assumed between the output signal and the input signal (real signal + dark image).

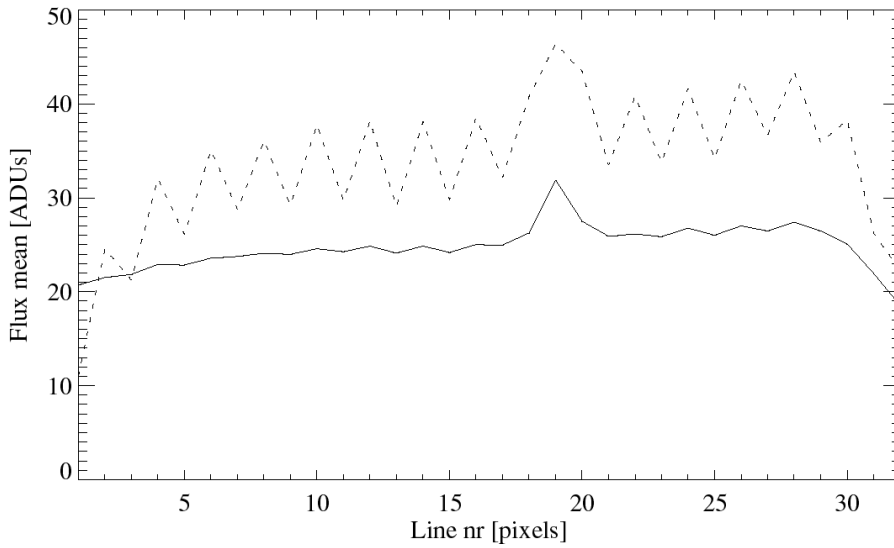


Figure 3-2. *Even/Odd line flux-variations, calculated from the mean flux [ADUs] of each line, using all frames in the CepA CN region (LW2 filter). The dashed curve is before and the solid curve after the dark correction.*

This first order correction is just a matter of subtracting the correct dark-frame from the frames in the data-cube, this is done by calling a subroutine called "calib_raster" with the keyword "dark" set. The subroutine uses the most suiting dark chosen from the CAL-G DARK library, which is a library containing a lot of dark-frames taken regularly in orbit. The best available dark frame has been chosen earlier, when the original data was created from the "sscd".

Usually the striped odd-even pattern is now gone (figure 3-3). However for some rasters this simple procedure is not enough. This sometimes makes it necessary to do a second order dark correction, see chapter 3.5.

A first order dark correction was sufficient for all rasters except the two rasters in the central (CepA CC) region.

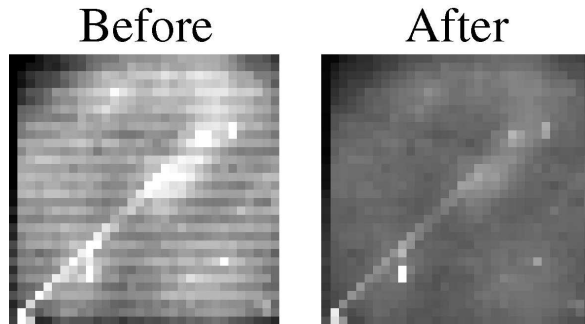


Figure 3-3. *Dark correction of a frame (LW2) in the Cepheus A, CN region.*

3.4 Glitch correction

There are various methods available to remove glitches caused by impacting particles, almost all of these deglitching methods involves some kind of median-filtering or a median transform.

One of the better methods, probably the best yet for regions with many exposures for each spatial position is the MMT deglitching method which I have used to calibrate the data in the Cepheus A region.

The MMT (Multiresolution Median Transform) deglitch method, proposed by Starck et al. (1996), is a non-linear multiresolution transform which works by the principle that glitches are small scale structures which only exists for a short period of time compared to the large scale structures of the source signal. This implies that if we observe the same position in the sky during several exposures, then any significant structure in our signal that has a temporal size less than the total exposure time is a glitch.

This method also seem to handle non-stabilized data very well, it is especially good for observations where many frames are used. At least four exposures for each position is usually required to properly deglitch the data, however for short exposure times (e.g. 0.28 seconds) as many as 16 exposures or more are often required.

After the MMT-deglitching there are almost never any signs of glitches, as can be seen in figure 3-4. The signal and noise are however not modified by the deglitching procedure.

The only real limitation of this method is that it is unable to detect glitches which lasts longer than the total exposure time for a position in the sky, this setback can only be avoided by including enough frames to properly deglitch the data, which has been done for all Cepheus A observations.

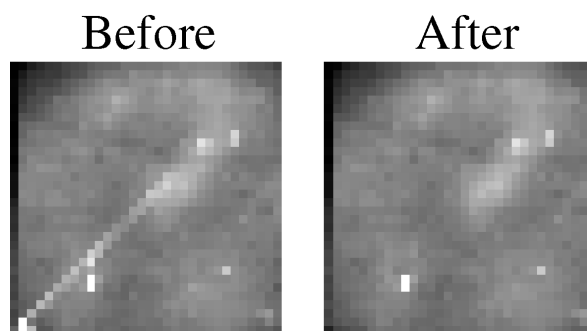


Figure 3-4. *Glitch correction of the dark corrected frame presented in figure 3-3. The glitch streak clearly visible in the left image has effectively been deglitched in the right image by the MMT method.*

Of course, this method only removes the streaks caused by impacting particles for the concerned images, but there is still a responsivity variation caused by these glitches that effects the exposures following a glitch. A perfect deglitch method would therefore be one that associates the glitches found by the MMT to a model which corrects for the gain variation following a glitch.

3.5 Second order dark correction

Sometimes, in a particularly difficult raster, the first order dark correction using the dark library is not sufficient, as was the case for the central rasters of Cepheus A. This calls for a second order dark correction, in which a Fourier transform is applied to the images, motivated by the fact that the odd-even line pattern in the images looks like oscillations.

This means that the ‘dark images’ also oscillates between lines with a period of two pixels (two lines), therefore its fourier representation shows a highly peaked component which is easy to suppress. After the elimination of low frequencies in the Fourier transform (mainly the background) and thresholding of all Fourier coefficients lower than three times the noise, it is possible to obtain the remaining dark-pattern by calculating the inverse FFT which gives the dark-pattern as its real part.

When this has been carried out on all images, the resulting raster will show if the correction is enough to completely suppress the odd-even line intensity variations. If the correction is enough, it must be applied to each frame in the entire cube, as for now it has only been used on the images in the raster, which are based on the frames in the cube, that is why all permanent corrections must be applied to the cube and not the images.

Prior to the second order dark correction, one of the images is chosen to represent the raster, this image should contain as few and weak sources as possible and have neglectible nebulosity. When the dark-pattern of the represented image has been calculated, it is subtracted from all the frames in the cube. This dark-pattern should have a clear odd-even line intensity variation (stripes) with no other structures visible since it has been calculated from the image with the easiest removable signal (the emptiest image).

An advantage of this method, using the FFT thresholding, is that it will always find a residual dark image with a mean value of zero, thus the correction just suppresses the striped artefact pattern and does not add any offset to the real data.

3.6 Transient correction

When pixels in the LW array have been subjected to large flux changes as is the case when viewing bright sources, there is a time-lagged response which shows up as ‘ghost sources’ in the images following the flux change.

These artefacts are often (more or less) removed in the transient correction, as can be seen in figure 3-5 where the transient correction successfully has suppressed a ‘ghost image’ of a previously observed, strong source.

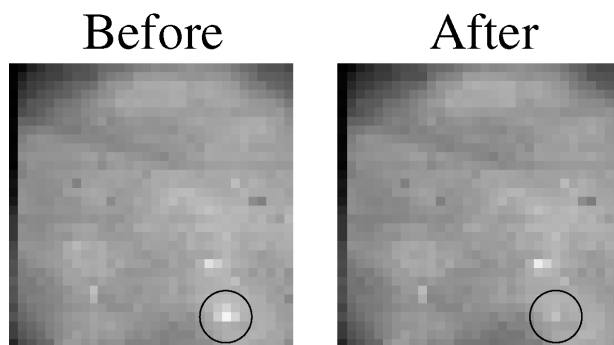


Figure 3-5. *Transient correction of an image in the Cepheus A, CN region, using the IAS inversion model. The circled transient artefact is almost completely removed by the transient correction (right image).*

For very bright sources like the core of Cepheus A in the centre raster, the ghost sources could only be partially removed. There are several methods available for transient corrections, however a routine using the ‘IAS transient model’ was used for all rasters. The IAS-model⁴ suppresses the frames or the pixels which do not seem stabilized in time.

At first, a cube called ”precube” is defined that contains 200 median-images of the frames from the uncorrected cube, multiplied by the integration time. Then a cube called ”ias_cube” is defined, that contains the precube and the uncorrected cube (also multiplied by the integration time). The transient corrections then uses the ias_cube for the IAS-model calculations resulting in a similar, but transient-corrected cube called ”trans_cube” (which

⁴ For more information on the IAS inversion method (version 10) see Starck et al. 1999.

also contains the precube). These calculations takes a lot of computation time, it is therefore important to save the transient corrected data when the calculations are done.

3.7 Masking

At some point in the data corrections, some pixels in the cube are not wanted in some or all of the remaining calculations or included in the final results because they are biased by a combination of unwanted effects, these effects will be discussed in this chapter.

To keep track of masking information, a "masking cube" with as many pixels as the original cube has been defined. This cube contains integers that describes the masking state of each pixel, every reason for masking a certain pixel has a number (1, 2, 4, 8, 16, ... , 128) that corresponds to a certain bit in the integer number. These reasons (rank) are "added" together to give a unique number for each pixel, describing the masking history for each pixel.

Some pixels are found to be "bad", they are unusable and not wanted in any calculations and certainly not in the final results, they are therefore masked as bad (rank 1) in the masking cube. Since ISOCAM is observing continusly during an observing session, some frames are observed at spatial positions between the target-positions, these frames are masked as bad.

After the transient correction some pixels, often at the edges of a frame, may obtain negative values which of course would harm the following calculations, these pixels are also marked as bad in the masking cube. This occured for the central region "CepA CC" with both filters. This meant that several lines and columns close to the edges of each frame had to be masked as bad.

Due to a hardware problem, known at the launch time of the ISO satellite, there is a 'dead column' at column 24 of the LW array. All pixels in this column are masked as dead (rank 2) for each frame.

Deglitched pixels (rank 4) are also not wanted in the calculations since the original information at these pixels is only available in other frames belonging to the same image or in overlapping images that contains frames without any glitches.

Pixels that are found to be severely affected by transients and memory effects are sometimes found and masked (rank 8) by the transient correction.

There are four more reasons for a pixel to become masked, a pixel that is not illuminated (rank 16), pixels flagged as bad by other flags (rank 32), spare pixels (rank 64) and finally extended source pixels (rank 128).

With all these reasons for masking pixels, it may look like there is going to be voids with information missing, however this is often not the case since every sky position is normally overlapped by two or more images, each containing several frames and it is unlikely that all these frame overlaps has masked pixels for the same sky position!

3.8 Flatfielding

Flatfielding is the final step in the correction of the observed data. This is done in order to make the observed fields "flat", so that a sky region with uniform brightness also should be imaged as flat, almost without any brightness variations. However, without flatfielding this is practically never the case since different pixels on the array have different sensitivities to radiation. Another reason why flatfielding is necessary is that there often is a vignetting (depending on the PFOV) present that decreases the sensitivity of the array circularly towards its edges.

A flatfield is essentially a normalized image without any sources or nebulosity, leaving an image that only includes the array pixels different sensitivities. When this flatfield has been calculated it is used for flatfielding of all the observed frames, this is done by dividing each frame with the normalized flatfield, making all pixels in the frames equally sensitive.

For each region and filter (resulting in ten combinations) I have created the manually best obtainable flatfield, using a subprogram of CIA called "flat_builder" which has all images with the region/filter combination as an argument.

With the help of flat_builder, as many images as possible are chosen that not contain much nebulosity or any intense sources. For each of the chosen images, areas with sources and nebulosity are removed. A flatfield is then created out of the remaining pixels using a median filtering technique. This flatfield is then normalized, using a square region in the middle of the obtained flatfield as a reference.

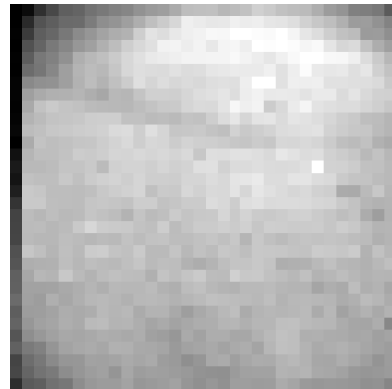


Figure 3-6. Flatfield calculated with the median filtering technique.

Finally, all images in a raster are flatfield corrected by dividing them with the normalized flatfield of the raster. This is done for all 10 rasters of the Cepheus A observations, each using a specific flatfield.

As can be seen in figure 3-7, the flatfield correction 'flattens' an image, making all pixels equally sensitive to radiation. The vignetting effect and 'low sensitivity band' seen in the flatfield (figure 3-6) have almost been completely removed in fig. 3-7 (right).

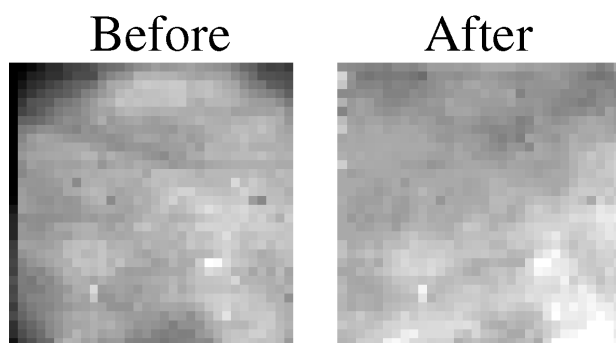


Figure 3-7. Flatfield correction of the transient corrected image presented in figure 3-5.

3.9 Point source detection

Now that all observed data has been corrected, it is time to detect all possible point sources in both the LW2 and LW3 filters for each region. This is often a difficult and very time

consuming effort which involves both 'automatic' and manual detections in a painstaking combination where one needs to be very careful not to overlook any potential sources.

All detections were made in a subprogram of CIA called "det_raster_bus", the detected point sources are then saved to a variable which I have named "data_det".

It is best to start with 'automatic' detection since there are too many potential sources available at first to select them all manually in a logical order. The program first looks for the brightest pixel in the current raster (region/filter combination). When this pixel has been manually investigated, it is cleared from the region by a black square making it one of the weakest pixels to avoid it being detected once again. The procedure is repeated, and the current brightest pixel is found, this procedure is continued until one has cleared out almost all possible point sources.

For each brightest pixel detection, there are usually a number of overlaps available that includes this bright pixel. In order to find out if the pixel belongs to a point source one has to consider a lot of data. The two most important considerations are determining the spatial agreement between all available overlaps and the intensity history of the pixel and the area surrounding it.

When the brightest pixel is found in the raster, its corresponding position is marked at each overlapping image containing this potential point source. It is important to consider if there seems to be a point source close to the marked position in each image, if this is the case, a point source has been **spatially confirmed**.

The second consideration takes advantage of the fact that each image consists of several frames each separated in time by one exposure time. With this information it is possible to consider the intensity variations of the source in each overlapping image containing the central pixel. One has to observe these intensity-curves very carefully, and if they all show convincing signs of a point source the source has been **temporally confirmed**.

If a pixel is both spatially and temporally confirmed then it is a good point source candidate.

A number of facts has to be considered when rating a point source, sometimes an intensity curve shows signs of a point source in one image but not in another overlapping image. This can certainly be the case if the central pixel lies next to or at the dead column in one of the images or if it lies close to the edge of an image.

Even if a source candidate looks like a true source it can also be an extended nebulous "gas knot" or even a glitch or a transient that remained after the glitch and transient corrections. A glitch can often be revealed in the spatial consideration since a pixel often has been observed at different times and different positions on the array for the overlapping images. Sometimes there is just one image that contains the source candidate, in this case it may be possible to reveal a glitch or a remaining transient by finding signs of a decreasing intensity curve.

Another problem during the source detection is that an already considered source may be found again because it is an extended source or a small nebulous area which extends outside the cleared area from the first detection. It is possible to clear different sized squared areas around an already considered pixel but by clearing a larger area one just decreases the possibility of finding a closeby individual source!

At last, when most of the raster is cleared out and has been "automatically" searched it is possible to select possible sources manually in the raster. This may be necessary to examine possible weak sources that would take too long to find using the automatic method but are quite evident candidates by just looking at the raster. The same procedure is used in the manual mode as in the automatic mode when a possible point source is considered.

3.10 Photometry of point sources

Photometry of the detected point sources is carried out on each individual coverage using aperture photometry. The nominal aperture radii are 1.5 and 3.0 pixels for the 6" and 3" PFOV's respectively, however, any aperture radius may be selected. An aperture correction is made by using an empirically calculated PSF in order to take into account the entire flux of a point source, independent of the aperture chosen.

For each point source the photometric flux of each overlap is the median flux from all readouts at that sky position. The flux uncertainties are then calculated from the standard deviation around this median and from the σ of the sky background (defined by an inner and outer sky radius) added in quadrature. The median values for the point source accuracies (1σ) are ~ 1.3 mJy for LW2 and ~ 2.3 mJy for LW3, which also approximately represent the detection limits.

If a pixel is spatially and temporally confirmed then it is a good point source candidate and one choose a confidence value describing how sure one is that the source is a point source. I have used a rating system like this:

1. Most likely a point source ≥ 85 % probability
2. Probably a point source $\sim 50-85$ % probability
3. Doubtful point source ≤ 50 % probability

Also, the flux measurements are flagged if affected by the dead column, detector edges, glitches, memory effects, close neighbours, if the source is extended or lies in a very nebulous area etc.

The source centre is taken to be its peak pixel and a source position is calculated from the redundant images where the source is closest to the centre in order to minimize the effects from field distortion. The average uncertainty in the positions is about $\pm 3''$.

The fluxes in $\text{ADU}\cdot\text{s}^{-1}$ are then converted to mJy through the pre-launch conversion factors $1 \text{ mJy} = 2.191$ and 1.964 ADU/gain/s for the two filters LW2 and LW3 respectively (assuming a source with $F_\lambda \propto \lambda^{-1}$).

An interpolation of the zero magnitude for ground based photometry (Cohen et al. 1992) results in the following relations:

$$\begin{aligned} m_{6.7} &= 12.30 - 2.5 \cdot \log(F_{6.7}) \\ m_{14.3} &= 10.69 - 2.5 \cdot \log(F_{14.3}) \end{aligned}$$

where $F_{6.7}$ and $F_{14.3}$ are given in mJy.

The uncertainties are ~ 0.08 and ~ 0.10 mag. for the $6.7 \mu\text{m}$ and $14.3 \mu\text{m}$ photometry respectively, as estimated from the ISO sources presented in chapter 4.3 combined with the flux uncertainties.

3.11 Correlation between LW2 and LW3 point sources

Now that all point sources have been found and measured by aperture photometry there are two lists of point sources, one for the LW2 mosaics and one for the LW3 mosaics. In order to make one list containing all sources with LW2 & LW3 measurements listed next to each other a correlation is necessary between the two lists.

In order to make a point source correlation between the two filters, a point source's positions in the two filters must not be separated by more than $\approx 15''$ for the $6''$ PFOV regions (outer regions) or more than $\approx 10''$ for the $3''$ PFOV regions (the central region).

The correlation is carried out with a CIA-command called 'crosscornew' yielding an output structure (one list) containing all correlated sources followed by sources not seen in LW3. For each list row (source) there are 25 columns with information on the source's coordinates, fluxes and uncertainties, used aperture and sky sizes, flags etc.

All point sources seen in LW3 were seen in LW2 as well. About 54 % of the sources were seen in the LW3 observations while all sources were seen with the more sensitive LW2 filter.

4. Results of the ISOCAM observations

In this chapter the results of the Cep A ISO-observations are presented. First the resulting four mosaics (LW2 and LW3, two areas) from the data-processing are presented. Then the calibration of ISO source positions is described and the final source list for the Cep A region is presented. Finally, a discussion of the results is carried out using colour-diagrams.

4.1 Mosaics of the Cepheus A region

The outer rasters (East, West, North, South) in the Cepheus A region are now put together into one mosaic for each filter yielding two mosaics of the entire region except for the central raster.

The central raster is much brighter than all other rasters, even saturated at some positions. It is also subject to major transients, unremovable during the transient correction. If all five rasters were put together the overlaps with the central raster would degrade the other four rasters with its large remaining transients, therefore the central region is kept as a separate mosaic. This yields two outer and two central mosaics, one for each filter.

All these mosaics, with the sources circled and numbered according to increasing RA are presented in appendix E.

Except for some very strong central sources, all sources seen in the central mosaic are also seen in the outer mosaic due to sufficient overlaps. It is also apparent that the Cep A region contains a lot of nebulosity, probably dominated by PAH-radiation. There seems to be a lot of 'gas knots' and even nebulous arcs that looks like shock-bows. The Cep A region is a tricky one for photometry at these wavelengths and a chance of source confusion is always present.

4.2 Calibration of source positions

All obtained coordinates of the ISO sources are of course subject to systematic errors, mainly caused by a poor position accuracy of the lens wheel. In order to eliminate these and only keep the unavoidable random errors a constant is added to the RA coordinates and another one to the Dec coordinates.

These constants, δ_{RA} and δ_{Dec} are different for the outer and central mosaics. They are calculated using deviations between the ISO LW2 and the Hubble GSC's coordinates.

The mean deviations are calculated and all ISO coordinates are then calibrated, the same constants are used for the LW2 and LW3 filters. Also, the sine-term involved in smaller RA-circles with greater declination is considered when the RA-coordinates are calibrated.

In order to calibrate the coordinates in the outer mosaic 8 guide stars were used from the HST guide-star catalogue. In figure 4-1, the ISO coordinate deviations are marked with crosses and both the zero deviation point (GSC centre) and the ISO mean deviation point are marked with large plus-signs.

The mean deviations are:

$$\delta_{\text{RA}} \approx +8.2'' \pm 3.0''$$

$$\delta_{\text{Dec}} \approx -5.1'' \pm 1.7''$$

As for the central mosaic, the deviation constants are based on just one guide star (the only GSC-star present!) and are as follows:

$$\delta_{\text{RA}} \approx -3.0''$$

$$\delta_{\text{Dec}} \approx -1.2''$$

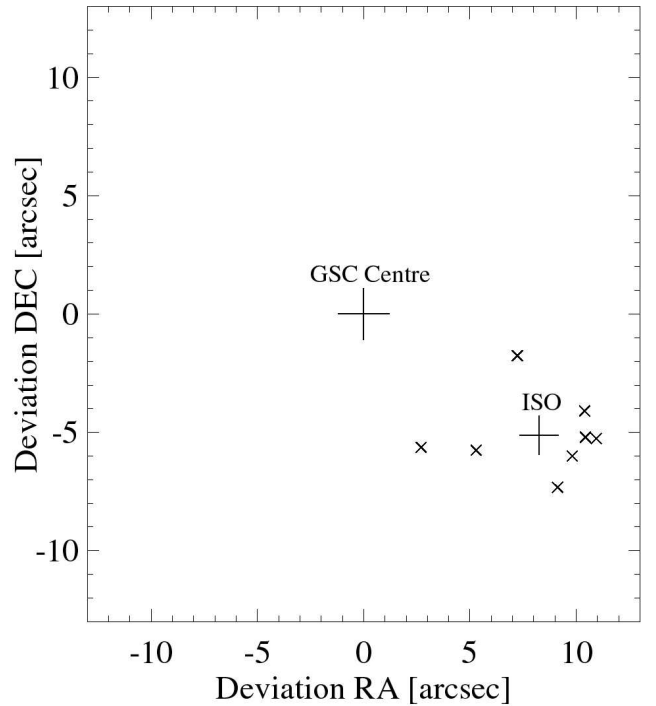


Figure 4-1. Calibration of ISO coordinates: Deviations from Hubble GSC.

4.3 Detected sources

In this chapter, a list of all ISOCAM sources detected in the Cepheus A region is presented. A total of 76 sources were detected in the LW2 observations while only 41 were detected in the less sensitive LW3 observations.

All LW3 sources were also detected in the LW2 observations.

Sources that are classified as 'red' according to their ISOCAM single colour index [14.3/6.7] (see chapter 4.4) are marked with bold source designations in the ISO source table on the following page⁵.

The positional accuracy was determined to be 0.42s (2.94'') in right ascension and 1.64'' in declination (1σ) by using the 8 GSC stars in order to calculate the remaining (random) uncertainties after the systematic errors had been removed.

In the remarks column, 'Binary' means that the source has shown signs of being an optical double star at other wavelengths (see chapter 6.1.1), therefore the counterpart measured by ISOCAM could have the IR-flux of one or both of the components. The remark 'Central M.' indicates that the source is one of the very bright sources only seen in the central mosaic.

⁵ The ISO single colour and SED indices used in the table are described in chapter 1.1.

Table 4-1. *ISOCAM detected sources in the Cepheus A region.*

ISO-Cep	RA (1950)	DEC (1950)	F(6.7) [Jy]	F(14.3) [Jy]	[14.3/6.7]	$\alpha_{6.7-14.3}$	Remarks
1	22:52:56.5	61:43:38	0.018				
2	22:53:06.7	61:45:43	0.626	0.140	-0.65	-2.97	
3	22:53:07.8	61:49:33	0.0095				
4	22:53:07.3	61:46:15	0.012				
5	22:53:12.8	61:48:04	0.0079				
6	22:53:13.1	61:45:10	0.0233	0.0046	-0.70	-3.13	
7	22:53:16.8	61:40:20	0.0059				
8	22:53:23.5	61:42:55	0.0088				
9	22:53:25.0	61:47:59	0.0064				
10	22:53:25.8	61:48:57	0.0198	0.0158	-0.10	-1.30	
11	22:53:25.8	61:46:03	0.0156				
12	22:53:26.9	61:41:04	0.0129				
13	22:53:27.7	61:46:37	0.0134				
14	22:53:30.3	61:47:41	0.0120				
15	22:53:32.0	61:49:15	0.139	0.0904	-0.19	-1.57	
16	22:53:32.8	61:44:20	0.0037				
17	22:53:33.1	61:46:56	0.0085				
18	22:53:40.5	61:47:52	0.0309				
19	22:53:43.0	61:40:22	0.0263	0.0083	-0.50	-2.53	
20	22:53:43.4	61:38:08	0.0509	0.0125	-0.61	-2.85	
21	22:53:44.1	61:48:39	0.0167	0.0257	+0.19	-0.43	Binary
22	22:53:44.6	61:46:38	0.0229				
23	22:53:45.1	61:44:33	0.0050				
24	22:53:47.8	61:41:38	0.140	0.0343	-0.61	-2.85	
25	22:53:49.7	61:46:15	0.0284				
26	22:53:51.2	61:44:23	0.237	0.708	+0.48	+0.44	
27	22:53:52.4	61:54:01	0.0249	0.0082	-0.48	-2.47	
28	22:53:53.4	61:54:32	0.419	0.118	-0.55	-2.67	
29	22:53:57.9	61:38:46	0.0538	0.0112	-0.68	-3.07	
30	22:53:59.5	61:48:22	0.132	0.0340	-0.59	-2.79	
31	22:54:02.7	61:44:11	0.350	0.0897	-0.59	-2.79	
32	22:54:04.3	61:47:00	0.922	1.03	+0.05	-0.85	Central M.
33	22:54:04.7	61:52:54	0.0166				
34	22:54:05.8	61:44:35	0.0413	0.0489	+0.07	-0.78	
35	22:54:07.8	61:48:32	0.208	0.254	+0.09	-0.74	
36	22:54:10.2	61:44:40	0.0438				Binary
37	22:54:10.5	61:48:23	0.366	0.152	-0.38	-2.16	
38	22:54:10.5	61:50:21	0.0105				
39	22:54:13.0	61:43:37	0.105	0.169	+0.21	-0.37	
40	22:54:13.6	61:39:49	0.0193				
41	22:54:14.4	61:39:08	0.0176	0.0121	-0.16	-1.49	
42	22:54:14.6	61:46:18	0.736	0.389	-0.28	-1.84	Central M.
43	22:54:15.5	61:37:57	0.270	0.0505	-0.73	-3.21	
44	22:54:17.8	61:48:46	0.0212				
45	22:54:18.8	61:51:16	0.0137	0.0174	+0.10	-0.69	
46	22:54:18.9	61:45:53	5.71	23.5	+0.62	+0.87	Central M.
47	22:54:19.3	61:53:22	0.0937	0.0300	-0.49	-2.50	

Table 4-1. *Continued.*

ISO-Cep	RA (1950)	DEC (1950)	F(6.7) [Jy]	F(14.3) [Jy]	[14.3/6.7]	$\alpha_{6.7-14.3}$	Remarks
48	22:54:24.5	61:50:25	0.111	0.0219	-0.71	-3.14	
49	22:54:26.5	61:44:14	0.0166	0.0224	+0.13	-0.61	
50	22:54:26.2	61:41:47	0.0100	0.0252	+0.40	+0.22	
51	22:54:26.9	61:43:53	0.0078	0.0106	+0.13	-0.59	
52	22:54:27.5	61:54:19	0.0198				
53	22:54:29.3	61:43:47	0.0083				
54	22:54:29.4	61:51:34	0.0609	0.0281	-0.34	-2.02	
55	22:54:31.2	61:39:03	0.0236				
56	22:54:32.5	61:52:59	0.0306	0.0148	-0.32	-1.96	
57	22:54:34.7	61:48:47	0.303	0.0785	-0.59	-2.78	Binary
58	22:54:36.5	61:53:28	0.0326				
59	22:54:39.6	61:54:07	0.0639	0.0142	-0.65	-2.98	
60	22:54:40.6	61:45:01	0.0539	0.0842	+0.19	-0.41	
61	22:54:44.5	61:51:25	0.157	0.0756	-0.32	-1.96	
62	22:54:46.3	61:50:51	0.0381	0.0334	-0.06	-1.18	
63	22:54:48.8	61:54:36	0.0179	0.0082	-0.34	-2.02	
64	22:54:49.1	61:39:48	0.0324				
65	22:54:49.9	61:41:47	0.0293	0.0467	+0.20	-0.38	
66	22:54:52.2	61:48:23	0.0225				
67	22:54:53.9	61:41:56	0.0240	0.0486	+0.31	-0.07	
68	22:54:57.5	61:41:27	0.0387	0.0251	-0.19	-1.57	
69	22:55:08.2	61:46:07	0.0178				
70	22:55:22.7	61:48:10	0.0041				
71	22:55:25.4	61:49:44	0.0060				
72	22:55:26.2	61:46:59	0.0051				
73	22:55:31.2	61:48:56	0.0030				
74	22:55:32.5	61:46:55	0.0013	0.0072	+0.73	+1.21	
75	22:55:33.2	61:42:56	0.0123				
76	22:55:39.9	61:49:27	0.0093				

4.4 Colour diagrams

In order to detect sources with mid-IR excess (which indicates a YSO candidate, see chapter 1.1), using only ISOCAM data, we need both LW2 and LW3 photometry. Since all sources seen in LW3 were also detected in LW2, it is now possible to classify all 41 LW3 sources using a ‘colour diagram’.

A colour diagram is based on a spectral comparison of a source between two passbands, in this case the LW2 (6.7 μm) and LW3 (14.3 μm) passbands. All stars of course have intrinsic colours⁶, however, with a disk present (as is the case with YSOs) their intrinsic colours are reddened. By making a colour diagram using ISOCAM observations it is then possible to detect these highly reddened stars and classify them as YSO candidates.

⁶ The ‘colour’ of a star is usually its magnitude difference at two wavelength regions, for instance $m(\text{LW2})-m(\text{LW3})$. It is also common, when using ISOCAM photometry, to use the ISOCAM single colour index [14.3/6.7] as a colour.

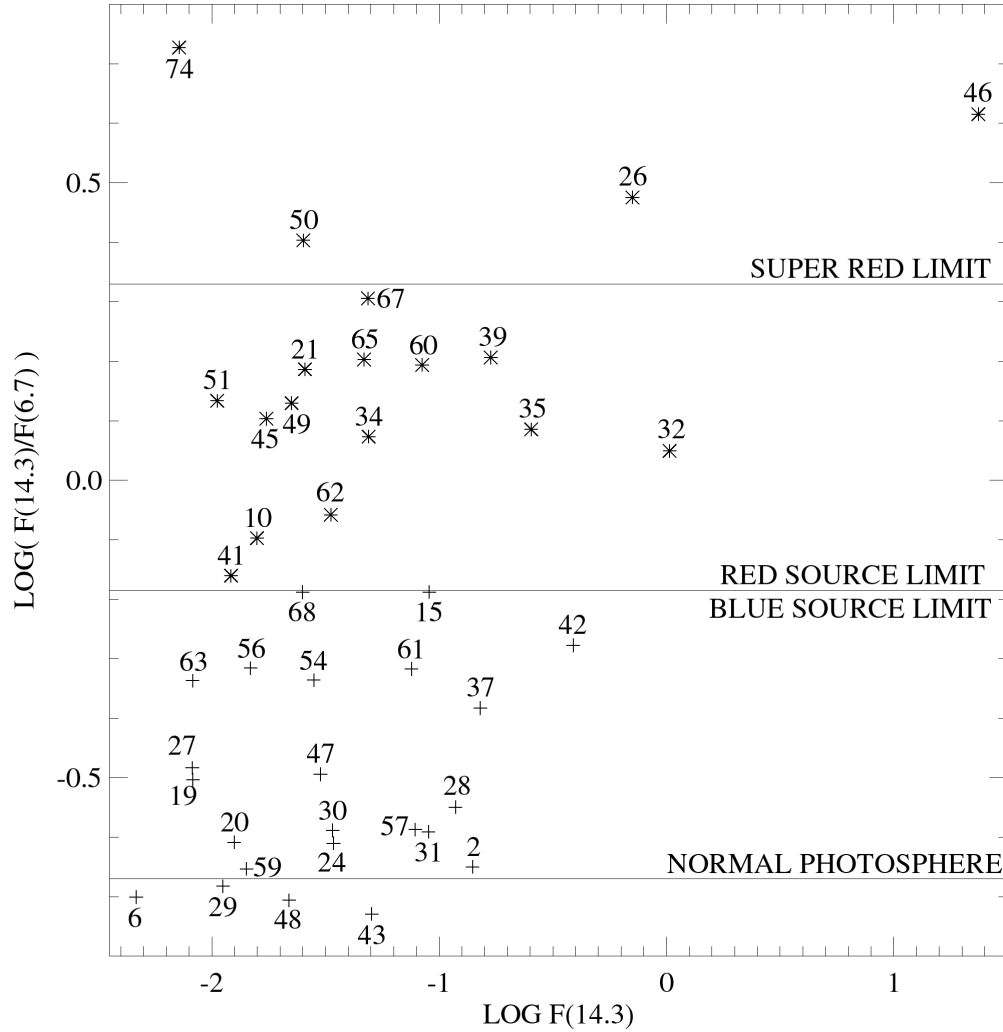


Figure 4-2. ISOCAM Single colour [14.3/6.7] type colour-diagram using all sources with LW2 and LW3 photometry available. ‘Blue’ sources are marked with plus signs while ‘red’ sources are marked with asterisks. At least 18 sources are clearly red.

In figure 4-2, all 41 ISO-sources with LW3 detections have been plotted and classified as ‘red’ or ‘blue’ based on their single colour index [14.3/6.7], defined as $\log(F(14.3)/F(6.7))$.

Out of the 41 ISO sources detected at 14.3 μm , 18 are classified as being ‘red’, i.e. showing evidence of a mid-IR excess. Several groups and sub-groups are clearly seen, first there are four class I candidates (‘super-red’). Below the ‘super red’ limit there are 11 stars (ISO-Cep-67 down to ISO-Cep-32) with large mid-IR excesses (at 14.3 μm) that are apparently ‘red’. Just above the ‘red/blue limit’ there are three sources: ISO-Cep-62, 10 and 41 that also show signs of having mid-IR excess.

In the ‘blue’ region, 8 stars (ISO-Cep-15 down to ISO-Cep-37) are located in a group just below the ‘red/blue limit’. Even though these stars have some mid-IR excess, the ISO-data alone are not convincing enough to classify them as ‘red’. However, with near-IR observations available for all these stars, they will be examined further for mid-IR excess in chapters 5.11 and 6.1.2.

The other stars in the 'blue' group are clearly 'blue', however, the centre of this sub-group is located somewhat to the 'red' of a 'normal photosphere' indicating that interstellar reddening may be important even at these wavelengths. This fact makes it even more important to examine the stars close to the 'red/blue limit' in the near-IR, where additional information can be gained on the reddening.

The two central sources ISO-Cep-32 and ISO-Cep-46 are extremely bright and are responsible for the large transients still remaining in the central mosaic.

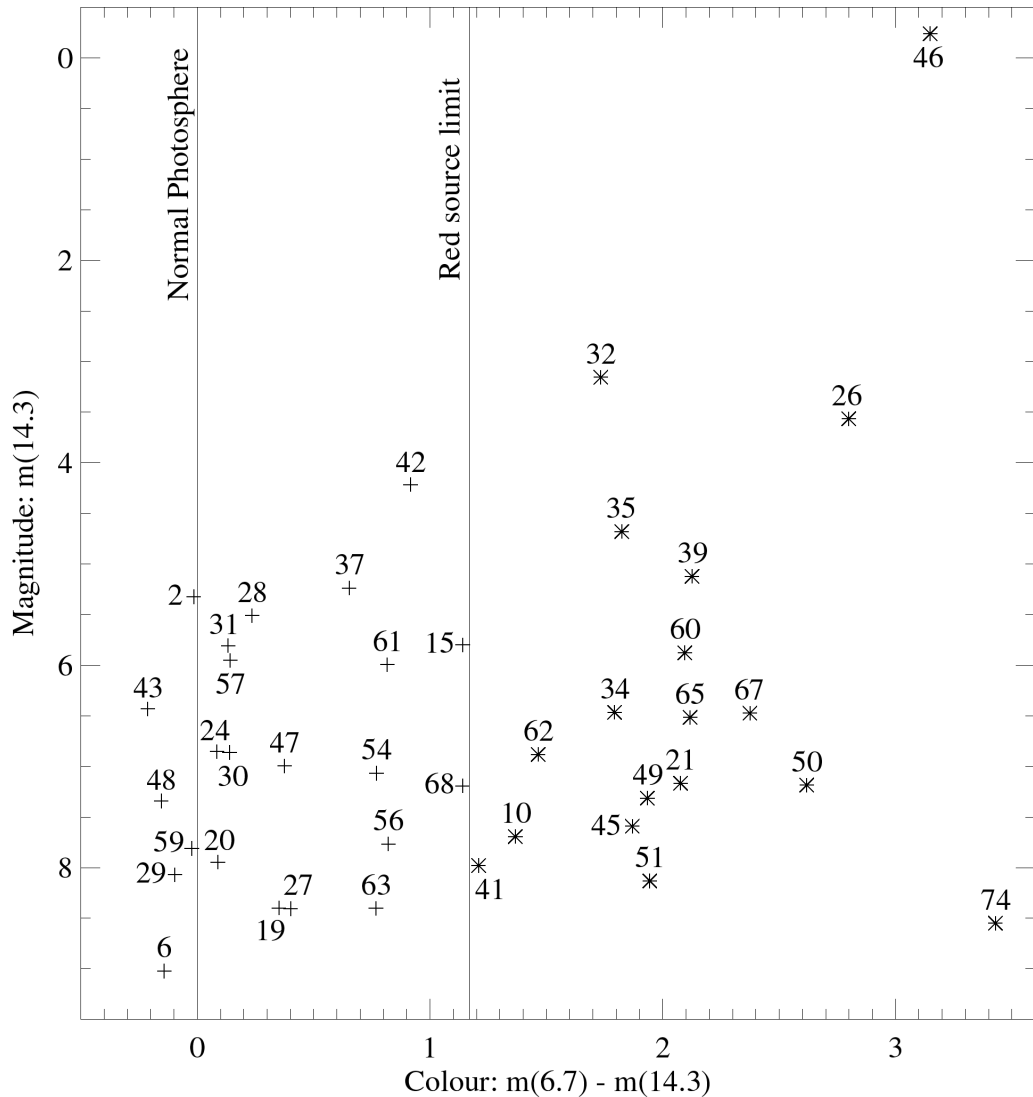


Figure 4-3. ISOCAM magnitude type colour-diagram.

Interstellar reddening in the $m(6.7)$ - $m(14.3)$ colour index could be somewhat responsible for reddening of the sources, however, from the colour/magnitude diagram in figure 4-3, it can be shown that there are background stars in heavily obscured regions⁷ with still normal colour indices (~ 0). This implies that intrinsic reddening is the dominating reddening factor at mid-IR wavelengths.

⁷ It can be seen in visual and near-IR colour / colour diagrams (chapters 5.11 and 6.1.2) that some of the ISO-blue sources are highly reddened along the interstellar reddening line, indicating that they are background stars.

5. My observations at visual and near-IR wavelengths

Since there has been very little done previously in terms of visual, near-IR and IR observations of Cepheus A¹, I set out to make both visual and near-IR observations myself, which I then could combine with ISOCAM's IR-observations later on.

5.1 Planning the observations

The telescope to be used for these observations is the 1m reflector telescope located at Stockholm Observatory², equipped with a 1024 x 1024 array CCD-camera mounted at the primary focus.

A filter wheel was also planned to be used, located in front of the CCD-camera, to simplify the changing of filters.

Due to Stockholms unstable and unpredictable weather (low pressures and humid air often move in from the Atlantic ocean), especially this close to the sea-level, I knew it was going to be a lot of waiting for the weather to become 'photometric', and even then, several observation nights before all required images were obtained at good, stable conditions.

There is also a strong glare to the N.W. due to light pollution from the nearby city of Stockholm. Fortunately, Cepheus high elevation³ (circumpolar, with a minimum elevation of $\sim 30^\circ$) made the observations of Cep A as good as possible regarding light pollution.

The FOV of the telescope/CCD camera combination is $\sim 8'$ while the ISO mosaics can be covered by an approximate $20' \times 20'$ square mosaic (see figure 3-1). This of course requires a 3×3 images mosaic for each filter, assuming a $1'$ overlap. This, in turn, requires pretty accurate positioning of the telescope in order to obtain several mosaics of the same area, using different filters, since the telescope has to be lowered to an elevation of $\sim 20^\circ$ after each mosaic to rotate the filter wheel and then reposition all 9 previous positions to obtain images for the next mosaic.

At first, a positioning system using special software and hardware connected to the telescope's motor were going to be used, yielding an approximate accuracy of 0.5s ($7.5''$ at 0° Dec.) in Right Ascension and 0.15' ($9''$) in Declination. After a calibration with a bright star this would be of sufficient accuracy, however, after a few test-nights the hardware proved to be unreliable, sometimes not functioning at all, so another method had to be found.

Actually, two methods were combined in order to point the telescope at the desired image coordinates. An analogue camera/image intensifier, connected to a monitor was now placed behind the telescope's viewfinder, yielding a square FOV of about 1° . Now, the first

¹ Most Cep A observations has previously been in the radio regime, or poor-resolution observations in the far-IR.

² Stockholm Observatory is located at 60m above sea-level, at Saltsjöbaden: $18^\circ 18.5' E$; $59^\circ 16.3' N$

³ The high elevation of Cep A also induced a problem, since the telescope had to be turned 180° in RA when Cep A passed overhead!

(approximate) method is the ‘setting-circles’ technique in which a bright star with known coordinates is placed at the monitors centre, I often used the star κ Cassiopeia as a calibration star due to its roughly similar declination to the Cep A area whilst being a rather bright star (mag.4.2).

The RA-circle was now set to the target star’s known RA-coordinate (this is equivalent to setting the sidereal time) while the Dec circle of course never needs to be set. In the case of Cep A, the telescope is now pointed at the 8.5 mag. star SAO 20299, about 3 minutes to the west of Cep A. Fine-adjustments are now made so that this ‘start star’ is located as close as possible to the monitor’s centre.

As for the second method, it uses Earth’s rotation and timing to position the telescope at the 9 positions that make up the mosaic, as is shown in figure 5-1.

With the telescope pointing at SAO 20299, the RA-motor is turned off for as long as the time-arrows indicate, then it is turned on again and the RA position of a selected image is set. The declination is set by slewing the telescope with the Dec motor until it has moved 7’ (images 4-6) or 14’ (images 7-9) south of the start star. These distances have actually been measured previously on the monitor when images 1-3 were positioned, since 1m in RA roughly corresponds to 7’ in Dec. at the declination of Cep A.

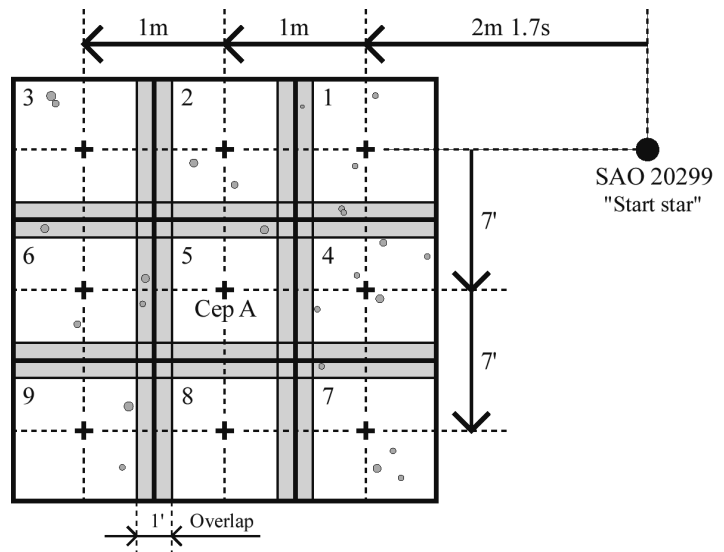


Figure 5-1. Each mosaic consist of 9 images with a 1’ overlap. The ‘start star’ SAO 20299 is used as a reference when pointing the telescope, using Earths rotation and timing.

All stars in the GSC for the mosaic region are shown in figure 5-1, the faintest one being of magnitude $m_V \approx 14.4$.

Before and after each image position, a corresponding dark image is taken, these are essentially CCD-images with the shutter closed, using the same exposure times as the ‘real’ images. One extra dark image is obtained before images 4 and 7 since the time-delays between images 3-4 and 6-7 due to repositioning (using the ‘start star’) are long enough for the dark current to change noticeably.

While I wanted as long exposures as possible in order to obtain good photometry data and get high limiting magnitudes, there is also the timefactor to consider and in order to make a whole mosaic with similar sky conditions for all images it is necessary to obtain all images for a chosen filter in one night, with the photometric conditions not having time to change too much. A reasonable compromise seemed to be 300 seconds, however, test nights has shown that the dark current limits the exposure time to 100 seconds which implies that 3 exposures

must be used for each image. The dark current is stable enough that dark exposures are not needed between exposures of the same image.

The effective observing time needed for the whole mosaic in one filter is therefore $(9 \cdot 3 + 12) \cdot 100$ seconds = 65 minutes, using 12 dark images. In reality, the total observing time is much longer since there are a lot of preparations before each image, for instance rotating the dome to a safe position, waiting with the RA-motor off (timing), moving the telescope in declination and sometimes repositioning the start star (for each row in the mosaic). Also, it is sometimes needed to change the focus and retake the latest (unfocused) exposure.

Also, the darkest hours of the night were used, with the observations centred around the time when Cep A passes nearly overhead, to make sure that Cep A has a high elevation that does not change too much during the observations.

5.2 Filter testing

Since the purpose of my observations are photometric measurements at different (shorter) wavelength regions than the mid-IR observations of ISOCAM, in order to obtain good spectral coverage, it is necessary to have a good knowledge of which wavelength regions are observed and the corresponding transmission curve for each filter.

A cut-on or cut-off filter by itself is rather useless for this purpose since these filters have very wide transmission curves, limited only to wavelengths either shorter or longer than a certain limit. What we really need is either a true bandpass filter or a combination filter using a cut-on/cut-off combination, resulting in a unique⁴ passband.

Four filters were measured in the 0.4 to 1.2 μm range, resulting in the transmission curves seen in figure 5-2.

There are a red cut-on filter, a blue-green cut-off filter (named 301 A) apparently with a "leak" at wavelengths longer than $\sim 0.9 \mu\text{m}$, a true V passband filter ($0.55 \mu\text{m}$) and a $1.05 \mu\text{m}$ passband filter that lies somewhere between the standard I and J passbands⁵. The cut-on/cut-off filters could in this case be combined to give a passband filter much like the V-filter, however with reduced transmission and

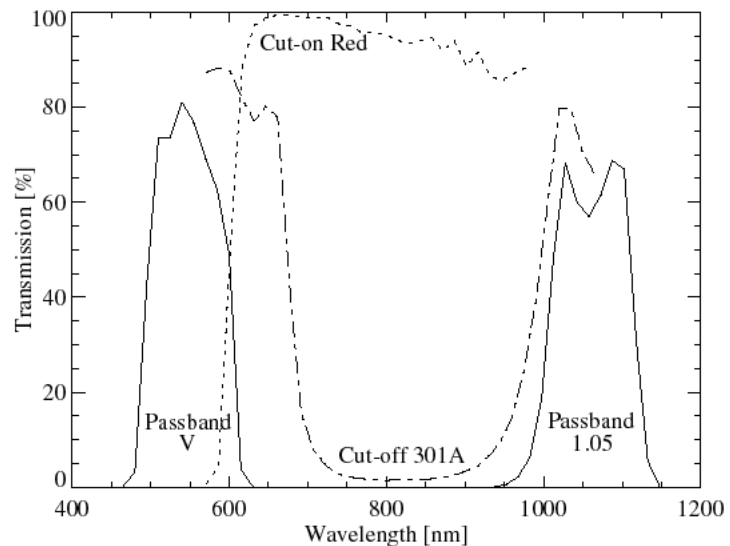


Figure 5-2. Transmission curves of lab-tested filters.

⁴ Single passband filters often have standard transmission curves, while a cut-on/cut-off combination can result in a more unusual passband.

⁵ For more information on standard passbands, see Mayers et al (1987).

a slightly higher effective wavelength. Since this filter would be similar to a V-filter only with a weaker signal, **the V and 1.05 μm filters are chosen**, resulting in two different passband mosaics of the Cep A region.

The 1.05 μm filter lies in the near-IR at wavelengths where the CCD-camera has reduced sensitivity while the V filter of course lies at optical wavelengths, resulting in high CCD-camera sensitivity and therefore a higher limiting magnitude.

5.3 Preparations

Now that two filters have been chosen, an easy way of interchanging these is required, and this will be done by the means of a filter wheel. The filter wheel was constructed as in figure 5-3. It consists of a wheel with six available circular holes, four of these were covered up with black plastic 'circles' in order to prevent confusion regarding which filter is active. The remaining two holes, located on opposite sides of the wheel, are now used for the V and 1.05 μm filters. Two metal balls are located under the wheel, against a metal wheel with a circular "track" and two depressions, resulting in two "stop-positions" at which one of the filters is lined up with the exit hole and the CCD-camera. In order to be sure of which filter is active, markings has been made at the opposite sides of the filter-wheel for each filter, easily readable.

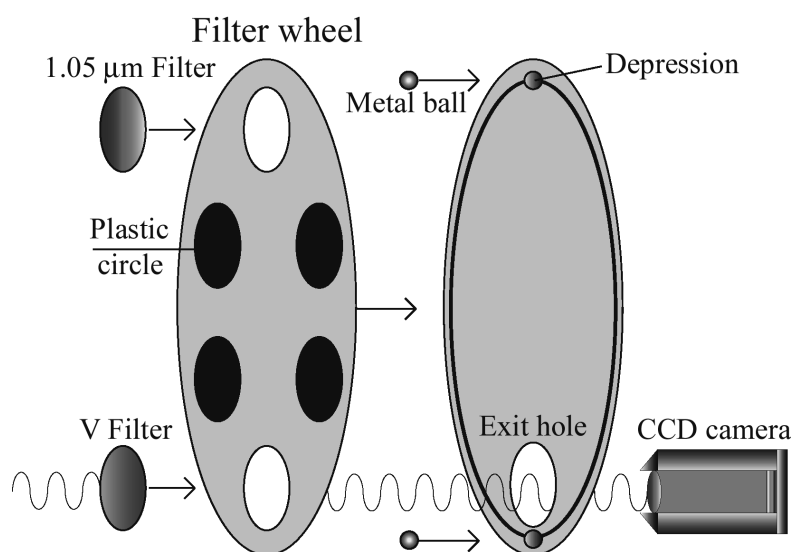


Figure 5-3. Filter wheel constructed to easily interchange filters.

As a part of the telescope preparations, the 1m diameter primary mirror of the reflector telescope was re-aluminized, resulting in a more efficient reflecting surface and more light being focused at the CCD-camera. The primary was also aligned by making sure that it was not tilted in respect to the mechanical axis of the telescope. This had probably not been done since the 1960's.

The CCD-camera was placed close to the prime focus and connected to the observation computer and focusing equipment. It was then tested that the camera had enough moving capabilities to be brought into focus during one of the test nights. Before the camera was placed at the telescope it was pumped and filled with dry nitrogen to avoid condensation of water on the CCD chip. Also, the telescope's RA-motor was fine-tuned and the observation computer was replaced as a result of several test nights, proving the RA-motor to be unreliable as well as the computer, after a harddisk crash!

5.4 The CCD camera

The CCD camera has a resolution of 1024 x 1024 pixels, resulting in a square FOV greater than $\sim 8 \times 8$ arcminutes. This yields a PFOV of ~ 0.5 arcseconds, although this resolution has never been achieved on any test-night due to atmospheric conditions.

Due to the CCD camera's mounting, some rows and columns at the edges of the CCD-chip are covered resulting in smaller images (1000 x 1017 pixels), columns 1-24 as well as rows 1 and 1019-1024 are therefore unusable.

It has a cooling system to minimize the dark current, however, exposure times greater than five minutes (and sometimes just a few minutes) yields a dark current with ADU's as large as 65535 which is the absolute maximum of the images. Therefore, leaving some margins to dark-current saturation, exposure times of 100s has been chosen and an image consists of 3x100s exposures resulting in a total exposure of 300s (while keeping down the dark current) since an image is calculated as a mean of the exposures, keeping ADU-values well below 65535 in each exposure.

The shortest possible exposure time seems to be ~ 0.05 s, however at these short exposures the bias totally dominates over the dark current as the largest noise component.

5.5 Telescope testing

A number of tests were conducted, establishing a magnitude limit of at least 17 mag. for the V filter and 13 mag. for the 1.05 μm filter. These tests involved data reduction of 5 minute exposures using bias, dark and flat-fields. Then, estimating the weakest star visible, comparing with weak stars in the GSC. As for the limit of the 1.05 μm filter, it is a rough estimation based on observed A0 stars, with known magnitudes.

In order to orientate oneself in the apparent star-field displayed in the monitor viewfinder, after a rough positioning, weak enough stars must be seen in the monitor. By observing the Cep A region, the limiting magnitude of the monitor/viewfinder system was estimated to at least 12 mag. at which stars were easily seen. This is certainly enough to locate the "start star" of magnitude 8.5 and to track the movement of the star field when the RA motor is turned off.

As a check for a possible 'viewfinder camera' tilt relative to the equatorial coordinate system, the RA motor was turned off after placing a bright star at the monitor's right edge (largest RA coordinate), rotating the viewfinder camera until the star moved horizontally across the screen.

Also, the CCD camera's tilt was calibrated using star-trails resulting from long exposures of a bright star with the RA-motor turned off.

The focus of the CCD camera is set by moving the camera closer/further from the primary mirror using a switch and a display in the control room. Since the focus varied slightly throughout a typical test night, it was checked that the camera could be moved enough to obtain the two most extreme focuses realistically needed on a real observation night.

Aligning the viewfinder and its camera to the telescope's optical axis is also important in order to make reliable observations, knowing that a star in the viewfinder's centre will also be located at the viewfinder-monitor's centre and to a high degree also at the CCD camera's centre in an exposure.

Several test images were taken around Cep A, they did not show that much nebulosity except for some small regions (a few arcseconds in radius) close to some bright stars. This implies that a flatfield can be made directly out of the images in the mosaic using the so called 'median method' on dark corrected images. Details of the reduction methods will be found in chapter 5.7.

The Earth rotation and timing method described in the planning of the observations (chapter 5.1) was thoroughly tested and seemed to work excellent.

5.6 Observations

During the spring of 1998 most of the test observations were made as part of the planning, several important considerations were then taken into account, for instance at first only four images seemed to be required for the mosaic (2x2), but during these observations it became evident that at least a 3x3 mosaic (9 images) really was needed for each filter to yield sufficient overlaps and spatial coverage.

Serious observations begun at the end of April, however, after a week of observations in non-photometric conditions the nights became too short to make a whole mosaic in one night, which is preferable since this makes the photometry more reliable when comparing measurements between different images in the mosaic. At May 1st the astronomical night⁶ was only 3 hours and 50 minutes and further observing had to be continued after the bright summer months⁷.

Observations were resumed at the end of September, with some improvements made to the observatory's equipment during the summer, for instance the RA-motor of the 1m telescope was adjusted and became much more reliable than before. A week followed with two observation occasions that started out fine, but clouds started to form in the middle of the mosaic observations (at one time when the seventh mosaic image out of nine was being observed!).

⁶ The astronomical night is defined as the time-period during which the Sun remains more than 12° below the horizon.

⁷ Actually, at the night after summer solstice (June 21/22) the Sun is never lower than about $-7^\circ 17'$ relative the horizon. It rises at 3:30 and sets at 22:06 local summer time, this shows why any serious observations are impossible during the summer months here at Stockholm Observatory.

Finally, during the first two weeks of October, two very successful nights with photometric conditions provided the two needed mosaics (one night was required for each filter).

Table 5-1. *Observational log of the optical observations.*

V filter Observations				
<i>Date:</i>	<i>1998 – October – 13/14</i>			
<i>Exposure time:</i>	<i>3 x 100 s</i>			
<i>Orientation:</i>	<i>South</i>			
<i>Epoch</i>	<i>1950</i>			
<i>Seeing:</i>	<i>Very good</i>			
<i>Comments:</i>	<i>The focus was constantly changing</i>			
Position	RA ⁸	DEC ⁸	Focus ⁹	Comments
1	22 ^h 53 ^m 24.9 ^s	61°52'22"	45	<i>One of the two dark fields was unusable</i>
2	22:54:24.7	61:52:20	45	
3	22:55:24.1	61:52:19	45	<i>A bright star flooded some pixels on the CCD</i>
4	22:53:25.2	61:46:00	45	
5	22:54:25.2	61:46:01	45	
6	22:55:25.5	61:46:01	60	<i>Change of focus</i>
7	22:53:27.1	61:39:24	60	
8	22:54:26.3	61:39:25	60	
9	22:55:26.1	61:39:26	76	<i>Change of focus</i>

Since each position needed three exposures the telescope had to point in the same direction for at least 5 minutes. For this the RA motor needs to be in good shape, which was proven by the observations since the largest RA drift for any position in the mosaic was 3 pixels which corresponds to ~1.5 arcsec.

As can be seen in the table, the RA overlaps are very small since the subsequent RA coordinates are very close to 1 min as planned, but the Dec overlaps are somewhat larger than the planned 1' which has been done on purpose since the accuracy of the telescope pointing is less in declination, the Earth rotation/timing method can of course only be used in RA. When positioning the telescope, the RA accuracy obtained using this timing method is at least 0.5s (~3.5") while the declination accuracy is estimated to be about 20". The obtained accuracy, as calculated afterwards using guide stars in the mosaic with the images positioned correctly is of course much higher (see chapter 5.8 for details).

The focus increased steadily during the night, however, this does not have any effect on the observation data since any detectably unfocused image resulted in a refocus and a retake of the exposures for that position.

As for the second mosaic, it is that of the 1.05 μm passband-filter images which were

⁸ *These coordinates are valid for the centre of each image and has been calculated from the guide-star calibration as described in chapter 5.8*

⁹ *The figures used to describe the focus are really a measurement of the CCD camera's position relative to the primary mirror along the optical axis, expressed in convenient units and origin.*

obtained much in the same way as the V-images. The observational log for these observations are shown in the table below.

Table 5-2. *Observational log of the near infrared observations.*

1.05 μm filter Observations				
<i>Date:</i>	<i>1998 – October – 3/4</i>			
<i>Exposure time:</i>	<i>3 x 100 s</i>			
<i>Orientation:</i>	<i>North</i>			
<i>Epoch</i>	<i>1950</i>			
<i>Seeing:</i>	<i>Good</i>			
<i>Comments:</i>	<i>Some fog started to form at sea-level during the observations, however at 60m the seeing remained good until about 1 hour after the observations had finished. Then the fog reached all the way up to the observatory and the seeing changed drastically to the worse!</i>			
Position	RA ⁸	DEC ⁸	Focus ⁹	Comments
1	22 ^h 53 ^m 20.6 ^s	61°52'25"	71	<i>The focus appear to be stable</i>
2	22:54:19.0	61:52:24	71	
3	22:55:18.8	61:52:25	71	
4	22:53:22.9	61:46:15	71	
5	22:54:22.8	61:46:14	71	
6	22:55:22.4	61:46:13	71	
7	22:53:24.5	61:40:25	71	
8	22:54:24.7	61:40:24	71	
9	22:55:24.7	61:40:24	71	<i>Only two exposures could be obtained</i>
SAO 20394	23:03:20.1	62:38:00	71	<i>Spectral type A0 (Used for photometric calibration) Coordinates are in Epoch 2000</i>

The RA motor showed a similar accuracy as for the V filter observations.

In order to be able to make a mosaic out of these 1.05 μm images, larger overlaps had to be used in declination since fewer stars will be seen in these images than in the V images depending both on a degraded transmission curve and the decreased CCD camera sensitivity at these wavelengths. In RA the overlaps remains about the same since the timing method of course yields the same precision as for the V filter.

Since the orientation of these images are to the north, they did not need to be mirrored as was the case for the V filter images¹.

An A0 star was also observed to be used later when calibrating the 1.05 μm photometry. This is done since an A0 star by definition should have about the same magnitude in all bands (if interstellar reddening can be neglected, or corrected for). The A0V star 'SAO 20394' has been chosen since it is located close to Cep A. For both filters, dark images were obtained as planned in chapter 5.1.

¹ *The reason for this is that the V observations had to be made with the telescope turned 180° in RA to avoid hitting the mounting with the telescope.*

5.7 Data reduction

No bias fields needed to be taken since these are always included in the large amount of dark fields used in the data reduction. Except for position 1 in the V filter mosaic two dark fields are available for each position, one before and one after the three exposures of each position. For each exposure the unusable pixels (chapter 5.4) are removed, resulting in 1000 x 1017 pixel exposures, this is also done to the corresponding dark exposures.

The RA drift is as mentioned before quite small, however a drift of 0-3 pixels during each position is evident when comparing the three images of a certain mosaic position. This effect is now corrected for by repositioning the images "on top" of each other, resulting in three images of the same sky area but losing a few pixel rows/columns at the edges where all three images do not overlap. Then, the mean value of each pixel is calculated from the three images, resulting in a 300s exposure at each mosaic position.

For each position, the two dark fields are now averaged to obtain a dark field valid for all three exposures of that position. Now the calculated 300s exposure images are dark corrected by subtracting the corresponding calculated dark fields. This yields a total of 18 dark corrected images, one for each position in the two mosaics.

Since the nebulosity has been proven neglectible using both filters in the test observations, a flatfield can be calculated for each filter, directly from the 9 images contained in each mosaic. This is done by using the so called 'median method' in which the median of each pixel in all dark corrected images of a filter is calculated. The obtained flatfields (one for each filter) are now images of what the sky would look like if it were 'flat', with no stars or other sources available in the exposure, showing only the systematic errors of the CCD camera which for instance includes the different sensibilities of the pixels on the CCD chip. By subtracting each filters corresponding flatfield from the mosaic images, flatfield corrected images are obtained.

These bias, dark and flatfield corrected images are then finally combined to give two mosaics of the observed region.

5.8 The mosaics of Cepheus A in Visual and Near-IR observations

By visually identifying the same stars, present in several image positions used for a mosaic, due to the overlaps between neighbouring images it is now possible to build a mosaic for each filter. The final mosaics are presented in appendix D with all detectable ISOCAM sources circled. The two mosaics were put together using a small program that I have written for this purpose, and after a coordinate system relation has been established between the equatorial (RA, Dec) coordinates and the mosaic (x, y pixel) coordinates, it is possible to calculate the centre position of each image contained in the mosaics (tables 5-1 and 5-2). Assuming a linear relation in two dimensions between these systems, we get:

$$\text{RA} = A + B \cdot x + C \cdot y \quad (\text{Eq. 1})$$

$$\text{Dec} = D + E \cdot x + F \cdot y \quad (\text{Eq. 2})$$

Not only is this assumption well motivated by the fact that the CCD camera (and therefore the mosaic) is slightly tilted to the equatorial coordinate system, there is also a linear effect in play here from the RA grid's narrowing with increased declination². Since the variations across the mosaic in declination are less than 20' this is also well approximated by the linear relations.

For the calculations leading to the constants A-F stated in equations (1) and (2), 25 HST GSC stars were used for the V mosaic and 24 for the 1.05 μm mosaic. Using multiple regression (least squares fitting) this leads to the following normal-equations:

$$\begin{aligned} A \cdot N + B \cdot \sum x_i + C \cdot \sum y_i &= \sum RA_i \\ A \cdot \sum x_i + B \cdot \sum x_i^2 + C \cdot \sum x_i \cdot y_i &= \sum x_i \cdot RA_i \\ A \cdot \sum y_i + B \cdot \sum x_i \cdot y_i + C \cdot \sum y_i^2 &= \sum y_i \cdot RA_i \\ \\ D \cdot N + E \cdot \sum x_i + F \cdot \sum y_i &= \sum Dec_i \\ D \cdot \sum x_i + E \cdot \sum x_i^2 + F \cdot \sum x_i \cdot y_i &= \sum x_i \cdot Dec_i \\ D \cdot \sum y_i + E \cdot \sum x_i \cdot y_i + F \cdot \sum y_i^2 &= \sum y_i \cdot Dec_i \end{aligned}$$

Solving these equations with N=25 using the V mosaic data now gives a set of constants A_V, B_V, \dots, F_V while solving them with N=24 for the 1.05 μm mosaic data gives another set of constants $A_{1.05}, B_{1.05}, \dots, F_{1.05}$. The errors in RA and Dec when calculated with equations (1) and (2) have been estimated to $\sigma_{RA} \sim 0.4s$ ($\approx 3''$) and $\sigma_{Dec} \sim 3''$ for both the V mosaic and the 1.05 μm mosaic.

We also have a useful inverse relation to equations (1) and (2):

$$x = \frac{Dec - D + \frac{F}{C} \cdot (A - RA)}{E - \frac{F}{C} \cdot B} \quad (\text{Eq. 3})$$

$$y = \frac{RA - A - B \cdot x}{C} \quad (\text{Eq. 4})$$

Equations (3) and (4) can now efficiently be used to calculate the ISOCAM sources approximate pixel (x,y) coordinates in the V and 1.05 μm mosaics.

5.9 Identification of ISOCAM sources

Equations (3) and (4) were used with the ISOCAM coordinates listed in table 4-1. to give the corresponding pixel coordinates in the two mosaics. I have made a program for this purpose, that displays the V filter and 1.05 μm filter mosaics with the calculated position circled. If a source could be seen within a $\sim 5''$ radius circle around the calculated position,

² At a declination of 0° , 1h in RA corresponds to exactly 15° however at greater declinations (closer to one of the poles) this decreases due to the smaller RA circles that makes up 24h and therefore the RA grid gets more narrow. The RA coordinate varies with declination (Dec) according to the factor $\cos(\text{Dec})$.

small adjustments were made to the position to centre this source. For each adjustment a PSF is drawn and used to find the flux centre of the source. This procedure was carried out on both mosaics for all ISO sources, yielding pixel coordinates of sources detectable at these wavelengths.

Out of the 76 ISO sources, 26 were seen in the V passband and 35 in the 1.05 μm passband mosaic. There are 23 sources that are present in both mosaics.

5.10 Photometry

Both the photometry of the V and 1.05 μm passband observations were carried out using a photometry program I wrote, this program is described in section 5.10.1 below. It needs two precalculated input variables, an integrated PSF variable and an uncertainty matrix, these are described in sections 5.10.2 and 5.10.3 respectively.

5.10.1 The photometry program

Photometry of the identified ISO sources in the V and 1.05 μm mosaics was done with a computer program that I wrote especially for this purpose, in the IDL³ language. The program is listed in appendix B and the details of the used methods are described in this chapter.

When a source's coordinates in a mosaic is known, either by direct measuring in the mosaic or by calculating it from its equatorial coordinates using calibration stars in the mosaic, the program divides the surrounding area into three types of regions (figure 5-4).

The program uses a photometry method called 'Aperature photometry'. The 'aperature' is the region inside an aperature circle, defining an outer edge of the source, out to which it is easily measurable. Between the aperature and sky circles lies the so called sky area which is used to calculate the flux correction at the source due to the background sky. Outside the sky circle but inside the photometry limit of the data readout lies a void region not considered in further calculations.

The program first obtains input information (both source and project specific data) entered in the beginning of the source code by the user. The user-specific parameters are only entered once for each mosaic and are valid for all measurements within the mosaic. However, before each run of the program

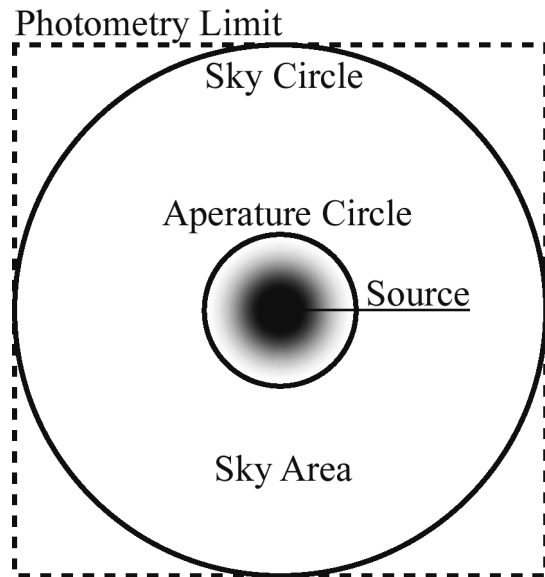


Figure 5-4. The regions used for 'aperature photometry' by the photometry program.

³ IDL is a mathematical, programmable software package developed by Research Systems, Inc. in which images can be used as variables in all types of calculations, enabling efficient data reduction and measurements.

the user is able to change the source specific parameters in order to try out new settings for the aperture and sky radii, and to make fine-adjustments of the source's position.

Among the user specific parameters are some rather self explanatory parameters controlling the window size, the aperture rebin size, the name of the mosaic and its 'cuts' used for the display. There are however two parameters that deserves a closer explanation (PSF and sigma). The PSF parameter is an integrated PSF along the aperture radius, containing ratios of the considered/total flux for each radius out to a maximum-radius (obtained by measuring the aperture radius for the strongest sources). The sigma parameter is an uncertainty estimation variable based on the used sky size and aperture radii. Both the PSF and sigma parameters are pre-calculated, this is described in sections 5.10.2 and 5.10.3.

Then, some automatic parameters are calculated by the program and the mosaic is shown with the current aperture and sky-circles. Since the mosaic in this case is larger than the drawing window, only a part of the mosaic, preferably with the source at the windows centre (not possible when close to a mosaic edge) can be shown.

The equatorial coordinates of the source's centre pixel is then calculated, using equations (1) and (2) in chapter 5.8. Now it is time for the sky and aperture data to be read, this is done by dividing all pixels within the photometry limit into the three regions shown in figure 5-4.

A statistical analysis is carried out on the sky pixels yielding its mean, median value and standard deviation σ . Since closeby sources and exceedingly bright or dark pixels may contaminate the sky sample a ' 3σ clipping' method is used to filter out sky pixels deviating more than 3σ from the median value of the sky (not the mean value since this is more easily affected by other sources present in the sky region which increases the sky's mean much more than its median value).

Then the aperture calculations follows, correcting the aperture for background (sky) flux by subtracting the mean sky value from all pixels in the aperture and also calculating an integrated PSF radially for the current source. This PSF is NOT the one used later in the program to calculate the total source flux, it is only used in one of the help-plots⁴ to simplify the choice of an aperture and sky radius.

Now the integrated part of the source is estimated from the general integrated PSF, this is then used to calculate the total flux of the source (in ADUs). Finally, the 'help-plots' are plotted and information is printed on the screen regarding both the source coordinates and its photometry. If the user is not satisfied with the source specific parameters, as is seen in the mosaic and using the help-plots, the parameters are changed and the program run again.

For both the V and 1.05 μm photometry, I chose aperture radii that incorporated between 50% (weak sources) and 100% (very strong sources) of the total source flux. By dividing the

⁴ Four so called 'help-plots' are plotted by the program to further help the user choose aperture and sky radii. These plots are: A radially integrated PSF, two 1-dim. PSF's (horizontally and vertically) through the source's centre and finally a signal-strength plot.

measured flux with the corresponding integrated PSF value the total flux is of course obtained. I used the signal strength help-plot to choose a suiting aperature radius, always keeping the signal above 1σ (preferably above 3σ) everywhere inside this radius.

As for the sky radius, three sizes were used as following:

Small sky	25 pixels	Bright stars very close to measured source
Medium sky	50 pixels	Intermediate
Large sky	100 pixels	Isolated source, no localized nebulosity or nearby sources

In the V-mosaic case, the V magnitude for any source is now calculated⁵ as:

$$m_v = m_i - 2.5 \cdot \log (F_v / F_i)$$

where m_i and F_i are the known V magnitude and flux of a 'calibration star'. This expression can now be rewritten as:

$$2.5 \cdot \log (F_v / F_i) = m_i - m_v \Leftrightarrow 2.5 \cdot \log (F_v) = c_1 + c_2 \cdot m_v \Rightarrow$$

$$m_v = (2.5 \cdot \log F_v - c_1) / c_2 \quad (\text{Eq. 5})$$

By using 17 GSC stars present in the V mosaic (measuring their ADU fluxes F_i) as calibration stars, having V magnitudes ranging from 10.7 down to 14.4, the two constants c_1 and c_2 in equation (5) were obtained by a linear fit (figure 5-5):

$$c_1 \approx 27.168$$

$$c_2 \approx -0.999$$

A statistical analysis using the guide stars and the fitted line now yields the V magnitude uncertainty:

$$\sigma_v = 0.16 \text{ mag.}$$

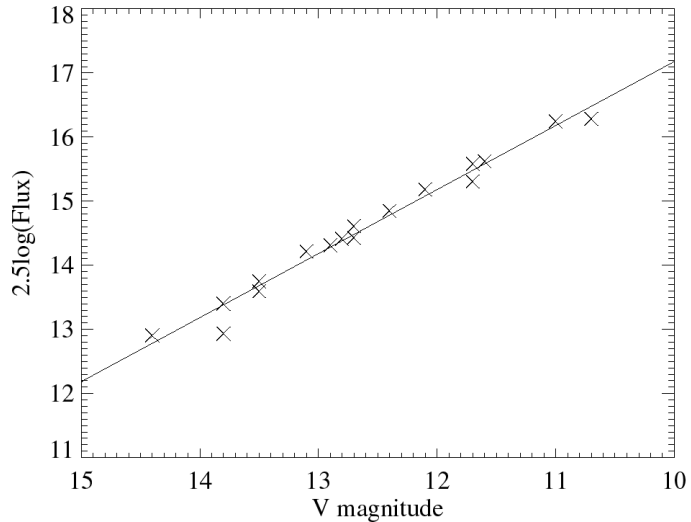


Figure 5-5. Calibration of the magnitude-flux relation for the V-filter using 17 GSC stars.

For the photometry in the $1.05 \mu\text{m}$ mosaic a calibration star of spectral type A0V (SAO 20394) was used. According to the Hipparchos catalogue: $m_v = 8.167 \pm 0.01$, $B-V \approx 0.04$ and $V-I \approx 0.06$. An interpolation for the interstellar extinction (Martin & Whittet. 1990) yields $E_{1.05-V} / E_{B-V} \approx -1.96$. This implies that $m_{\text{SAO20394}, 1.05\mu\text{m}} = 8.09 \pm 0.05 \text{ mag.}$ and for any star in the mosaic we now get:

$$m_{1.05} = m_{\text{SAO20394}, 1.05\mu\text{m}} - 2.5 \cdot \log [F_{1.05} / F_{\text{SAO20394}, 1.05\mu\text{m}}] \quad (\text{Eq. 6})$$

where it is reasonable to assume that $\sigma_{1.05} = 0.16 \text{ mag.}$ as in the V magnitude case.

⁵ The first step of the calculation is just the logarithm of the magnitude definition: $F_2 / F_1 = 100^{(m_1 - m_2)/5}$

5.10.2 Calculating the integrated PSF

It is assumed that any point source, independent of its flux, yields the same size in a mosaic even though weak sources has much smaller aperature radii in the photometry measurements due to their much lower signal to noise ratios and thereby smaller apparent sizes. Therefore only a part of a weak source's flux can be integrated directly, but if one knows the ratio of measured/total flux (for instance 50%) its total flux can easily be calculated.

This is done by calculating an integrated, normalized PSF that expresses the measured/total flux for each possible aperature radii. Based on the equal size assumption above, a PSF that is calculated from some of the strongest point-sources is valid for all sources in the mosaic independent of their fluxes.

The largest (apparent) point-sources in the V mosaic has aperature radii of ~15 pixels, compared to ~13 pixels for the 1.05 μm mosaic. An integrated PSF is then calculated for each mosaic, using as many of the bright point sources as possible. In the V mosaic, 13 strong point-sources (each with an aperature radius of 15 pixels) are used to calculate the PSF, while in the 1.05 μm mosaic 10 strong point sources are used (aperature radii of 13 pixels). For both mosaics, two different PSF's had to be used, one for images 2-3 and one for all other images.

A number of 'selection requirements' were used to select stars for the PSF calculations:

1. Bright stars, with apparent radii of ~15 pixels (V mosaic) or ~13 pixels (1.05 μm mosaic)
2. Not a double star as seen in the Palomar Sky Survey (PSS) optical images
3. Not too close to a mosaic's edge, to get a large enough sky area for aperature photometry

For each chosen star, its integrated PSF is calculated using the photometry program (see section 5.10.1) and stored as a variable until all needed PSF's have been calculated. The resulting PSF's are then used to calculate a mean PSF curve, which is then valid for all stars in the used images.

As an example of an integrated PSF used in the calculations, in figure 5-6 the integrated PSF for images 1 and 4-9 in the V filter mosaic is plotted.

The integrated PSFs are very similar for the different images of each mosaic, however, there is an apparent difference between the integrated PSFs of the two mosaics, mostly because the seeing varied for the two observation nights (one filter each night).

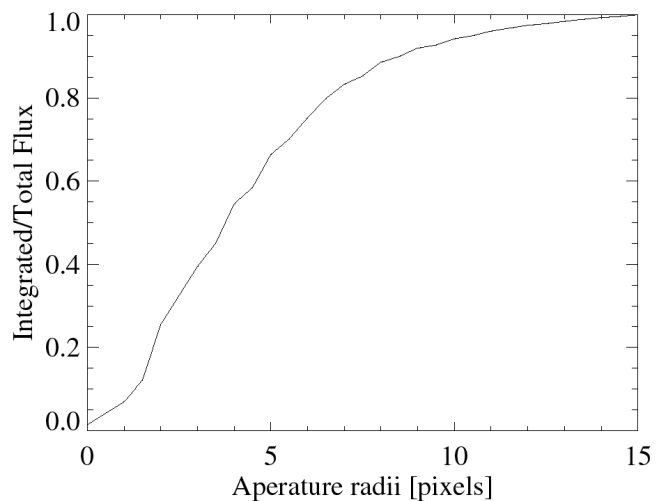


Figure 5-6. Integrated PSF for the optical mosaic.

5.10.3 Uncertainty estimations

The flux uncertainties depend on several factors, among these are the chosen aperture and sky radii. In order to estimate the uncertainties, 20 apparently "empty" positions in each mosaic without any nearby point sources were measured with the photometry program using all possible aperture and sky radii. For every combination⁶ the flux (in ADUs) was measured, theoretically this flux should be approximately zero.

All these measurements (automatically done for each 'fake' source using a modified version of the photometry program) were then combined by calculating the standard deviation for each radii combination, using all 20 sources for each calculation. The result can be seen in figures 5-7 and 5-8 below (this is the 'sigma' variable in the photometry program).

In these plots, the following notations are used for the different sky radii sizes:

Small	25 pixels
Medium	50 pixels
Large	100 pixels

As can be seen in the plots, a larger sky radius seems to yield a smaller flux uncertainty. That is why the largest possible sky radius of the three available has been used for each source. It is also interesting to note that for both mosaics, an aperture radius of ~4-6 pixels yields the smallest flux uncertainties.

For each 'fake' source, all pixels within the aperture are added and sky corrected. An integrated PSF (same one as for the real sources) is then used to simulate a total flux calculation. This explains why the uncertainties are high for small aperture radii (the flux is based on very few pixels).

These pre-calculated curves are used in the photometry program to estimate the flux uncertainty (1 sigma) for the used aperture and sky radius combination.

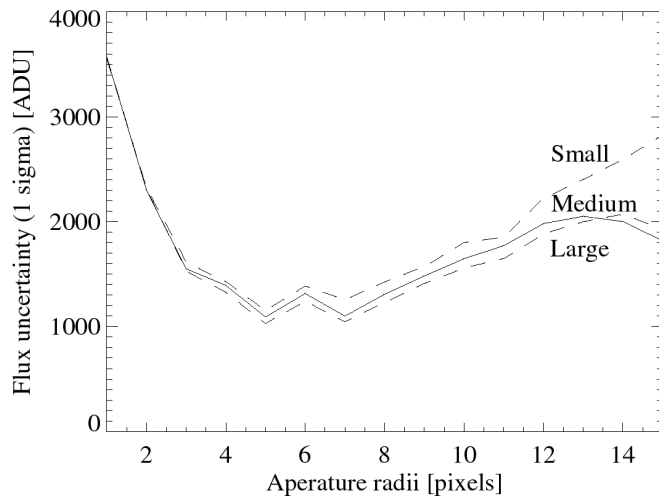


Figure 5-7. Photometric uncertainties: V filter.

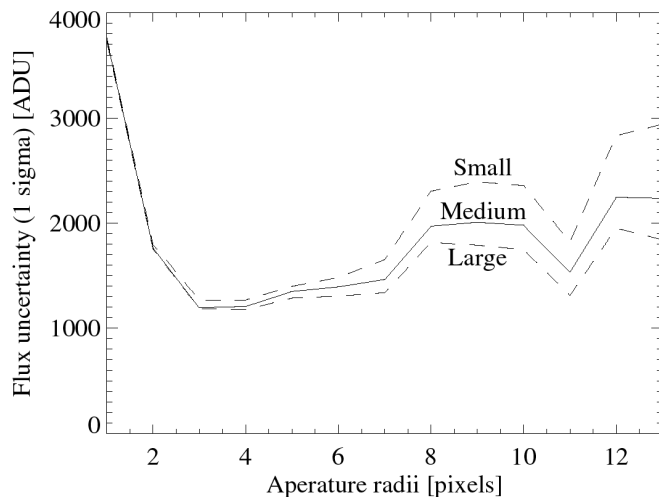


Figure 5-8. Photometric uncertainties: 1.05 μm filter.

⁶ There were $15 \cdot 3 \cdot 20 = 900$ combinations (measurements) in the V mosaic and $13 \cdot 3 \cdot 20 = 780$ combinations in the 1.05 μm mosaic.

For both filters, the systematic magnitude uncertainty (chapter 5.10.1) of 0.16 mag. is now assumed to be the minimum total uncertainty for any source. The total uncertainty of a source also depends on its flux uncertainty.

Using the magnitude formulas and flux uncertainty functions for each mosaic, the following 3σ limiting magnitudes have been estimated:

V-filter:	≥ 18.5 mag.
1.05 μm filter:	≥ 13.5 mag.

These limiting magnitudes corresponds well with the ones in chapter 5.5 obtained from the test observations (≥ 17 mag. for the V filter and ≥ 13 mag. for the 1.05 μm filter). However, these observations are slightly deeper since they were made during better conditions than the test observations. They also agree well with the weakest sources in both mosaics, ~ 18.6 and ~ 13.7 mag. respectively.

5.11 Results

In this chapter, a table of all detected ISOCAM sources in the optical (V filter) and near-IR (1.05 μm filter) mosaics is presented. These observations are then used to plot a colour/colour diagram in which it will be possible to separate intrinsic and interstellar reddening in order to confirm the previous classifications of the ISOCAM sources (sources with LW3 detections). The colour/colour diagram will also be used to classify ISOCAM sources that lack LW3 detections but are detected in the V and 1.05 μm observations.

Out of the 76 ISO sources ~ 34 % were visible in the V observations and ~ 46 % in the 1.05 μm observations down to a limiting magnitude of ~ 18.6 and ~ 13.7 mag. for the two filters respectively.

Some sources are very weak any others are not visible at all in my optical and near-IR observations, this is just what would be expected for YSO-candidates, which probably have a large IR-excess due to a circumstellar dust-shell surrounding this type of object.

Also, the optical depth is larger in the V band than the 1.05 μm -band, resulting in more sources seen in the latter.

Table 5-3. *Optical (V) and near-IR (1.05 μm) photometry of ISOCAM sources in Cep A.*

ISO-Cep	RA (1950)	DEC (1950)	F(V) [ADU]	F(1.05) [ADU]	m(V)	m(1.05)
1	22:52:56.5	61:43:38	147013 \pm 1485	10215 \pm 1816	14.26 \pm 0.17	12.34 \pm 0.27
2	22:53:06.7	61:45:43	---	13631 \pm 1339	---	12.02 \pm 0.20
5	22:53:12.8	61:48:04	1710542 \pm 1929	57341 \pm 1816	11.60 \pm 0.16	10.46 \pm 0.17
6	22:53:13.1	61:45:10	4909533 \pm 1929	159660 \pm 1748	10.45 \pm 0.16	09.35 \pm 0.16
9	22:53:25.0	61:47:59	22716 \pm 1048	6657 \pm 1816	16.29 \pm 0.17	12.80 \pm 0.39
10	22:53:25.8	61:48:57	---	2500 \pm 1394	---	13.87 \pm 0.90
13	22:53:27.7	61:46:37	3927 \pm 1395	2096 \pm 1208	18.20 \pm 0.51	14.06 \pm 0.95
15	22:53:32.0	61:49:15	1186314 \pm 1929	364559 \pm 1748	11.99 \pm 0.16	08.46 \pm 0.16
18	22:53:40.5	61:47:52	5133 \pm 1032	15624 \pm 1307	17.91 \pm 0.30	11.88 \pm 0.19
20	22:53:43.4	61:38:08	---	12615 \pm 1339	---	12.11 \pm 0.21
21	22:53:44.1	61:48:39	3028 \pm 1243	---	18.48 \pm 0.60	---
22	22:53:44.6	61:46:38	4686 \pm 1243	---	18.01 \pm 0.38	---
23	22:53:45.1	61:44:33	699546 \pm 1929	37825 \pm 1339	12.57 \pm 0.16	10.92 \pm 0.17
24	22:53:47.8	61:41:38	80688 \pm 1048	137002 \pm 1791	14.91 \pm 0.16	09.52 \pm 0.16
27	22:53:52.4	61:54:01	---	3660 \pm 1177	---	13.45 \pm 0.45
28	22:53:53.4	61:54:32	---	42167 \pm 1339	---	10.80 \pm 0.17
29	22:53:57.9	61:38:46	---	9177 \pm 1816	---	12.45 \pm 0.29
30	22:53:59.5	61:48:22	7019 \pm 1032	36595 \pm 1791	17.57 \pm 0.24	10.95 \pm 0.17
31	22:54:02.7	61:44:11	---	32621 \pm 1816	---	11.08 \pm 0.18
35	22:54:07.8	61:48:32	4299 \pm 1387	5250 \pm 1483	18.10 \pm 0.46	13.06 \pm 0.40
37	22:54:10.5	61:48:23	1978071 \pm 1929	861238 \pm 1843	11.44 \pm 0.16	07.52 \pm 0.16
39	22:54:13.0	61:43:37	7549 \pm 1560	8069 \pm 1816	17.49 \pm 0.30	12.59 \pm 0.32
43	22:54:15.5	61:37:57	13232 \pm 1243	89683 \pm 1791	16.88 \pm 0.20	09.98 \pm 0.17
47	22:54:19.3	61:53:22	---	12422 \pm 1816	---	12.12 \pm 0.24
48	22:54:24.5	61:50:25	1326908 \pm 1929	278689 \pm 1952	11.87 \pm 0.16	08.75 \pm 0.16
52	22:54:27.5	61:54:19	---	2940 \pm 1288	---	13.69 \pm 0.65
57	22:54:34.7	61:48:47	167528 \pm 1560	20729 \pm 1791	14.12 \pm 0.16	11.57 \pm 0.19
59	22:54:39.6	61:54:07	---	14222 \pm 1339	---	11.98 \pm 0.20
60	22:54:40.6	61:45:01	4312 \pm 1243	9232 \pm 1816	18.10 \pm 0.41	12.45 \pm 0.29
61	22:54:44.5	61:51:25	3335142 \pm 1929	299115 \pm 1843	10.87 \pm 0.16	08.67 \pm 0.16
62	22:54:46.3	61:50:51	64331 \pm 1649	4979 \pm 1465	15.16 \pm 0.17	13.12 \pm 0.42
63	22:54:48.8	61:54:36	2655 \pm 1243	7687 \pm 1339	18.62 \pm 0.71	12.65 \pm 0.27
68	22:54:57.5	61:41:27	2644 \pm 1032	11539 \pm 1791	18.63 \pm 0.57	12.20 \pm 0.25
69	22:55:08.2	61:46:07	3151729 \pm 1929	100614 \pm 1748	10.93 \pm 0.16	09.85 \pm 0.16
72	22:55:26.2	61:46:59	58110 \pm 1411	19971 \pm 1339	15.27 \pm 0.17	11.61 \pm 0.18
74	22:55:32.5	61:46:55	3129 \pm 1317	---	18.45 \pm 0.62	---
75	22:55:33.2	61:42:56	---	8354 \pm 1177	---	12.56 \pm 0.23

The magnitude uncertainties quoted in table 5-3 above are the total uncertainty obtained from adding the linear approximation and flux uncertainties in quadrature. Sources with mid-IR excess in the m(1.05)–m(6.7) index are marked with bold source designations.

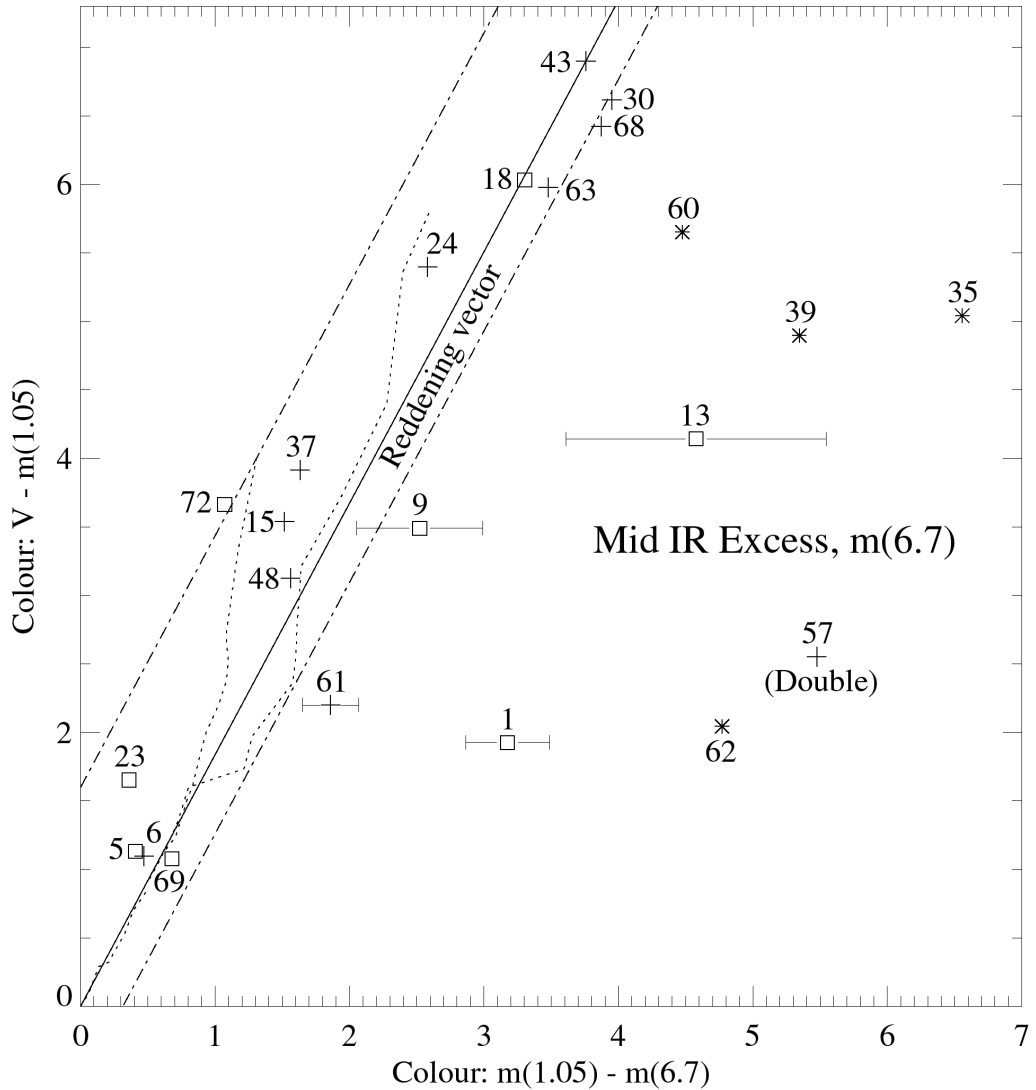


Figure 5-9. Colour / Colour diagram of all sources detectable in both the V and 1.05 μm mosaics. 'ISO red' sources are marked with asterisks, 'ISO blue' sources with plus signs and sources not seen in LW3 with squares. Intrinsic colours for giants (left dotted curve) and dwarfs (right dotted curve) are also plotted.

In this colour/colour diagram, sources classified as 'red' using the ISO $m(6.7)\text{-}m(14.3)$ colour index are marked with asterisks while those classified as 'blue' are marked with crosses. Sources not seen at $14.3 \mu\text{m}$ (and therefore not classified) are marked with squares. Intrinsic colours as interpolated from standard photometric bands (Bessell & Brett. 1988, Leggelt. 1992) have been plotted for dwarfs (spectral classes B8-M6) and giants (G0-M5) using dotted lines (located in the reddening band). The detection limit of a background source (neglecting extinction) corresponds to an M0-dwarf.

We see both the effects of interstellar reddening and intrinsic mid-IR excess (at $6.7 \mu\text{m}$). The reddening vector represents the interstellar reddening curve for an A0 star and has been approximated by fitting a line from the origo, using known ISO-blue sources to make the fit (except for the suspected binary source ISO-Cep-57). The diagram was obtained by using my observations combined with the ISO observations and it generally agrees with the blue/red

source classifications made earlier using ISO data only. The sources with red $m(6.7)-m(14.3)$ colours also seen in the V and $1.05\ \mu\text{m}$ passbands are all located to the red side of the reddening band, confirming their intrinsic mid-IR excesses. As for the ISO blue sources, all except source ISO-Cep-57 show no signs of a significant intrinsic mid IR reddening.

Sources ISO-Cep-9 and ISO-Cep-61 both have small mid-IR excesses, yet they cannot be classified as YSO-candidates solely from this plot since they may well be located within the reddening band as shown by their uncertainties.

Source ISO-Cep-57 however is an ISO-blue source which is located to the red side of the reddening band, still it cannot be classified as having an intrinsic mid-IR excess since additional observations (2MASS observations, chapter 6.1) has shown this source to be a binary-star (not resolved in the V, $1.05\ \mu\text{m}$ or ISO observations), making its position in the colour-diagram very unreliable. Furthermore, it shows no mid-IR excess in the 2MASS colour/colour diagrams (chapter 6.1.2) in which its 'double nature' has been taken into account.

Also, the ISO-blue sources ISO-Cep-15 and ISO-Cep-68, lying very close to the ISO-red limit, are in this plot supported as being blue.

Two sources, ISO-Cep-1 and ISO-Cep-13, not detected in the LW3 filter are located deep inside the intrinsic mid-IR excess region and are thus added to the list of sources with mid-IR excess (YSO candidates).

6. Additional Near-IR observations

Some other relevant observations have been done in the Cepheus A region, especially the recently started 2MASS survey which as of yet roughly covers the north and central regions of the ISO-observations. This is an ongoing survey and will cover the whole sky when finished. There are also close-up observations available of the central region.

6.1 The 2MASS survey

It has almost been 30 years since the last large area near-IR survey of the sky was carried out, it was called the Two Micron Sky Survey (TMSS) and scanned ~70% of the sky, detecting ~5700 sources of infrared radiation. Now there exists technology making it possible to detect sources over 10^8 times fainter than those detected in the TMSS.

The recently started Two Micron All Sky Survey (2MASS) is uniformly scanning the entire sky in 3 near-IR passband filters, detecting point-sources down to a flux detection-limit of about 1 mJy in each band!

This survey uses two new, highly automated 1.3m telescopes (at Mt.Hopkins, USA and CTIO, Chile) equipped with a three-channel camera, each channel consisting of a 256x256 pixel array of HgCdTe detectors, observing simultaneously at J (1.25 μm), H (1.65 μm) and K_S (2.17 μm).

I have used the most recent data available from the survey, called "The 2MASS Spring 1999 data release", it involves FITS Atlas images in the J, H and K_S bands as well as a Point Source Catalog (PSC) containing astrometry and photometry.

Since I have used the online-version of the catalogue (over 0.5 Tb for the uncompressed version, not kept online) when retrieving the Atlas-images, the images are 20:1 lossy compressed and may therefore be unreliable for direct photometry. However, photometry has already been carried out on the uncompressed Atlas-images and is available in the PSC.

6.1.1 Identification of ISOCAM sources

The subpart of the PSC that I have used contains 718 sources (some artefacts) down to a K_S magnitude of 15.0.

In order to be able to compare ISOCAM coordinates with PSC coordinates grafically it is yet again necessary to establish a relationship between equatorial coordinates and the ('Atlas images') pixel coordinates, this is done in the same manner as in chapter 5.8. Since the catalogue is sorted in right ascension, a known RA coordinate of an ISO source can be found in the table and about 8 possible candidates (four to each side of the ISO coordinate) are then circled along with the ISO source in the Atlas images. One is then left with one or maybe two (sometimes none) possible candidates. In order to further verify the choice of counterparts (if any) for the ISO source, I have carried out photometry directly on the images using the same

photometry program (Appendix B) that I used for my visual & near-IR observations. I have also done photometry on ISO source counterparts that are clearly visible in the Atlas images, however not listed in the PSC.

For the Cep A region of the 2MASS spring 1999 data release (roughly the central and north regions of the ISOCAM observations) there are 32 ISO sources available. All except one (ISO-Cep-42) could be identified with a near-IR counterpart in at least one of the three images. Photometry is available for all ISO sources except ISO-Cep-42 (not detected in near-IR) and ISO-Cep-26 (too close to the southern edge of the images for photometry).

In figure 6-1 all ISOCAM sources in the 2MASS region are circled and numbered on top of the 2MASS K_s image.

All ISOCAM sources except ISO-Cep-42 appears to have a near-IR counterpart in the region covered by the 2MASS survey. ISO-Cep-42 is however bright in both the LW2 and LW3 ISOCAM mosaics! It could be a very embedded star lying at an extreme optical depth in K_s .

ISO-Cep-26 is clearly visible, however it lies too close to the southern edge in the 2MASS images in order to be measured with photometry.

ISO-Cep-21 is clearly a double star and ISO-Cep-36 does also show (photometric) signs of being a double.

ISO-Cep-46 is very close to the centre of Cep A, it is much brighter at longer wavelengths than shorter (for instance very bright in K_s however barely detectable in the J observations). ISO-Cep-25 has a very diffuse and extended counterpart.

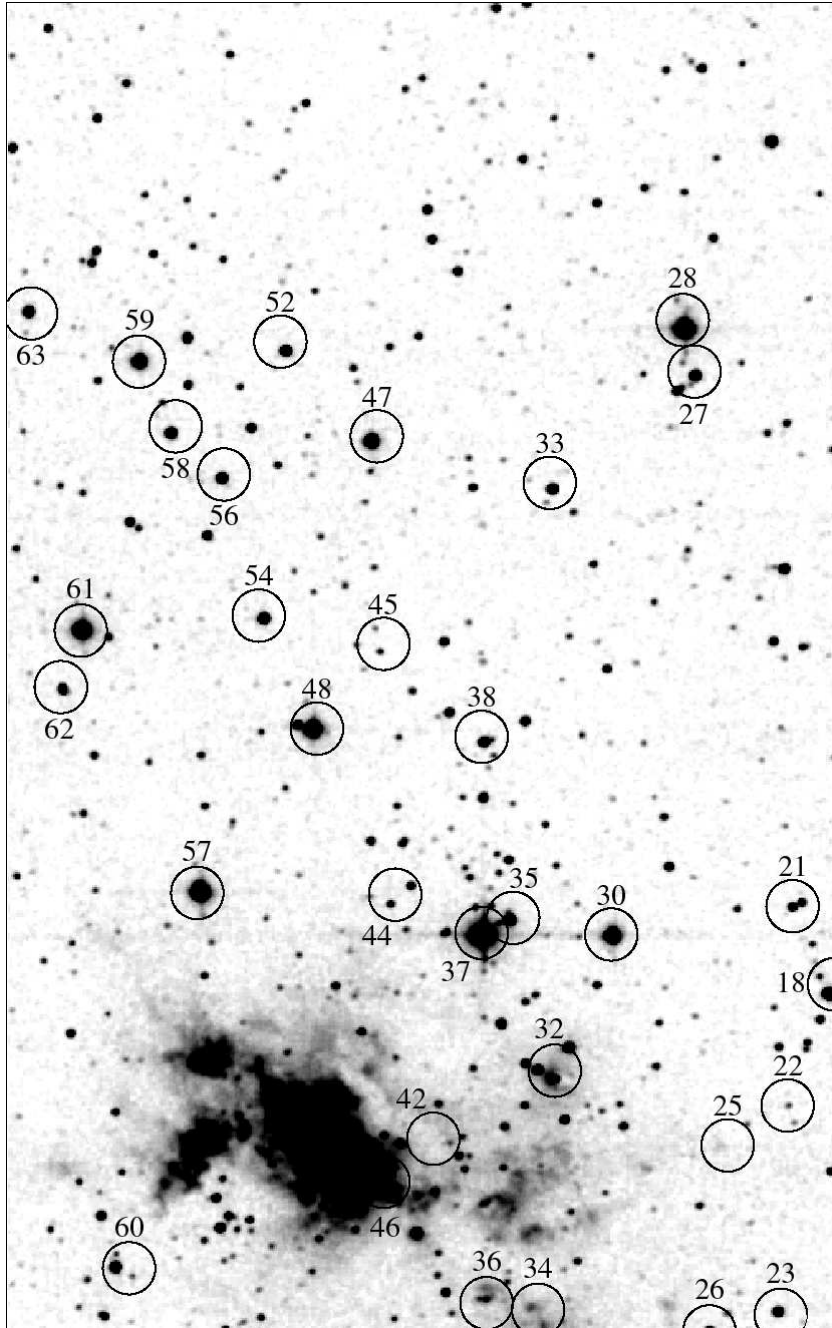


Figure 6-1. 2MASS K_s ($2.17 \mu\text{m}$) image ($8.5' \times 13.4'$) with ISOCAM sources circled (using a circle diameter of $0.5'$).

6.1.2 Results

Photometry of the 2MASS data are presented in table 6-1 below, both from the PSC and aperture photometry carried out directly on the images. Sources with mid-IR excess in the $K_S-m(6.7)$ or $H-m(6.7)$ indices are marked with bold source designations.

Table 6-1. Near-IR (2MASS J , H and K_S) photometry of ISOCAM sources in Cep A.

ISO nr	Near-IR counterpart		2MASS Spring'99 Release PSC			Image photometry			Remarks
	RA(2000)	DEC(2000)	m_J	m_H	m_{K_S}	m_J	m_H	m_{K_S}	
18	22:55:39.5	62:03:49	10.67 ± 0.04	09.54 ± 0.04	09.02 ± 0.03	10.58	09.37	09.01	
21	22:55:41.8	62:04:44	13.63 ± 0.05	12.50 ± 0.05	11.98 ± 0.04	13.57	12.36	11.98	Binary
	22:55:42.6	62:04:41	13.74 ± 0.04	12.38 ± 0.04	11.59 ± 0.04	13.67	12.27	11.51	
22	22:55:43.0	62:02:41	14.43 ± 0.05	13.84 ± 0.06	13.61 ± 0.05	14.39	13.56	13.57	
23	22:55:43.9	62:00:38				10.72	10.51	10.48	GSC
25	22:55:48.1	62:08:01				---	---	13.92	Extended
27	22:55:50.9	62:10:03	12.39 ± 0.04	10.50 ± 0.04	09.69 ± 0.03	12.26	10.43	09.75	
28	22:55:51.8	62:10:32	09.38 ± 0.04	07.58 ± 0.04	06.74 ± 0.04	09.23	07.79	07.11	
30	22:55:58.0	62:04:24	09.84 ± 0.04	08.24 ± 0.04	07.60 ± 0.04	09.72	08.26	07.68	
32	22:56:03.0	62:02:57	---	14.69 ± 0.11	12.07 ± 0.05	---	14.58	11.92	Central M
33	22:56:03.2	62:08:55	12.76 ± 0.04	10.98 ± 0.04	10.34 ± 0.02	12.62	10.92	10.35	
34	22:56:05.1	62:00:39	---	~ 14.50	13.95 ± 0.09	---	14.76	13.30	Extended
35	22:56:06.9	62:04:34	11.80 ± 0.04	10.38 ± 0.04	09.33 ± 0.03	11.63	10.25	09.34	
36	22:56:08.9	62:00:44	16.03 ± 0.13	14.44 ± 0.08	13.08 ± 0.07	15.84	14.11	13.05	Close
	22:56:09.6	62:00:45	~ 16.19	14.93 ± 0.11	13.70 ± 0.09	16.10	14.70	13.63	Binary
37	22:56:09.2	62:04:25	06.92 ± 0.03	06.01 ± 0.04	05.67 ± 0.04	07.20	06.78	06.46	GSC
38	22:56:09.1	62:06:22	12.62 ± 0.04	10.87 ± 0.04	10.16 ± 0.03	12.48	10.78	10.20	
44	22:56:17.1	62:04:44	~ 16.24	13.91 ± 0.06	12.44 ± 0.03	16.43	13.81	12.47	
45	22:56:18.0	62:07:16	14.81 ± 0.06	13.63 ± 0.05	13.00 ± 0.04	14.74	13.52	13.02	
46	22:56:18.6	62:02:01	15.37 ± 0.14	11.56 ± 0.08	08.48 ± 0.09				Central M
47	22:56:18.7	62:09:24	10.84 ± 0.04	09.01 ± 0.04	08.15 ± 0.03	10.74	08.92	08.20	
48	22:56:23.7	62:06:30	08.29 ± 0.03	07.58 ± 0.04	07.31 ± 0.05	08.29	07.73	07.42	GSC
52	22:56:26.1	62:10:18	12.20 ± 0.04	10.71 ± 0.04	10.12 ± 0.03	12.06	10.63	10.13	
54	22:56:28.0	62:07:36	11.75 ± 0.04	10.19 ± 0.04	09.55 ± 0.03	11.64	10.12	09.56	
56	22:56:31.6	62:09:01	12.44 ± 0.04	10.62 ± 0.04	09.81 ± 0.03	12.35	10.54	09.89	
57	22:56:33.4	62:04:51	10.17 ± 0.05	07.92 ± 0.04	06.86 ± 0.04	09.94	07.93	07.08	Close
	22:56:33.6	62:04:55	12.33 ± 0.12	~ 09.16	~ 08.23	11.72	10.51	09.92	Binary
58	22:56:36.0	62:09:29	12.28 ± 0.04	10.51 ± 0.04	09.73 ± 0.03	12.16	10.43	09.77	
59	22:56:38.7	62:10:12	10.63 ± 0.04	08.99 ± 0.04	08.29 ± 0.03	10.53	08.93	08.33	
60	22:56:40.7	62:01:04	11.99 ± 0.04	10.73 ± 0.04	09.88 ± 0.03	11.88	10.65	09.94	
61	22:56:43.6	62:07:29	07.88 ± 0.03	07.35 ± 0.04	07.14 ± 0.04	07.91	07.51	07.39	GSC
62	22:56:45.3	62:06:53	12.43 ± 0.05	11.57 ± 0.04	10.89 ± 0.04	12.15	11.33	10.82	
63	22:56:48.3	62:10:42	11.49 ± 0.04	10.24 ± 0.04	09.74 ± 0.04	11.36	10.18	09.79	

In table 6-1, the following remarks are used:

GSC	A star present in the ‘Guide Star Catalogue’
Central M	One of the sources seen very close to Cep A in the ISO Cep A central mosaic
Extended	The photometry is uncertain, a PSF could not be used
Binary	Wide optical binary. Probably seen as a single source in the ISOCAM observations
Close Binary	Overlapping sources, uncertain photometry due to inseparable PSFs of components

The ‘Image photometry’ uncertainty is at least ± 0.05 mag. since it is based on only one A0 star with the same uncertainty, however, it is probably much larger for some sources since the image photometry was carried out on 20:1 lossy-compressed 2MASS images. The corresponding photometry from the 2MASS Spring’99 Release PSC were done directly on the uncompressed images, thus the smaller uncertainties.

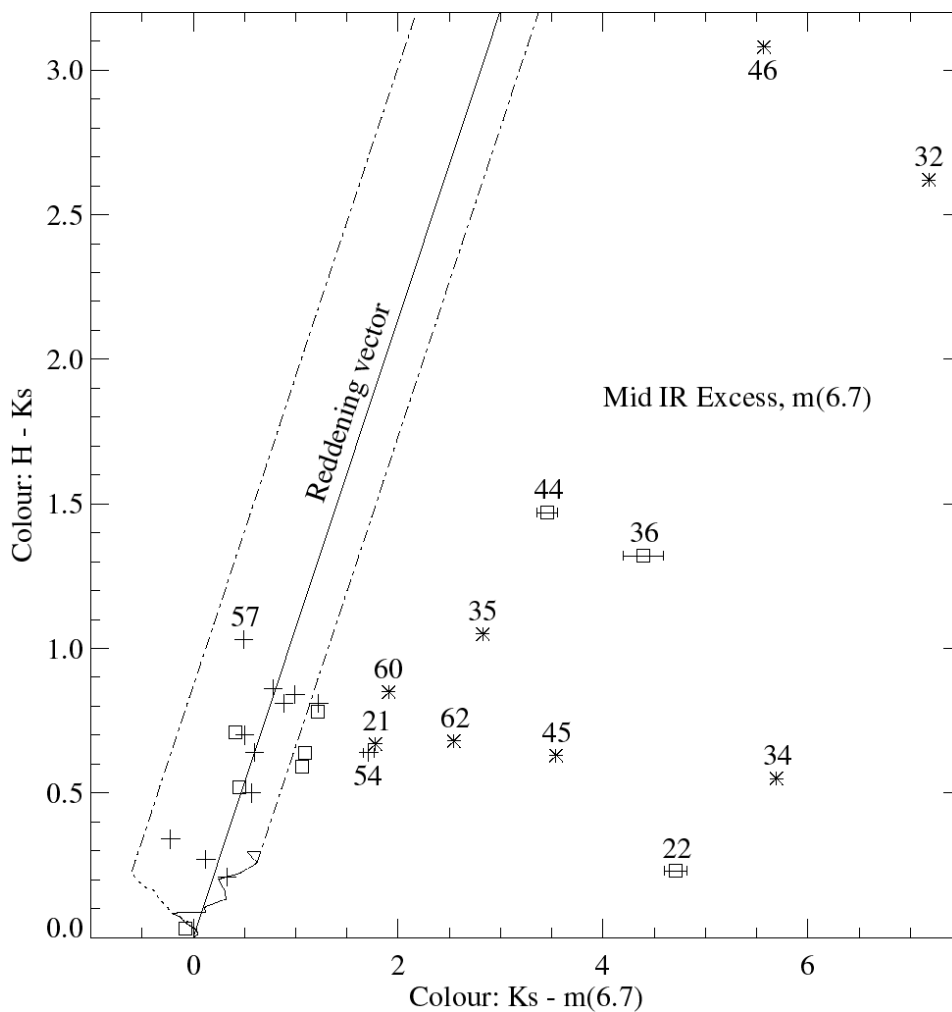


Figure 6-2. Mid / Near infrared colour/colour diagram $H-K_s$ versus $K_s-m(6.7)$.

In the Mid / Near IR colour/colour diagrams (figures 6-2 and 6-3) we see both the effects of interstellar reddening and intrinsic mid-IR excess (at $6.7 \mu\text{m}$). Intrinsic colours for dwarfs (spectral classes B8-M6) are shown as solid curves while giants (G0-M5) are shown as dotted curves in these diagrams.

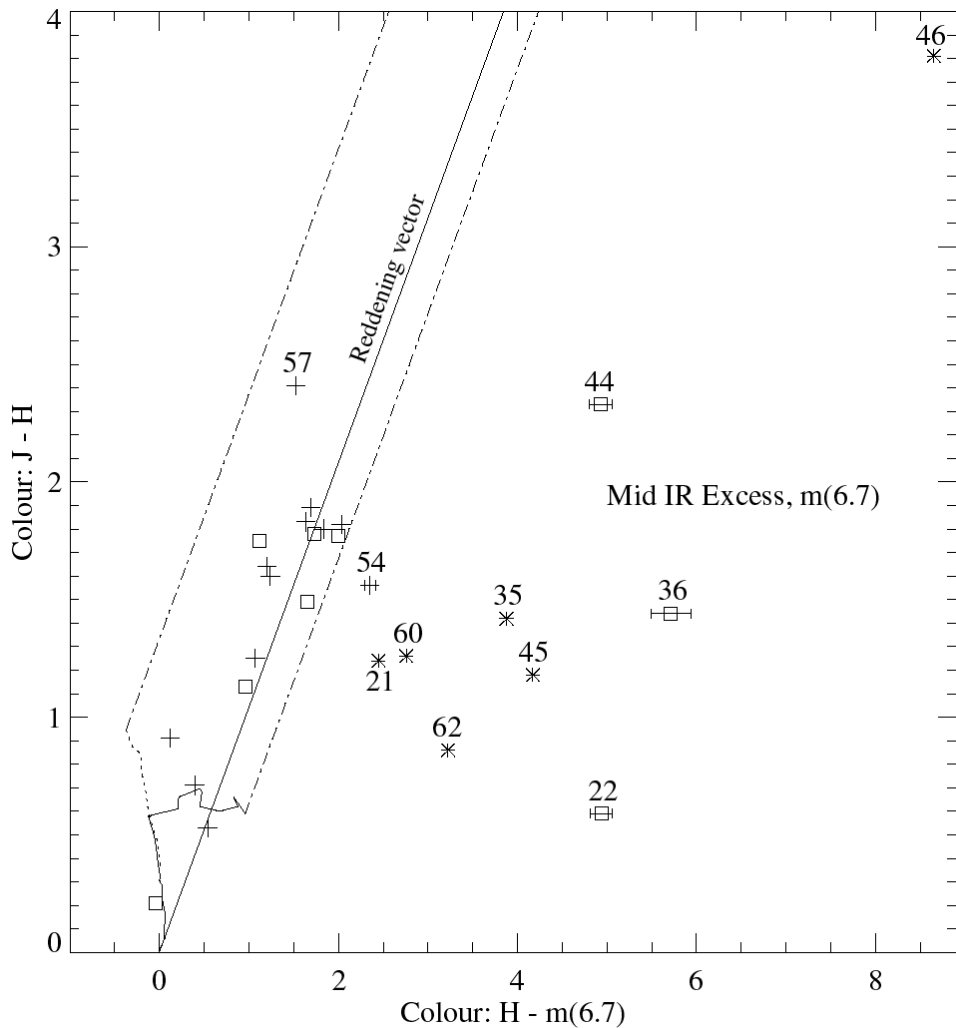


Figure 6-3. Mid / Near infrared colour/colour diagram $J-H$ versus $H-m(6.7)$.

Background stars (not intrinsically red) are revealed in these colour/colour diagrams as reddened stars scattered along an interstellar reddening vector. Some stars along this line (located close to origo) could also be foreground stars. This reddening vector represents the interstellar reddening curve for an A0 star and may differ between different clouds, it has not yet been accurately determined, but we see that the mid-IR reddening as determined for three other clouds (see Bontemps et al. 1999, Kaas et al. 1999 and G. Olofsson et al. 1999) agrees well with the Cep A data presented in this chapter, all four clouds having reddening vector slopes a little bit above 1.0 (Figure 6-2 and 6-3 have slopes of 1.07 and 1.04 respectively) The reddening vectors have been calculated by fitting a line from the origin through ISO sources without mid-IR excess (at $14.3 \mu\text{m}$).

In these colour/colour diagrams it is clear that sources that are 'red' in the $m(6.7)-m(14.3)$ index are 'red' also in $K_S-m(6.7)$ and $H-m(6.7)$. All the ISO-blue sources, except ISO-Cep-54, are 'blue' in these colour/colour diagrams as well. The ISO-blue source ISO-Cep-54 is in fact 'red' in the $K_S-m(6.7)$ and $H-m(6.7)$ indices. It is also located close to the 'red/blue limit' in the ISO observations (figure 4-2), it is therefore added to the sources with mid-IR excess.

ISO-Cep-22, 36 and 44 all have apparent intrinsic K_S -m(6.7) and H-m(6.7) excesses (located far away from the reddening band relative to their uncertainties), therefore they are also added to the list of sources with mid-IR excesses (YSO-candidates).

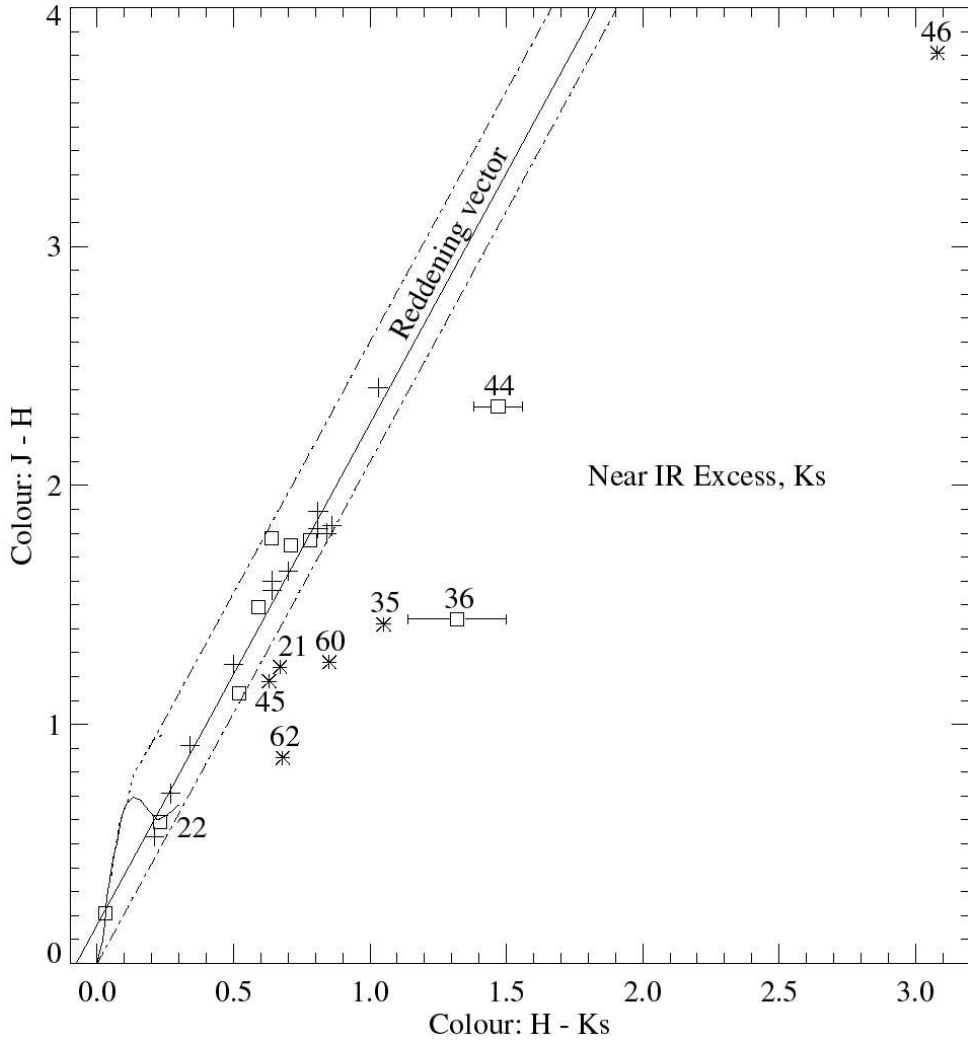


Figure 6-4. Near infrared colour/colour diagram $J-H$ versus $H-K_S$.

In the third colour/colour diagram (figure 6-4), the near-IR excess at $2.17 \mu\text{m}$ (K_S) is presented. Intrinsic colours for dwarfs (B8-M6) and giants (G0-M7) have also been plotted.

As for the near-IR excesses there are no surprises, all ISO-red sources are 'red' and all ISO-blue sources are 'blue'. However, ISO-Cep-22 lacks near-IR excess even though it was found to have a mid-IR excess in both the K_S -m(6.7) and H-m(6.7) indices. This again shows the fact that $J-H / H-K$ diagrams are far less efficient than the mid-IR excess diagrams and the single ISOCAM colour index [14.3/6.7] in extracting IR excess sources. In fact, its efficiency has been estimated to less than 50% (Kaas et al. 1999).

A reason for the lack of near-IR excess in sources with mid-IR excess may be explained by current models of circumstellar disks (Calvet et al. 1992, Meyer et al. 1997, Hillenbrand et al.

1998) in which an inner hole or an optically thin region with radius $\sim 3 R_*$ is sufficient to remove all the near-IR excess for all stars later than spectral class M2 if the accretion rate is slower than $10^{-8} M_{\text{Sun}} \text{ yr}^{-1}$. Modifications from the pole-on case to the most likely disk inclination of $i=60^\circ$ results in undetectable near-IR excesses even for larger stellar masses.

The detection limit of a background source (neglecting extinction) corresponds to an M3 dwarf (J), M2 dwarf (H) and an M0 dwarf (K_S), this may narrow the reddening band in the upper part of the colour/colour diagrams. However, due to the large extinction in the J-passband (compared to H and K_S) this is often the limiting factor in the colour/colour diagrams in which J-magnitudes are present.

6.2 The central Cep A region.

The central region of Cep A is very bright at mid-IR wavelengths, this causes source confusion in the ISOCAM central mosaic with its strong unremovable transients and very large contrasts. At near-IR wavelengths this region is less bright and detectors exist that makes high-resolution imaging easier. Such observations of the central Cep A region have been made by Hodapp (1994) in the near-IR K' passband ($2.17 \mu\text{m}$), see figure 6-5 below. This image has a $\approx 8' \times 3'$ field of view and is part of his survey of regions associated with CO molecular outflows.

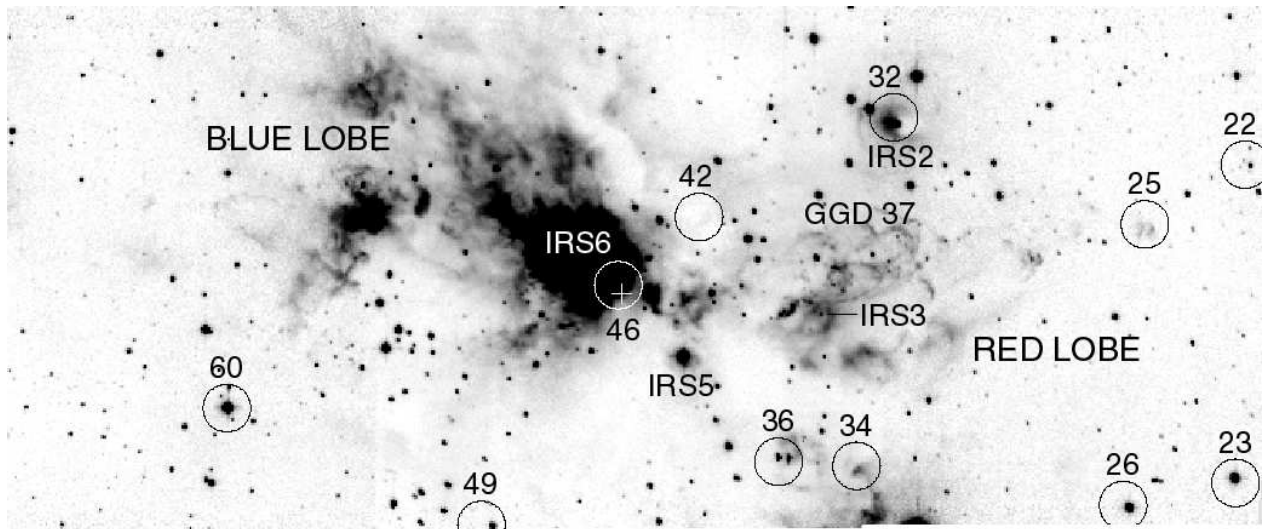


Figure 6-5. *High resolution K' image of the central Cepheus A region.*

In this K' image the red and blue outflows of a central source can easily be seen as two lobes in roughly opposite directions (the high and low speed outflows of each lobe are directed at slightly different angles). Located at the red lobe's northern edge is the suspected Herbig-Haro object GGD 37, seen as several bright arcs in this image.

Several of the IR-sources designated IRS1-8 (Lenzen, Hodapp and Solf. 1984) can be seen in the image, in particular IRS6 at the centre of the image is an IR reflection nebula,

reflecting light off the innermost parts of the cavity created by the bipolar outflow that originates from a central source (close to ISO-Cep-46).

ISO-Cep-32 is clearly visible close to the centre of the IR-source IRS2. This source is very faint at optical wavelengths and is not seen in the POSS-prints as pointed out by Lenzen et al.

ISO-Cep-36 is here clearly separated into two components proving it to be a double star, this is not seen in either the ISO, 2MASS near-IR or my V, 1.05 μm observations.

ISO-Cep-42 is very strong in the mid-IR ISOCAM observations, however, it is not seen at all in this near-IR image. This suggests that ISO-Cep-42 is deeply embedded and is subject to very large near-IR extinction.

ISO-Cep-46 is located very close to the source of the bipolar outflow, as can be seen by comparing its position with that of the converging position of the 3.6 μm polarization-map of Lenzen et al. (1984). The deviation is only $\sim 3''$ which agrees well within the uncertainties. They interpreted this converging region ($< 4''$) as the position of a point-like illuminating source of IRS6(a). ISO-Cep-46 also lies close to several ultracompact H II regions, especially HW2 (marked with a cross in figure 6-5) which is thought to be the driving source of the molecular outflow (Bergin et al. 1997).

All other ISOCAM sources present are confirmed in this image except ISO-Cep-25 which looks more like a 'gas-knot' or a patch of nebulosity, since it lacks the appearance of a point source (it could however be a deeply embedded point source).

7 Summary of results

A $\sim 20' \times 20'$ (0.09 square degrees) region centered on Cep A has been imaged by ISOCAM onboard the ISO satellite using two mid-IR filters: LW2 (6.7 μm) and LW3 (14.3 μm). For each filter, five overlapping regions were observed.

All observations were dark corrected⁷ (removing the odd-even line sensitivity variations), de-glitched (removing streaks caused by particle impacts), transient corrected (removing memory effects caused by the detector's slow response to a large flux step), masked (removing bad pixels) and finally flatfielded (making all pixels in the array equally sensitive).

After these corrections had been successfully performed, source detection and photometry was carried out. The regions were also put together into two mosaics for each filter (the central region of both filters were too bright to make just one mosaic for each filter).

A total of 76 sources were detected in the 6.7 μm images while 41 of these were detected in the less sensitive 14.3 μm images. These 41 sources could then be classified and 18 were found to have mid-IR excess and were thereby classified as YSO-candidates.

The 6.7 μm observations were then combined with visual (V) and near infrared (1.05 μm , J, H and K_S) observations which confirmed all (9) detectable ISO 'red' sources as having mid-IR excess. All except one (16 out of 17) detectable ISO 'blue' sources were confirmed as lacking mid-IR excess. The ISO 'blue' source ISO-Cep-54 showed an IR-excess and achieved an YSO-candidate status. Also, 15 sources not detected at 14.3 μm could be classified, resulting in 5 more mid-IR excess sources.

This yields a **total of 24 sources with IR-excess** (YSO-candidates).

Although 9 of these YSO candidates were undetectable at optical and near-IR wavelengths it is very likely that their IR excesses are intrinsic since all 15 IR excess sources that were detectable at these wavelengths confirmed their excesses as intrinsic. It is also important to note that the near-IR J, H and K_S data from the 2MASS survey (as of yet) only cover the central and northern part ($\sim 45\%$) of the Cep A region observed.

Details on all observations, the data reduction and colour/colour diagrams etc. leading to the results above are given in each chapter.

In this chapter, the luminosity-mass function of chapter 1.2 will be used to calculate the mass spectrum and also a convenient table is presented in which photometry of mid-IR excess sources from all observations are included: Stockholm Observatory (V, 1.05 μm ; visual and near-IR), 2MASS (J, H, K_S ; near-IR) and ISOCAM (6.7, 14.3 μm ; mid-IR).

⁷ The central region (both LW2 and LW3) actually required a second order dark-correction (see chapter 3.5).

Table 7-1. *Cep A ISOCAM sources with mid-IR excess (YSO-candidates).*

ISO #	Epoch 1950		Stock. Obs.		2MASS			ISOCAM		$\alpha_{6.7-14.3}$	Remarks
	RA	DEC	V	1.05	J	H	K _S	6.7	14.3		
1	22:52:56.5	61:43:38	14.26	12.34	out	out	out	9.16	---	---	
10	22:53:25.8	61:48:57	---	13.87	out	out	out	9.06	7.69	-1.30	
13	22:53:27.7	61:46:37	18.20	14.06	out	out	out	9.48	---	---	
21	22:53:44.1	61:48:39	18.48	---	12.93	11.69	11.02	9.24	7.17	-0.43	Binary
22	22:53:44.6	61:46:38	18.01	---	14.43	13.84	13.61	8.90	---	---	
26	22:53:51.2	61:44:23	---	---	out	out	out	6.36	3.56	+0.44	
32	22:54:04.3	61:47:00	---	---	---	14.69	12.07	4.89	3.16	-0.85	
34	22:54:05.8	61:44:35	---	---	---	~14.50	13.95	8.26	6.47	-0.78	Extended
35	22:54:07.8	61:48:32	18.10	13.06	11.80	10.38	9.33	6.50	4.68	-0.74	
36	22:54:10.2	61:44:40	---	---	~15.35	13.91	12.59	8.20	---	---	Binary
39	22:54:13.0	61:43:37	17.49	12.59	out	out	out	7.25	5.12	-0.37	
41	22:54:14.4	61:39:08	---	---	out	out	out	9.19	7.98	-1.49	
44	22:54:17.8	61:48:46	---	---	~16.24	13.91	12.44	8.98	---	---	
45	22:54:18.8	61:51:16	---	---	14.81	13.63	13.00	9.46	7.59	-0.69	
46	22:54:18.9	61:45:53	---	---	15.37	11.56	8.48	2.91	-0.24	+0.87	Central source
49	22:54:26.5	61:44:14	---	---	out	out	out	9.25	7.31	-0.61	
50	22:54:26.2	61:41:47	---	---	out	out	out	9.80	7.19	+0.22	
51	22:54:26.9	61:43:53	---	---	out	out	out	10.08	8.13	-0.59	
54	22:54:29.4	61:51:34	---	---	11.75	10.19	9.55	7.84	7.07	-2.02	
60	22:54:40.6	61:45:01	18.10	12.45	11.99	10.73	9.88	7.97	5.88	-0.41	
62	22:54:46.3	61:50:51	15.16	13.12	12.43	11.57	10.89	8.35	6.88	-1.18	
65	22:54:49.9	61:41:47	---	---	out	out	out	8.63	6.52	-0.38	
67	22:54:53.9	61:41:56	---	---	out	out	out	8.85	6.47	-0.07	
74	22:55:32.5	61:46:55	18.45	---	out	out	out	11.98	8.55	+1.21	

In table 7-1 above, 'out' means that no photometry could be obtained from the 2MASS data since the source is located outside the 2MASS observed region. Class II YSOs are marked with bold $\alpha_{6.7-14.3}$ indices. Photometry uncertainties are given in each corresponding observation chapter. Magnitudes of binary stars include both components while in chapter 6.1.2. the magnitude of each component is given in the 2MASS photometry. The ISOCAM photometry uncertainties are ~ 0.08 mag (LW2) and ~ 0.10 mag (LW3) for all sources except ISO-Cep-74 (~ 2 and 0.35 mag respectively).

When calculating the mass spectrum using the $6.7 \mu\text{m}$ magnitudes listed in table 7-1 it is necessary (preferably) to correct these for extinction wherever possible. For YSOs with H and K_S photometry available the extinction at $6.7 \mu\text{m}$ can be estimated as follows:

The relative and absolute extinctions at λ_1 and λ_2 are related as $E_{\lambda_1-\lambda_2} = A_{\lambda_1} - A_{\lambda_2}$

If the extinction in near-IR is assumed to be caused by scattering alone it can be written as a power law:

$$A_{\lambda} = \text{Const} / \lambda^{\beta} \quad \text{where } 0.7 \lesssim \lambda \lesssim 2.5 \mu\text{m}$$

From figure 6-4 (reddening vector) we see that $(E_{J-H}) / (E_{H-K_s}) \approx 2.097$, this yields $\beta \approx 2.635$.

If we now (as is usually done) extrapolate A_λ to infinite wavelengths, we can calculate the absolute extinction at K_s :

$$\frac{E_{H-K_s}}{E_{K_s-\infty}} = \frac{E_{H-K_s}}{A_{K_s}} \approx \frac{1.65^{-2.635} - 2.17^{-2.635}}{2.17^{-2.635}} \approx 1.058$$

This yields $A_{K_s} \approx 0.945 \cdot E_{H-K_s}$

Examining figure 6-2, the reddening vector gives $E_{H-K_s} \approx 1.069 \cdot E_{K_s-m(6.7)} \Rightarrow A_{6.7} \approx 0.01 \cdot E_{H-K_s}$

The extinction $A_{6.7}$ is thereby found to be small enough to neglect in further calculations. This is quite suprising and may indicate that the extrapolation of the extinction formula to infinity wavelengths is too rough an assumption to make, this would certainly be the case if there is an additional scattering component present in the extinction formula, this depends on the size variations of the dust grains. It is however beyond the scope of this master thesis to investigate this further, however, it may be discussed in greater detail in a forthcoming paper on the ISOCAM observations of Cep A.

G. Olofsson has found an empirical Flux-Luminosity relationship valid for Class II objects, using two other molecular clouds (RCrA and Cha.I) yielding the following combined fit (for a distance of 129 pc):

$$\log(L/L_{\text{sun}}) \approx \log(F_{6.7, JY}) + 0.34$$

Translated to the Cep A distance of 730 pc and recalculating to magnitudes this becomes:

$$\log(L/L_{\text{sun}}) \approx 3.765 - 0.4 \cdot m_{6.7}$$

Source luminosities can now be calculated for the class II objects of table 7-1. This will also be done for ISO-Cep-54 (small α) and the sources that lacks spectral index measurements since these almost certainly are class II/III objects, and the differences between class II and class III objects are very subtle and the transition is gradual.

Figure 7-1 shows the derived luminosity function for the class II/III objects. There is an approximate detection limit marked with a dashed line in this figure, it has been calculated empirically and is based on the faintest sources seen in the 14.3 μm ISOCAM images.

The luminosities calculated for the (20) sources can now be used to calculate their masses by using the Luminosity-Mass relation (10^6 years single age) of chapter 1.2. This results in the mass spectrum plotted in

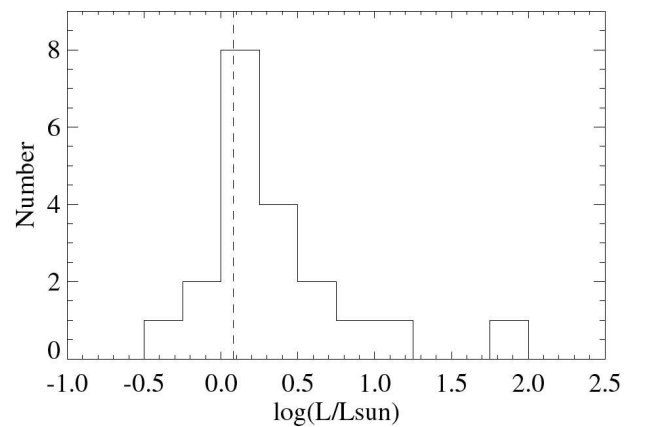


Figure 7-1. Luminosity function for the Class II and Class III source sample.

figure 7-2. Due to the relatively large distance to Cep A (730 pc) there is a detection limit of sources with masses lower than $\sim 0.7 M_{\text{sun}}$, this 'completion limit' is marked in the mass spectrum plot as a dashed line.

Also an IMF has been fitted to the data in the plot using two power law functions according to the model by Scalo (1998) that were discussed in chapter 1.3.

The fitted IMF agrees very well with the observed mass distribution!

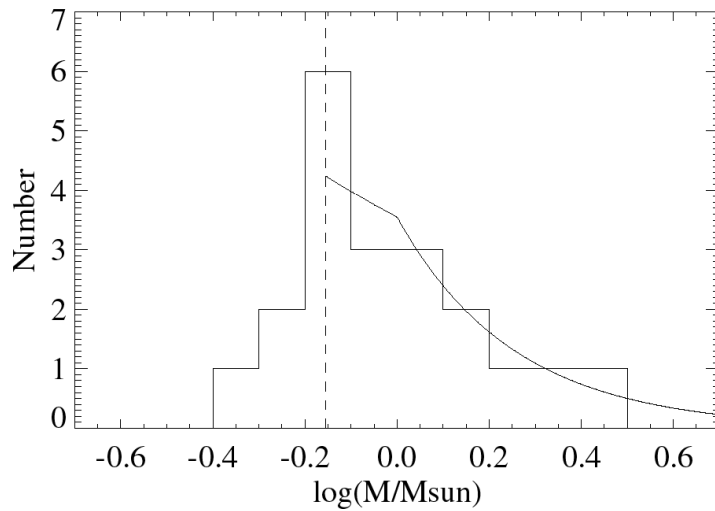


Figure 7-2. The distribution of stellar masses for the Class II and Class III YSOs with mid-IR excess emission. A theoretical IMF has also been plotted (Scalo 1998) using two power laws.

References

- Adams, Lada, Shu, 1987, *ApJ* **312**:788
- André, Ward-Thompson, Barsony, 1993, *ApJ* **406**:122
- Beichman, Becklin, Wynn-Williams, 1979, *ApJ* **232**:L47
- Bergin, Goldsmith, Snell, Langer, 1997, *ApJ* **482**:285
- Bergin, Ungerechts, Goldsmith et al., 1997, *ApJ* **482**:267
- Bessell & Brett, 1988, *Astron. Soc. of the Pacific* **100**:1134
- Blaauw, Hiltner, Johnson, 1959, *ApJ* **130**:69
- Bondtemps, Nordh, Olofsson et al., 1999, to be submitted to *A&A*
- Brown, Little, MacDonald, Riley, Matheson, 1981, *MNRAS* **195**:607
- Calvet, Magris, Patiño, Alessio, 1992, *Rev. Mexicana Astron. Astrof.* **24**:27
- Cohen et al., 1992, *AJ* **104**:1650
- D'Antona & Mazzitelli, 1997, *Mem.S.A.It.* **68**, No4
- Gonzales, *Digital Image Processing*, 1987 Addison & Wesley
- Gyulbudaghian, Glushov, Denisyuk, 1978, *ApJ* **224**:L137
- Hillenbrand, Strom, Calvet et al., 1998, *AJ* **116**:1816
- Ho, Moran & Rodriguez, 1982, *ApJ* **262**:619
- Hodapp, 1994, *ApJS* **94**:615
- Hughes & Wouterloot, 1984, *ApJ* **276**:204
- ISOCAM Observer's Manual v1.0 (The ISOCAM Team), 1994
- Kaas, Olofsson, Bondtemps et al., 1999, to be submitted to *A&A*
- Lada, Blitz, Reid, Moran, 1981, *ApJ* **243**:769
- Lada, 1987, *IAU Symp.* **115**:1
- Leggelt, 1992, *ApJS* **82**:351
- Lenzen, Hodapp, Solf, 1984, *AA* **137**:202
- Martin & Whittet, 1990, *ApJ* **357**:113
- Mayers et al, 1987, *ApJ* **319**:340
- Meyer, Calvet, Hillenbrand, 1997, *ApJ* **114**:288
- Olofsson, Hultgren, Kaas et al., 1999, accepted to *A&A*
- Rodriguez, Ho, Moran, 1980, *ApJ* **240**:L149
- Rodriguez, Moran, Ho, Gottlieb, 1980b, *ApJ* **235**:845
- Sargent, 1977, *ApJ* **218**:736
- Scalo, 1998, *ASP Conf. Ser.* **142**:201
- Shu, Adams, Lizano, 1987, *ARAA* **25**:23
- Simon & Joyce, 1983, *ApJ* **265**:864
- Starck, Abergel, Aussel et al., 1999, *A&AS* **134**:135
- Starck, Murtagh, Pirenne, Albrecht, 1996, *PASP*
- Torrelles, Ho, Rodriguez et al., 1985, *ApJ* **288**:595
- Wouterloot, Habing, Herman, 1980, *AA* **81**:L11

Appendix A – ISOCAM data reduction (one raster)

; Reduction of the ISOCAM data was done with the aid of the CIA (CAM Interactive Analysis) package.
 ; Each raster (W, E, CN, CS, CC combined with LW2 and LW3 => 10 rasters) of the Cepheus A mosaic had to be
 ; reduced separately using all the steps below...

; ***** Reading of the observed data *****

```
X_slicer ; Start the subprogram "X_slicer"
sscd = sscd_read('cssc_data*') ; Read raw data, previously selected with X_slicer
data_orig = get_raster_st(sscd) ; Create the original data structure, called data_orig
save, filename = 'data_orig.xdr', data_orig ; Store this structure on the hard-disk for safety
tmp = data_orig ; tmp is a copy of this structure, for temporary use
```

; ***** Dark and Glitch correction *****

```
x3d, tmp.cube ; View the unprocessed cube
calib_raster, tmp, /dark ; DARK CORRECTION (First order)
x3d, tmp.cube ; View the dark-corrected cube
calib_raster, tmp, deglitch = 'mm' ; GLITCH CORRECTION
x3d, tmp.cube ; View the glitch-corrected cube
save, filename = 'data_dg.xdr', tmp ; Store the dark+glitch (dg) corrected data

calib_raster, tmp, /reduce, /raster ; Reduce frames to images and calculate the raster
tviso, tmp.raster < 50 ; Display the raster, scale intensity between 0 and 50
```

; ***** Second order dark correction (if needed) *****

```
x3d, tmp.cube ; View frames, find one with 'stripes' and few sources
for i = 0, tmp.nscd-1 do print, median(tmp.image(*,*,i)) ; Compare the median of each image
; (tmp.nscd is the number of images in the raster)
tviso, tmp.raster < 50 ; Check that there is no emission at the selected frame
old = tmp.image ; "old" are the current images
new = fltarr(32,32, tmp.nscd) ; Create a matrix for the new images
for i = 0, tmp.nscd -1 do new(*,*,i) = del_pattern(old(*,*,i)) ; SECOND ORDER DARK CORRECTION
diff = fltarr(32,32, tmp.nscd) ; Create a matrix for the changes in the images
for i = 0, tmp.nscd -1 do diff(*,*,i) = old(*,*,i) - new(*,*,i) ; Calculate the image changes
tmp.image = new ; Use the new images for the calculation below...
calib_raster, tmp, /raster ; Calculate a raster, based on the new images
tviso, tmp.raster < 50 ; View the raster, see if the correction will do
```

```
for i=0, tmp.nbr_frame-1 do tmp.cube(*,*,i)=tmp.cube(*,*,i) - diff(*,*,N) ; Correct the cube, using frame N
data_dgs = tmp ; Copy the temporary structure for later use
save, filename = 'data_dgs.xdr', tmp ; Store the secondary dark corrected data
```

; ***** Transient correction *****

```
precube = fltarr(32,32,200) ; Create a pre-correction cube...
for i=0,31 do for j=0,31 do precube(i,j,0:199) = median(tmp.cube(i,j,*)) ; ...with the median image.
precube(*,*,0:199) = precube(*,*,0:199) * tmp.tint ; (tmp.tint is the integration time)
ias_cube = fltarr(32,32,tmp.nbr_frame+200) ; Create a cube consisting of...
ias_cube(*,*,0:199) = precube ; ...the precube...
ias_cube(*,*,200:tmp.nbr_frame+200-1) = tmp.cube(*,*,0:tmp.nbr_frame-1) * tmp.tint ; and the uncorrected cube.
correct_transient_ias, ias_cube, trans_cube ; TRANSIENT CORRECTION
save ; Since this correction takes time!

tmpcorr = fltarr(32,32,tmp.nbr_frame) ; Create matrix for corrected cube
tmpcorr(*,*,0:tmp.nbr_frame-1) = trans_cube(*,*,200:tmp.nbr_frame+200-1) / tmp.tint ; Insert values
tmp.cube = tmpcorr ; Replace the temporary cube
```

```

calib_raster, tmp, /reduce, /raster ; Calculate the corrected raster
tviso, tmp.raster <50 ; Display raster

data_dgst = tmp ; The transient corrected data
save, filename = 'data_dgst.xdr', data_dgst ; Store this data

; ***** Masking of unwanted pixels *****
index = where (tmp.otf eq 0) ; Find out which frames are not on target
tmp.mask (*,*,index) = tmp.mask (*,*,index) + 1 ; Mask all pixels that belong to these frames

test = fltarr (32,32) ; The variable "test" is used to search for...
for i=0,31 do for j=0,31 do test(i,j) = median(tmp.cube(i,j,*)) ; ...lines/columns which contains negative values.
tvsc1, congrid(test, 256, 256) < 50 ; View the "test" (median cube) image

tmp.mask (column,*,*) = tmp.mask (column,*,*) + 1 ; Repeat for all bad columns (with negative pixels)
tmp.mask (*,line,*) = tmp.mask (*,line,*) + 1 ; Repeat for all bad lines (with negative pixels)

calib_raster, tmp, /reduce, /raster ; MASKING (Calculate a new raster)
tviso, tmp.raster < 50 ; View this new raster
save ; Better safe than sorry

; ***** Flatfielding *****
data_flat = flat_builder (tmp.image) ; Start the subprogram "flat_builder"
print, where (data_flat eq 0) ; Check for zeros in the calculated flatfield
save, filename = 'data_flat.xdr', data_flat ; Save the flatfield

calib_raster, tmp, inflat = data_flat, /raster ; FLATFIELDING (Calculate a new raster)
tviso, tmp.raster < 50 ; View this new raster

data_dgstmf = tmp ; This is the final, processed data...
save, filename = 'data_dgstmf.xdr', data_dgstmf ; Save it!

; ***** Point source detection and photometry8 *****
det_raster_bus, data_dgstmf, data_det, raster = "Proj_st" ; Start the subprogram "det_raster_bus"
; (raster = "Proj_st" is only used the first time !!)
hs, data_det ; Examine the new structure "data_det"
save, filename = 'data_det.xdr', data_det ; Save the source-detection structure

phot_raster_ter, data_dgstmf, data_det, data_phot ; Start the subprogram "phot_raster_ter"
save, filename = 'data_phot.xdr', data_phot ; Save the photometry structure

; ***** Cross-correlation between LW2 & LW3 sources *****
crosscorrnew, data(LW2)_phot, data(LW3)_phot, 15, out ; 10" was used instead of 15" for CC_LW2 / LW3
area_cross = out ; area is W, E, CN, CS or CC for Cepheus A
save, filename = 'area_cross.xdr', area_cross ; Save the cross-correlation for the current region

```

⁸ Even though the point source detection (and photometry) section in this 'program' may seem short, and easy to do, the truth is quite the opposite. It often takes several hours to properly detect and measure (photometry) enough point sources for one raster, using the two sub-programs 'det_raster_bus' and 'phot_raster_ter'.

Appendix B – Aperature photometry program

```

;
;                               Photometry program by Magnus Gålfalk
;                               Written in the IDL language (Research Systems, Inc.)
;
;
; This version was finished 1999-06-24 and is used for photometry in the V passband observations.
; It can easily be used for any observations, just by changing some input-variables as indicated in the remarks.

; ***** Source-specific parameters, set for each source *****
Sourcepos = [800,800]           ; Position of source      [pixels]
Aprad =     15.0                ; Aperature radius     [pixels]
Skyrad =    100.0              ; Sky radius           [pixels]

; ***** User-specific parameters, set for each project *****
mosaic =    vmosaic             ; Name of mosaic to use for photometry
PSF =       PSFALL              ; Name of precalculated integrated PSF
sigma =     sigmav              ; Name of precalculated uncertainty table
cuts =      [0,300]             ; Min and Max-cuts for display [ADUs]
wsize =     [1000,750]          ; Window size
Apsize =    2                   ; Aperature rebin size

; ***** Automatic parameters, calculated by the program *****
msize =     (size(mosaic))([1,2]) ; Mosaic size
starx =     Sourcepos(0)>(Aprad+1)<(msize(0)-Aprad-2) ; Limited x-pos of source
stary =     Sourcepos(1)>(Aprad+1)<(msize(1)-Aprad-2) ; Limited y-pos of source
Skyrad =    Skyrad>(Aprad+1)<min([starx,msize(0)-1-starx,stary,msize(1)-1-stary]) ; Justified sky size

; ----- Show mosaic with the source preferably at the window's centre -----
wdelete, 0,1,2,3,4                ; Remove old windows
window, 0, xs=wsize(0), ys=wsize(1) ; Create mosaic window
xmin =    starx-wsize(0)/2.0 & xmax = starx+wsize(0)/2.0 ; x limits, Display
ymin =    stary-wsize(1)/2.0 & ymax = stary+wsize(1)/2.0 ; y limits, Display
dx =     ((0-xmin)>0)+((msize(0)-1-xmax)<0) & xmin=xmin+dx & xmax=xmax+dx ; x center offset, source
dy =     ((0-ymin)>0)+((msize(1)-1-ymax)<0) & ymin=ymin+dy & ymax=ymax+dy ; y center offset, source

tvsc1, mosaic(xmin:xmax,ymin:ymax)>cuts(0)<cuts(1) ; Plot mosaic

centx = wsize(0)/2.0-dx            ; Source x pos in window
centy = wsize(1)/2.0-dy            ; Source y pos in window

v = 2*pi/48.0                      ; Constant angle
for i = 0,47 do begin                ; Draw Aperature and Sky
    plots, centx+Aprad*cos(i*v), centy+Aprad*sin(i*v), /DEVICE
    plots, centx+Aprad*cos((i+1)*v), centy+Aprad*sin((i+1)*v), /DEVICE, /CONT, COL=-1
    plots, centx+Skyrad*cos(i*v), centy+Skyrad*sin(i*v), /DEVICE
    plots, centx+Skyrad*cos((i+1)*v), centy+Skyrad*sin((i+1)*v), /DEVICE, /CONT, COL=50000
endfor

; ----- Calculate equatorial coordinates of the source -----
Rasec =    A + B*starx + C*stary    ; RA (Epoch 1950) [seconds]
Decarcsec = D + E*starx + F*stary   ; DEC (Epoch 1950) [arc-seconds]

```

```

; ***** PHOTOMETRY CALCULATIONS *****
; ----- First, setup some Sky and Aperature variables -----
Skysize = 0 & Skypix = fltarr((2*Skyrad+1)^2) & Skyinfo = 0 & Skysigma = 0 & Sky = 0
Apsize = 0 & Appix = fltarr(Aprad*Apbin+1,4) & ApFlux = 0
for i = 0, Aprad*Apbin do begin
    Appix(i,0) = float(i)/Apbin ; Binned radii
    Appix(i,1) = 0 & Appix(i,2) = 0 & Appix(i,3) = 0 ; Initialize 'Appix' values
endfor

; ----- Then, all Sky and Aperature data is read -----
for sy = stary-Skyrad, stary+Skyrad do begin ; LOOP over y-values...
    for sx = starx-Skyrad, starx+Skyrad do begin ; LOOP over x-values...
        dist = sqrt((sx-starx)^2+(sy-stary)^2) ; Distance from centre of source
        bin = round(dist*Apbin) ; Radius-bin to use for this pixel
        if dist gt Skyrad then goto, outside ; Outside Sky circle ?
        if dist lt (Aprad+0.5/Apbin) then begin ; Inside Aperature ?
            Apsize = Apsize + 1 ; Number of Aperature pixels read
            Appix(bin,1) = Appix(bin,1) + 1 ; Add a pixel to radius bin
            Appix(bin,2) = Appix(bin,2) + mosaic(sx,sy) ; Read Aperature pixel to radius bin
            ApFlux = ApFlux + mosaic(sx,sy) ; Total Aperature flux (Not Sky corr.)
        endif else begin
            Skypix(Skysize) = mosaic(sx,sy) ; Read Sky pixel
            Skysize = Skysize + 1 ; Number of sky pixels read
        endelse
    outside:
    endfor
endfor

; ----- SKY Calculations -----
Skypix = Skypix(0:Skysize-1) ; Collect all read Sky pixels
Skyinfo = moment(Skypix) ; Statistical Sky analysis
Skysigma = sqrt(Skyinfo(1)) ; Sky Sigma
Sky = Skyinfo(0) ; Sky Mean
Skymedian = median(Skypix) ; Sky Median
Skycopy = fltarr(Skysize) & clipped = 0 ; Setup variables to be used below
for i = 0, Skysize-1 do begin ; 3-SIGMA CLIPPING of Sky pixels...
    if abs(Skypix(i)-Skymedian) lt (3*Skysigma) then begin
        Skycopy(i-clipped) = Skypix(i) ; Store good Sky pixels in Skycopy
    endif else begin
        clipped = clipped + 1 ; Number of clipped pixels
    endelse
endfor

; ----- Update Sky variables after 3-sigma clipping -----
Skysize = Skysize - clipped ; Number of sky pixels to be used
Skypix = Skycopy(0:Skysize-1) ; Copy these back to 'Skypix'
Skyinfo = moment(Skypix) ; New statistical Sky analysis
Skysigma = sqrt(Skyinfo(1)) ; Sky Sigma
Sky = Skyinfo(0) ; Sky Mean
Skymedian = median(Skypix) ; Sky Median
Skyclipped = clipped ; Nr. of 3-Sigma clipped pixels

; ----- APERATURE Calculations -----
ApFlux = ApFlux - Sky*Apsize ; Correct Aperature flux for Sky

```



```

IntegratedF = 0 ; Integrated flux (dummy variable)
for i = 0, Aprad*Apbin do begin
  Appix(i,2) = Appix(i,2)-Sky*Appix(i,1) ; Correct Aperature bin for Sky
  IntegratedF = IntegratedF + Appix(i,2) ; Integ. flux (sky corrected) out to this bin
  Appix(i,3) = IntegratedF/ApFlux ; Integ. flux expressed as a factor
endfor

integ = PSF(Aprad*Apbin) ; Integrated part of source (from PSF)
ADU = ApFlux/integ ; Total flux of point source [ADU]

; -----One dimensional PSFs for this source (through the centre) -----
PSFx = filtarr(2*Aprad+1) ; PSF along the x-axis (horizontally)
PSFy = filtarr(2*Aprad+1) ; PSF along the y-axis (vertically)
PSFpos = intarr(2*Aprad+1) ; Pixel deviations from centre
PSFpeek = 0 ; Dummy variable

for sx = -Aprad, +Aprad do begin ; Read PSFs along the x & y axis...
  PSFx(PSFpeek) = mosaic(starx+sx, stary)
  PSFy(PSFpeek) = mosaic(starx, stary+sx)
  PSFpos(PSFpeek) = sx
  PSFpeek = PSFpeek + 1
endfor

window, 1, xs=300, ys=200, title='PSF(x) for this source' ; Plot the x-axis PSF...
plot, PSFpos, PSFx, xtitle='Pixel', ytitle='Flux'
plots, 0, min(PSFx), /DATA
plots, 0, max(PSFx), /CONTINUE, /DATA, COLOR = 61000
plots, -Aprad, SKY, /DATA
plots, +Aprad, SKY, /CONTINUE, /DATA, COLOR = 65000

window, 2, xs=300, ys=200, title='PSF(y) for this source' ; Plot the y-axis PSF...
plot, PSFpos, PSFy, xtitle='Pixel', ytitle='Flux'
plots, 0, min(PSFy), /DATA
plots, 0, max(PSFy), /CONTINUE, /DATA, COLOR = 61000
plots, -Aprad, SKY, /DATA
plots, +Aprad, SKY, /CONTINUE, /DATA, COLOR = 65000

; ----- Integrated radii-PSF for this source -----
Iindex = where(appix(*,1) gt 0) ; Exclude radii with 'no pixels'
window, 3, xs=300, ys=200, title='Integrated PSF for this source'
plot, Appix(Iindex,0), Appix(Iindex,3)

; ----- Signal Strength PLOT -----
window, 4, xs=300, ys=200, title='Signal strength (Compared to Sky)'
plot, Appix(Iindex,0), Appix(Iindex,2)/(Appix(Iindex,1)*Skysigma), yrange = [-0.5,+15], ystyle = 1, $
  xtitle='Radii [pixels]',ytitle='Signal [Sky Sigma]'
plots, 0, 0, /DATA & plots, Aprad, 0, /CONT, /DATA, COL = 60000 ; zero line (median sky)
plots, 0, 1, /DATA & plots, Aprad, 1, /CONT, /DATA, COL = 50000 ; 1-Sigma line (68.27 %)
plots, 0, 2, /DATA & plots, Aprad, 2, /CONT, /DATA, COL = 40000 ; 2-Sigma line (95.45 %)
plots, 0, 3, /DATA & plots, Aprad, 3, /CONT, /DATA, COL = 30000 ; 3-Sigma line (99.73 %)
plots, 0, 4, /DATA & plots, Aprad, 4, /CONT, /DATA, COL = 20000 ; 4-Sigma line (99.994 %)
plots, 0, 5, /DATA & plots, Aprad, 5, /CONT, /DATA, COL = 76000 ; 5-Sigma line (99.99994 %)

if skyrad eq 25.0 then skyid = 0 ; Check if: Sky-type 1
if skyrad eq 50.0 then skyid = 1 ; Check if: Sky-type 2
if skyrad eq 100.0 then skyid = 2 ; Check if: Sky-type 3
sigmaflux = sigma(skyid, aprad-1) ; Obtain flux uncertainty
print, "Total source flux:", adu, "+-", sigmaflux, " ADU" ; Total flux with uncertainty
print, "V-mag: ", (2.5*log10(adu)-c1)/c2 ; V-magnitude (Only in the V-mosaic case)

END ; END OF PROGRAM

```

Appendix C – Vocabulary

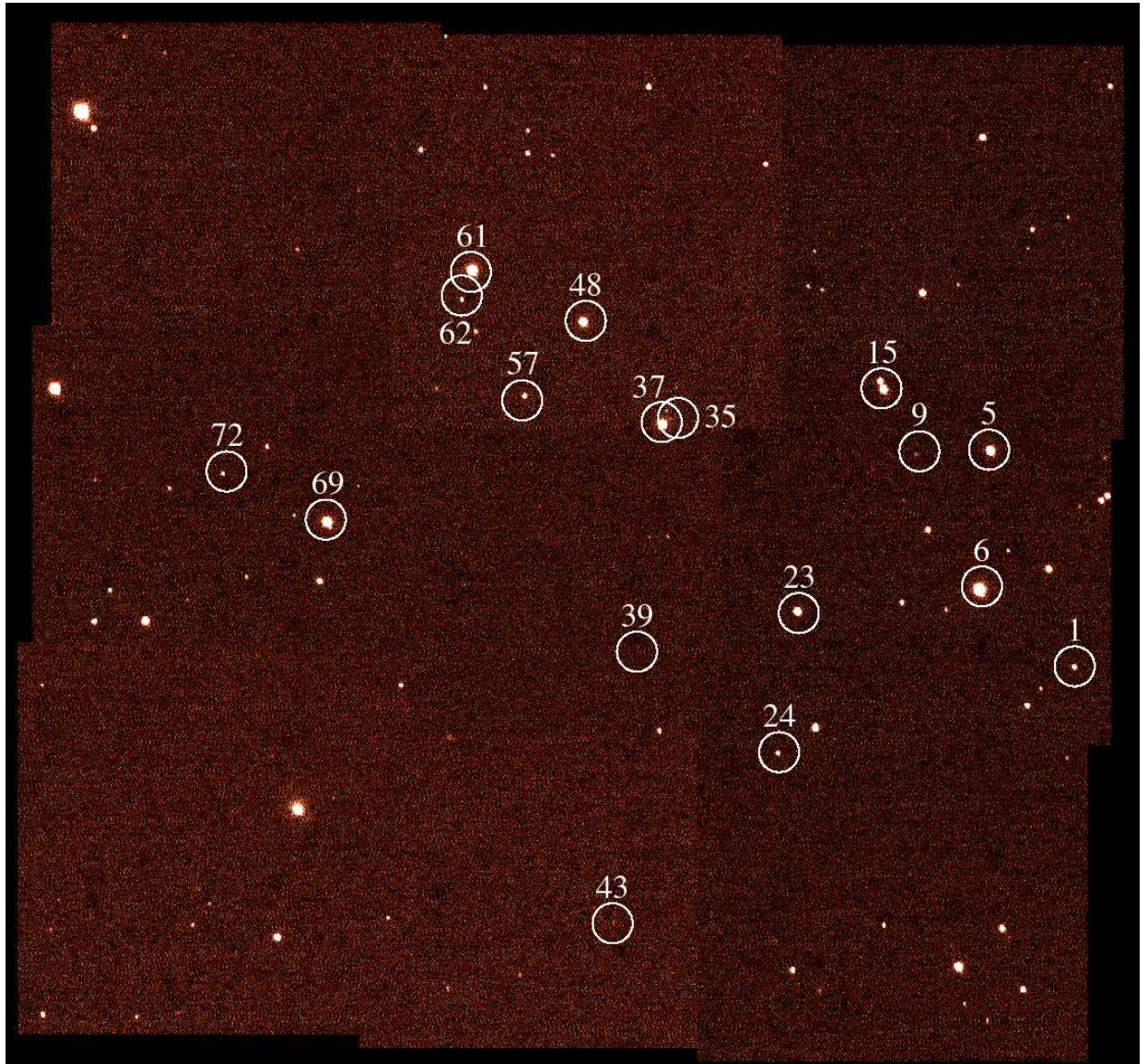
2MASS	Two Micron All Sky Survey (In the J, H and Ks passbands).
A0 Star	Spectral type of a star with a 'very flat' spectrum.
AD-converter	Analog to Digital converter.
ADU	Analog to Digital Unit.
Bias	Constant offsets added to each pixel of a CCD-camera.
Brown Dwarf	A Star with too small mass to start nuclear burning.
CCD	Charge Coupled Devices (Digital camera type).
Cep A	Short for the molecular cloud Cepheus A.
CIA	A high level computer language: ISOCAM's Interactive Analysis system.
CTTS	Classical T-Tauri Star (Often having a disk of gas and dust).
Colour diagram	A diagram with spectral brightness comparison on one axis.
Colour/Colour diagram	A Colour diagram with brightness comparisons on both axes.
Cut-off filter	A filter that blocks all light above a certain wavelength.
Cut-on filter	A filter that blocks all light below a certain wavelength.
Dark pattern	The striped even-odd 'readout' pattern in raw ISOCAM images.
Dead Column	A not working column (24) of the LW array.
Dec	Declination, a coordinate in the equatorial coordinate system.
Epoch	A standard reference in time for equatorial coordinates.
Equatorial coordinates	A coordinate system (Ra, Dec) of the sky that is aligned with the Earth's axis.
ESA	European Space Agency.
Far-IR	Far InfraRed spectral region (30-300 microns).
FFT	Fast Fourier Transform. Matematical algorithm (See Gonzales, 1987.)
Filter wheel	A rotational wheel with filters that makes filter changing easy.
Flatfielding	A method of making all image elements equally sensitive.
FOV	Field Of View.
Ghost source	A false source due a previously observed bright source.
Glitch	Streaks across images due to impacts with particles.
GMC	Giant Molecular Cloud.
GSC	Hubble Guide Star Catalogue.
H-filter	Near-IR passband filter (1.65 microns).
Herbig Haro object	Collisionally excited regions arising from the interaction of gas jets and the ISM.
HII region	Regions of ionized hydrogen gas surrounding newborn massive stars.
IAS	A transient correction method (See Starck et al. 1999).
IDL	A high level computer language developed by Research systems, Inc.
IMF	Initial Mass Function.
Interstellar reddening	The reddening of starlight due to its passage through intervening dust clouds.
IR-Excess	Stars that are 'redder' than expected from normal photospheres.
IRAS	InfraRed Astronomical Satellite.
ISM	InterStellar Medium, Gas and dust that exists between stars.
ISO	Infrared Space Observatory.
ISOCAM	ISO instrument: Infrared Camera.
ISOCAM-Cube	Three dim. array of readouts (32 x 32 x nr. of frames).
ISOCAM-Frame	A 32 x 32 pixel exposure.
ISOCAM-Image	The mean of all frames for a specific sky position.
ISOCAM-Mosaic	A mosaic of all rasters.
ISOCAM-Raster	All images put together into one image of a whole region.
J-filter	Near-IR passband filter (1.25 microns).
Jy	Jansky, unit for flux measurement.
Ks-filter	Near-IR passband filter (2.17 microns).
Light pollution	Brightening of the sky due to man-made sources (street lights etc.).
LW	Long Wavelength channel of ISOCAM.
LW2	Long Wavelength filter 2 (6.7 microns).
LW3	Long Wavelength filter 3 (14.3 microns).
Maser	Microwave Amplification by Stimulated Emission of Radiation.
Masked pixel	A bad pixel, not included in following calculations.

MF	Mass Function.
Micron	Wavelength unit (equal to 1 micrometer).
Mid-IR	Mid InfraRed spectral region (5-20 microns).
MMT	Multiresolution Median Transform, a deglitch method (See Starck et al.1996).
Near-IR	Near Infrared spectral region (0.7-5 microns).
Optical depth	A measure of observational depth into an object.
Optical double star	A not physically connected double star (line of sight effect).
Overhead	Time to prepare ISOCAM for an observation.
PAHs	Polycyclic Aromatic Hydrocarbons.
PFOV	Pixel Field Of View.
PSC	Point Source Catalogue of 2MASS sources.
PSF	Point Spread Function, the diffracted image of a point source as seen by a telescope.
PSS	Palomar Sky Survey (optical).
RA	Right Ascension, a coordinate in the equatorial system.
RA Drift	The lagging of a telescope's pointing position in RA during an exposure.
Readout	One 32 x 32 pixel frame read from ISOCAM.
SED	Spectral Energy Distribution.
Sidereal time	Time based on consecutive meridian crossings of a star.
SSCD	A raw-data format of ISOCAM.
SW	Short Wavelength channel of ISOCAM.
SWS	ISO instrument: Short Wavelength Spectrometer.
Transient	Biased flux measurements due to a large flux step before the observation.
V filter	Optical passband filter (0.55 microns).
Van Allen belts	Ions from the Sun, bouncing back and forth between Earths magnetic poles.
Vignetting	A circular degradation of sensitivity towards the edges of an image.
YSO	Young Stellar Object.

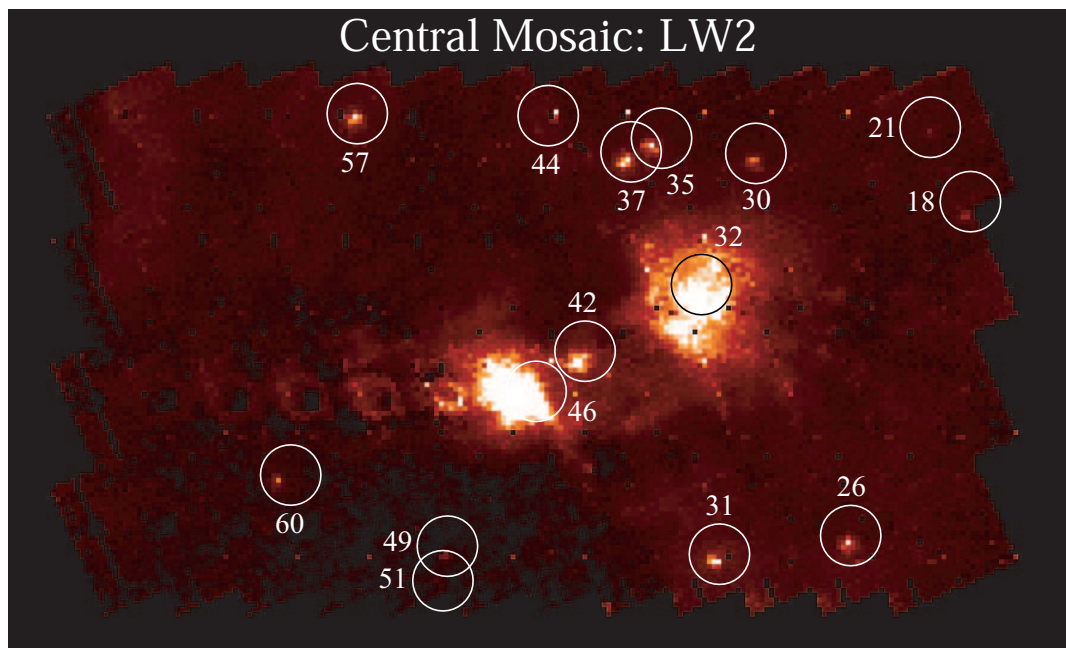
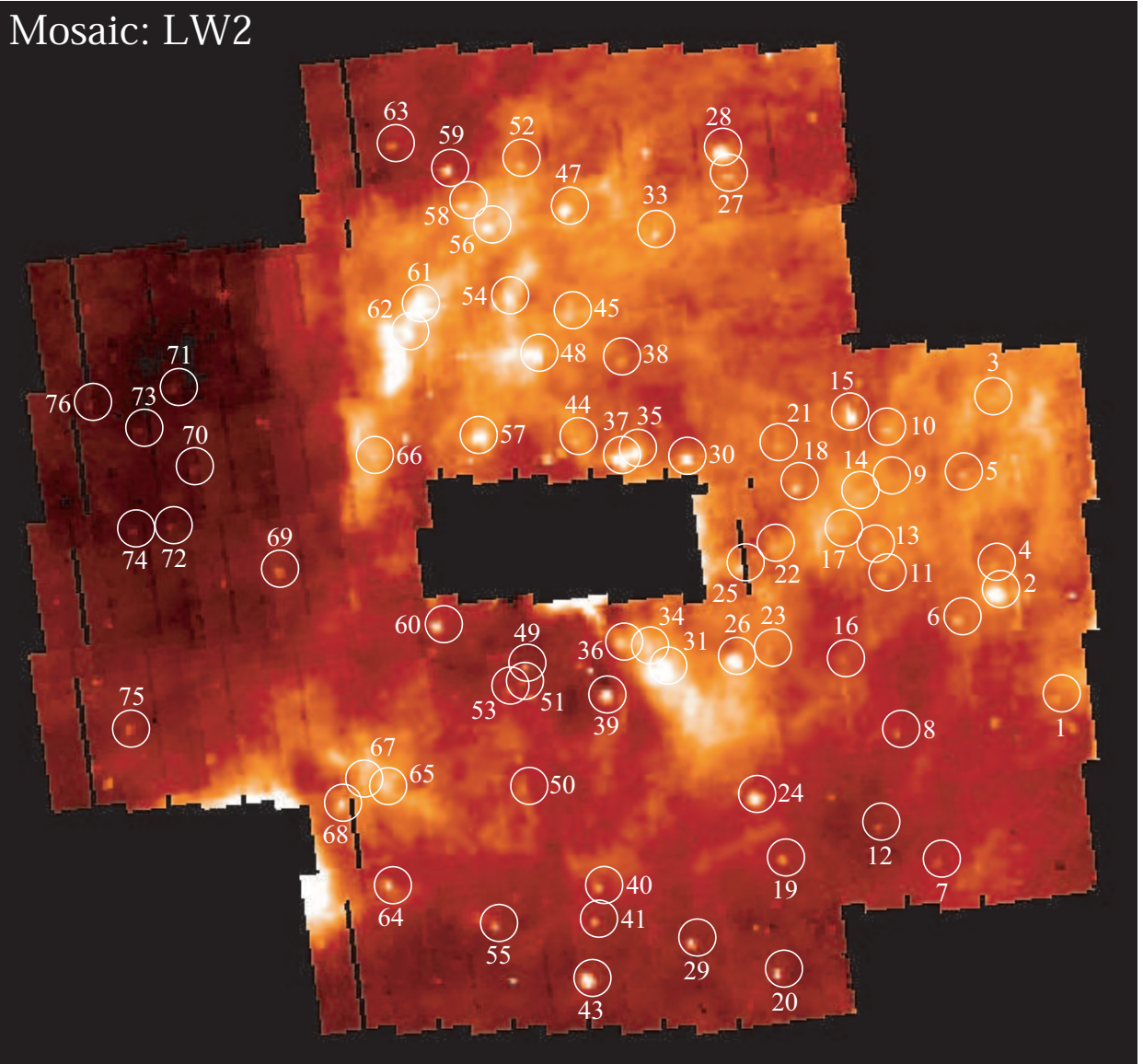
Appendix D – The optical mosaic (V filter)

In this appendix, the V-filter mosaic is presented with detected ISOCAM sources circled (except for the weakest detections, which would be impossible to see with these ADU cuts).

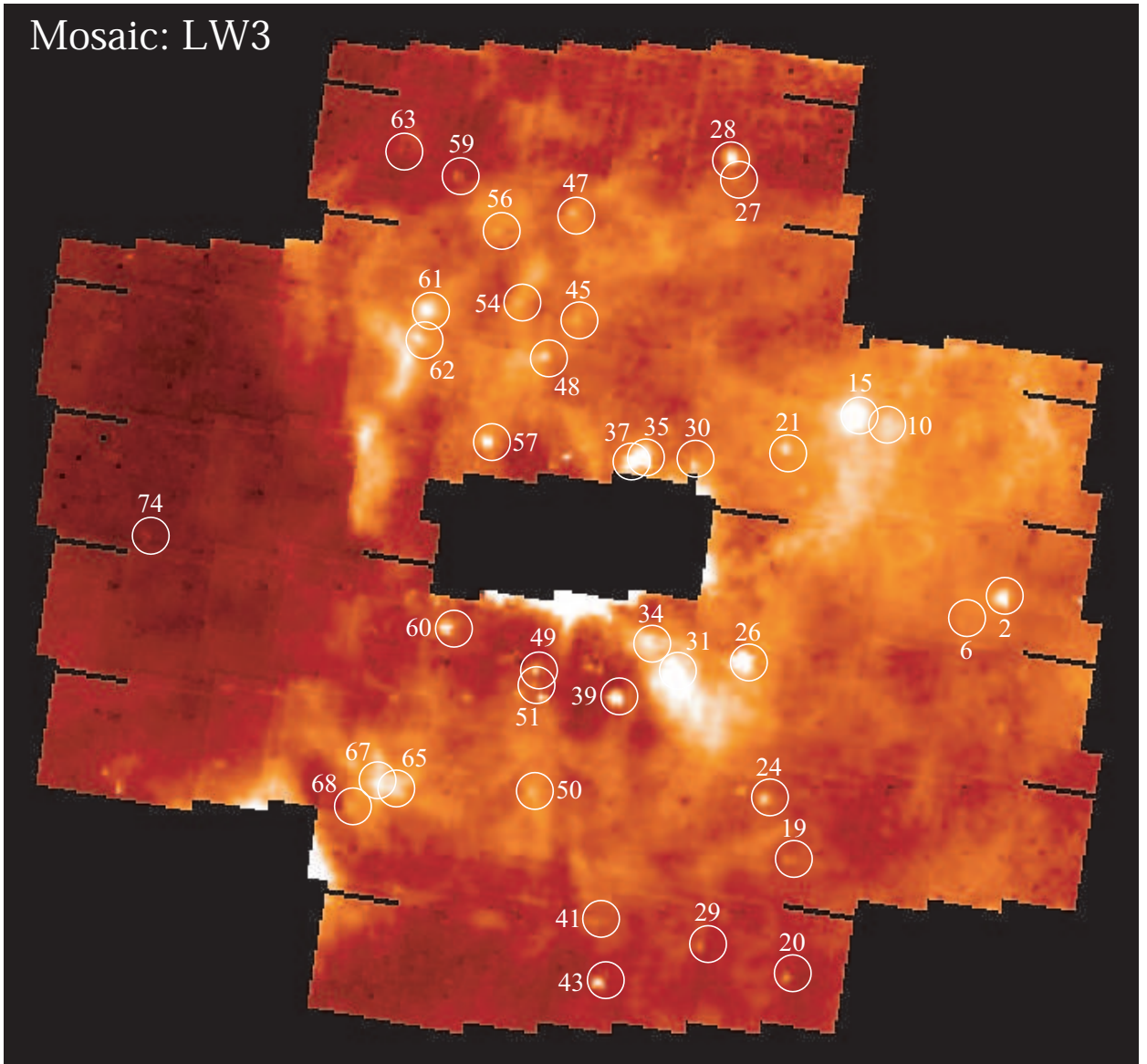
The 1.05 μm mosaic has a similar appearance as the V mosaic. Therefore, only the V-mosaic is shown in this appendix.



Appendix E - ISOCAM mid-IR mosaics



Mosaic: LW3



Central Mosaic: LW3

